Exploring the Solar Middle Corona through Low Frequency Radio Bursts

Jinge Zhang

Doctor of Philosophy

of

University College London

Department of Space and Climate Physics

Mullard Space Science Laboratory

University College London

May 23, 2024

I, Jinge Zhang, confirm that the work presented in this thesis is my own. Where information has been derived from other sources, I confirm that this has been indicated in the work.

致虚极，守静笃，
万物并作，吾以观其复

Abstract

Solar radio bursts are signatures of electron beams traveling through various magnetic flux tube structures in the solar corona. Type III bursts move along 'open' magnetic fields into interplanetary space, while J and U bursts travel along closed loops. This thesis delves into these bursts to dissect the kinetic properties of accelerated electron beams and the physical attributes of the middle coronal plasma and magnetic field. Three distinct research projects are introduced in this thesis.

Firstly, using the LOw-Frequency-ARray (LOFAR) and the Parker Solar Probe (PSP), 54 type III and J-bursts were identified during a significant solar radio noise storm on 10 April 2019. These observations revealed a critical similarity in exciter velocities between the burst types, suggesting a shared electron injection acceleration region across both open and closed magnetic structures during the event. Furthermore, a new method was introduced for inferring the plasma density model and physical parameters of large coronal loops using J burst spectra.

Secondly, with the LOFAR interferometric solar imaging data from 5 June 2020, a large coronal loop extending to 2.3 solar radii was captured as a bright U-burst was observed. This marked the first simultaneous imaging of both the upward and downward legs of a large loop extending into the middle corona. The analysis allowed for unprecedented comparisons of beam velocities and loop physical parameters between the two legs of this expansive loop, revealing electron beam deceleration and shedding light on the historically ill-defined large loops.

Lastly, by utilizing microwave and radio measurements during a solar burst on 3 June 2021, the travel time of the electron beam from the microwave emission to the radio emission region was estimated. By testing various numerical coronal density models and comparing them with the time gap between peak fluxes at two different wavelengths, a coronal plasma density model for the event was extrapo-

lated. This offers a novel multi-wavelength approach for diagnosing corona plasma conditions.

Impact Statement

The Sun releases massive amounts of energy through 'explosions', engendering events known as jets, flares, and coronal mass ejections. These events release stored magnetic energy by accelerating particles and ejecting them from the Sun's atmosphere, the corona, into the solar system in the form of solar winds. Solar winds shape space weather around our planet and influence technologies we rely on daily, such as communication satellites in orbit. Understanding the formation of solar wind and its origin, the corona, is crucial.

Recently, solar physicists have ascertained that the middle corona, from 0.5 to 5 solar radii above the Sun's surface, serves as the "kindergarten" for 'young' solar wind. However, this region remains poorly understood due to its low plasma density and the faint X-ray and Extreme Ultra-Violet (EUV) emissions, which pose more challenges for detection compared to the intensely studied lower corona. Nonetheless, solar explosive events that drive accelerated electron beams, pivotal to solar wind generation, navigate this region, generating low-frequency radio emissions. These emissions, observed and identified as solar radio bursts, serve as excellent diagnostics of the local plasma and magnetic field environment along the beams' trajectories.

The research presented in this thesis utilised the most advanced ground-based radio telescopes, the Low-Frequency Array (LOFAR), combined with multiple instruments, to observe these solar radio bursts. My work investigates the kinetic properties of these accelerated electron beams travelling through the middle corona along 'open' and closed coronal magnetic flux tubes. My key findings include the similarities of beam speed travelling along both magnetic structures during the same solar noise storm, and I also discovered the apparent decelerations of the beam travelling from large coronal loop's upward to downward leg. I provide new insights

on diagnosing electron beam dynamics by using radio bursts on both spectroscopy and interferometric imaging analysis. Furthermore, I have developed a new strategy for deriving large coronal loops by using solar radio data. I have imaged a loop that reached 1.3 solar radii, a size for such magnetic structures that has never been imaged before. I discovered the loop's symmetry in physical parameters (plasma temperature, pressure, and magnetic field). These findings are crucial for understanding the scientific nuances of the solar middle corona's functioning and for comprehending the formation of the solar wind. Such knowledge has significant practical applications, including the enhancement of advanced space weather forecasting models.

The outcomes of this thesis have significant implications for further studies using low-frequency solar radio data from both ground- and space-based instruments. This thesis provide a new strategy for combining multiple instruments and multiple wavelengths studies, such as combining LOFAR and Parker Solar Probe data to investigate the classification of radio burst types; the combination of several ground-based radio telescopes to identify the whole structure of a burst and including polarisation measurements of a single event. Moreover, diagnostic coronal plasma distribution models study the temporal relation between multi-wavelength data. This thesis can benefit future joint multi-wavelength and multi-instrument observational campaigns and act as an important example study and analysing solar radio bursts.

Acknowledgements

Firstly, I cannot express enough thanks to my parents, Zhang Jiaying and Hou Hongling. Without your endless support throughout not just my PhD but my past ten years of educational life, from my undergraduate and master's degrees, I would not have been able to deliver this work. Your love, understanding, and belief in me have been a constant source of strength.

Mingxing, my wife, words cannot fully express my gratitude for your unwavering support. Always by my side, you provided me with the warmth of your mental and physical hugs whenever I needed it most. Despite being separated for two years and enduring the hardest and longest distance in our relationship due to the pandemic, we chose to get married. This decision taught us that spatial and temporal difficulties are never insurmountable obstacles, and that love is always the solution. You truly own half of this thesis. I cannot imagine how much harder this journey would have been without you.

Heartfelt thanks to my supervisor, Dr Hamish Reid. I always like to regard you as my academic father for introducing me to the captivating world of solar radio physics. Our countless meetings and conversations, whether in your office, at coffee shops, on the streets, in pubs and parks, or online, have been incredibly enriching and fun. Moreover, you have been a wonderful friend and collaborator, always mindful of my feelings, continuously encouraging me, and consistently offering the best advice. Special thanks also to my secondary supervisor, Prof Sarah Matthews, for your unwavering support since my time as a master's student at UCL. Immense gratitude to my supervisory team for your contributions to this thesis, as you have proofread many versions of the draft, until the final minutes.

Deep thanks to all my collaborators outside MSSL. Dr. Eoin Carley and Prof. Peter T. Gallagher, thank you so much for your support and for hosting me to learn

interferometric imaging at DIAS. Thanks to Dr. Pietro Zucca for hosting me for a week at ASTRON and teaching me LOFAR skills. Thanks to the Royal Astronomical Society for providing me with travel grants when I needed them. And also, a big thanks to my home institution, University College London - Mullard Space Science Laboratory, for providing me with the best environment possible and support when I needed it the most.

To my dear G01 office crew, thank you to each and every one of you for making our space in MSSL the most beautiful and friendly office. As Solar Group PhD students, your support has been invaluable, in too many ways to fully articulate here. Andy, what a man, thank you for your friendship. Your unique ability to make everyone around you feel comfortable is truly magical. Hannah, my lovely flatmate, our time spent in Woking has undoubtedly become a shining diamond in my PhD journey. Together, we overcame the most challenging pandemic years, and I'm deeply grateful for your gracious support when I needed it most. Ryan, Jenny, and Diego, I am profoundly thankful for your guidance and friendship as the wonderful senior PhDs in our group when I joined. Teia, your organisation of so many amazing Solar Group activities has created countless beautiful memories throughout my PhD life. Camille, my academic sister, your proficiency in Chinese amazes me, and your company in the solar radio gang is always delightful. You are definitely the sunflower of G01, if we were a garden! Nawin, living together in Guildford has been a joy, and I'm often moved by your considerable kindness towards me. Julio and James, as the two new bright stars of G01, I'm grateful for your patience with my endless random conversations. Talking with both of you is always a pleasure, as you inspire me in numerous ways.

To Lidia, Lucie, Deb, Alex, David Long, and David Stansby, our esteemed teaching and senior researchers team, I extend my profound gratitude to all of you. From the very beginning, you opened your arms and provided me with the warmest welcome to the group. Since then, every conversation with each one of you has been a learning opportunity, and these kindness interactions have significantly shaped me into the young researcher I am today. I have witnessed your passion and patience, qualities I believe embody the spirit of extraordinary lifetime researchers, regardless of where we go and where we live.

A huge 'thank you' to all MSSL staff, as your support has been incredibly important to me throughout my PhD! Many of you have assisted me in various dimensions. Particularly, to Philippa and Rosemary, who provided me with accommodation in the UK during the MSSL closure due to the pandemic in 2020, and my writing-up period when my original accommodation contract ended earlier. Rosemary and Philippa's family offered me the warmth of family that I was so fortunate to have in the UK as a foreign student. Living on the farm has been a fantastic experience, and I am absolutely sure that it will become a lifelong cherished memory for both me and my wife. Thank you for taking care of us; we will maintain this friendship (or, familyship) for the rest of our lives.

To my grandparents, 姥姥, 姥爷, 爷爷, 奶奶, I miss you all dearly. It wasn't long ago that I had you all, but now you are gone. Words cannot fully capture my feelings now, as they are too complex, especially as I write in English, a language you might not understand. I cannot simply described my feeling as 'thanks' to you, because 'thanks' is infinitely too small a word. This mix of emotions—'sadness' for you are not here by my side, 'happiness' for achieving something you would have loved to see, 'regret' for not being by your side as I spent most of my time in the UK, and 'hope' for the future that to become a great scientist we all dreamed I would be. Since I was a baby, your endless belief in me that I am the best, teaching me honesty, selflessness, kindness, and bravery, has sown the seeds of who I am today. I have aspired to be a scientist from a very young age, and you were proud and supportive of me in achieving this goal. I have finally reached this milestone, and I wish you all happiness wherever you may be. Completing my PhD is a chapter I can now share with you, and it's a good one. I promise to deliver good upcoming chapters in the future and will keep you updated.

I would like to express my great thanks to all of my friends back in China, especially Jiangling, Yubin, Yuyue, and Minyi. Although it has been very long since we separated after university, our WeChat group remains one of the most active one until today. My thanks also extend to my brotherly friends Xueqian and Luning, who have provided unwavering support and shared unforgettable memories with me throughout our time at UCL and our adventures in London. Caode, my best friend of 16 years, I know this friendship will last a lifetime. You are like a star in

my life, always there for me. To all of you, your mental support has been invaluable to me, and I am confident that our friendship will age like the finest wine in the world. Our bond has been strengthened through mutual support during challenging times and celebrations during the joyful moments, always.

At the end, I would like to extend my gratitude to myself. Well done, Jinge, it has indeed been a marathon, and no one else truly understands the full meaning of this period in your life, the extent of its wonder and its challenges. Overall, you are doing well. Have confidence in the quality of the research you have accomplished, and strive to enhance this quality further in the future. Be proud of the skills and knowledge you have acquired during this PhD, and aim to expand upon them. Being a researcher is a lifelong journey. Please, never let the flame of curiosity in your mind gone. Maintain a strong heart, be gentle, and stay cool.

List of Publications

1. Imaging a large coronal loop using type U solar radio burst interferometry
   Jinge Zhang, *Hamish A.S. Reid, Eoin Carley, Pietro Zucca, Peijin Zhang*
   The Astrophysical Journal (2024), ; DOI: 10.3847/1538-4357/ad26fd

2. *Deriving Large Coronal Magnetic Loop Parameters Using LOFAR J Burst Observations*
   Jinge Zhang, *Hamish A.S. Reid, Vratislav Krupar, Pietro Zucca, Bartosz Dabrowski, Andrzej Krankowski*
   Solar Physics (2023); DOI: 10.1007/s11207-022-02096-0

3. *A study of the Relationship Between the Microwave and Meter-Wavelength Emissions from the Solar Flare on June 3, 2021*
   Julia Nasimovna Shamsutdinova, ***Jinge Zhang****, Dmitriy A. Zhdanov, Larisa Kamaletdinova Kashapova, H. A. S. Reid*
   Proceeding of Science Volume 425: PoS-MUTO (2022); DOI: 10.22323/1.425.0065

4. *Relationship between microwaves and meter range during the Solar flare on June 3, 2021*
   Julia Nasimovna Shamsutdinova, Larisa Kamaletdinova Kashapova, ***Jinge Zhang****, H. A. S. Reid, Dmitriy A. Zhdanov*
   Monthly Notices of the Royal Astronomical Society, (In review)

5. *Interpretation of Radio Wave Scintillation Observed through LOFAR Radio Telescopes*
   Biagio Forte, Richard A. Fallows, Mario M. Bisi, ***Jinge Zhang****, Andrzej Krankowski, Bartosz Dabrowski, Hanna Rothkaehl, Christian Vocks*

The Astrophysical Journal Supplement Series (2022); DOI: 10.1007/s11207-022-02096-0

6. *Geosynchronous Magnetopause Crossings and Their Relationships With Magnetic Storms and Substorms*
   A. A. Samsonov, Y. V. Bogdanova, G. Branduardi-Raymont, L. Xu, ***J. Zhang****, D. Sormakov, O. A. Troshichev, C. Forsyth*
   Space Weather (2021), DOI: 10.1029/2020SW002704

Contents

Chapter 1

Preface

Throughout human history, the Sun has been a subject of profound fascination and reverence. It has played a significant role in the religions and cultural traditions of civilizations across the globe. As the source of light and warmth, the Sun often symbolized divinity, enlightenment, and cyclical renewal.

Many ancient civilizations explored the secrets of the Sun in various ways. The Babylonians, Greeks, and Egyptians made early discoveries and explanations of solar activities. As humanity's understanding of science and technology advanced, so did our ability to study the Sun. The 19th and 20th centuries marked a new era in solar exploration, heralding the birth of modern solar physics. We came to understand that the Sun is just one of hundreds of billions of stars in the Milky Way galaxy, and our galaxy is but one among the countless others in the known universe.

1.1 The Sun as a Star

The Sun, a massive ball of hot plasma, is positioned at the centre of our solar system, dominating this celestial stage as the primary force shaping our existence. Its colossal presence extends across a diameter of 1.4 million kilometres. With a mass of 1.9889×10^{30} kg, predominantly composed of hydrogen and helium, the Sun dwarfs every other object in the solar system with its gravitational pull. It is classified as a G-type main-sequence star (G2V), also known as a 'yellow dwarf'.

As the closest star to Earth, electromagnetic waves, including visible light, take approximately 8.3 minutes to travel from the Sun to Earth. This duration is significantly shorter compared to the light travel time from Rigil Kentaurus (V645 Centauri), which is 4.2 light-years away. Studying the Sun, serving as an ideal

sample star and a nearby space plasma laboratory, provides us with insights that might not be obtainable from other stars and solar systems in the distant universe. These distant celestial bodies are visible but currently unreachable.

The Sun radiates electromagnetic waves of almost all wavelengths into space, a result of various physical processes occurring within its interior and atmosphere. To unravel the secrets of the Sun's physical properties and phenomena, researchers employ sophisticated instruments, including spacecraft and ground-based telescopes. These instruments observe the Sun from different distances, angles, and across a spectrum of wavelengths. Theoretical models have been pivotal in using these observations to deepen our understanding of the Sun's behaviour and the mysteries of its behaviour. These models range from the solar dynamo theory, which elucidates the Sun's activity cycles, and the emergence of magnetic flux tubes (see Charbonneau, 2020), to the Parker spiral model that describes the transportation of solar wind and the extension of the solar magnetic fields in the interplanetary medium (see Parker, 1958).

A particular area of interest in this thesis is the solar atmosphere, which is the outer component of the Sun that begins at the Sun's visible surface, the photosphere, and extends into interplanetary space. The primary focus of the research is the solar corona, a high-temperature portion of the solar atmosphere characterised by complex plasma dynamics and intricate magnetic field structures. The solar corona is an extremely inhomogeneous medium. It comprises regions that are either quiet (the quiet Sun), characterised by relatively 'small' closed magnetic loops, or dominated by 'open' magnetic fields, as seen in areas with lower temperatures known as coronal holes. Additionally, there are dynamic regions that consist of magnetic loops. These loops store magnetic energy and trap hot plasma in what are known as active regions. Within these active regions, massive amounts of magnetic energy are released through explosions, driven by interactions between twisted, extremely strong magnetic structures. These events lead to significant solar activity, known as flares and coronal mass ejections, which accelerate energetic particles and eject hot plasma gas into the solar system in the form of solar winds.

Solar winds traverse through the upper layers of the solar atmosphere, encompassing the middle and upper corona. In these regions, accelerated energetic par-

ticles, such as electrons, interact with the local ambient plasma and are influenced by variously characterised magnetic fields before being propelled into interplanetary space, heading towards planets, including Earth. Humans on Earth are safeguarded by our planet's atmosphere and magnetosphere, which serve as a delicate and thin protective shield against the Sun's hazardous radiation and the high-energy particles carried by the solar wind. The interaction of solar winds' high-energy particles and magnetic fields with the Earth's magnetosphere shapes space weather, impacting essential technologies that we rely on daily, such as communication and navigation satellites in orbit and electric power grids on the ground. Therefore, understanding the solar accelerated particles, such as high-speed flare-accelerated electron beams, and their interactions with the solar upper atmosphere—particularly the middle corona, which is not well understood—is crucial. This understanding is crucial not only for grasping the scientific nuances of the solar corona's functioning but also for comprehending the formation of the solar wind. Such knowledge has significant practical applications, including the enhancement of advanced space weather forecasting models.

1.2 Objectives of the Thesis

Since the seminal work of Parker (1958), which identified solar winds as outflowing plasma gas emanating from the Sun into interplanetary space, the origin and formation of solar winds have remained unclear. Recent advancements in solar physics have established that the middle corona, extending heliocentric distances from 1.5 to 6 $R_\odot$ (solar radii), serves as the 'kindergarten' for the 'young solar wind' (the middle corona defined by West et al., 2023). However, our understanding of the middle corona is hampered by observational constraints (key questions about the middle corona summarised by Seaton et al., 2023). Its low electron plasma density results in minimal X-ray or Extreme Ultra-Violet (EUV) emissions, making detection challenging. This issue is exemplified by the large coronal magnetic loops that extend into this region, which have historically been poorly defined due to a lack of observational data. Nevertheless, electron beams, a key component of the solar wind, are accelerated by solar activities such as flares and Coronal Mass Ejections (CMEs). As they traverse the middle corona, these beams generate radio waves at the background plasma frequency or its harmonic. Serving as a probe of the mid-

dle corona's plasma conditions and magnetic field properties, these electron beams offer valuable insights into the local plasma environment and the magnetic field properties along their path.

This thesis delves into the study of accelerated electron beams travelling along both open and closed magnetic flux tubes in the solar middle corona. Within this region, these beams produce high-intensity radio waves through plasma emission mechanisms, as detailed in section 3.1.2. These electromagnetic waves, captured by ground-based radio interferometers above 10 MHz and observed by space-based instruments below 10 MHz, cannot pass through the Earth's atmospheric window, which only allows a limited range of electromagnetic waves to propagate through and reach ground-based instruments. These wide frequency range radio fluxes are identical and identified as solar radio bursts. Specifically, this study focuses on observations of type III, J, and U bursts in the 20-80 MHz range, observed by the Low-Frequency Array (LOFAR) telescope (see van Haarlem et al., 2013). These three types of solar radio bursts are part of the 'fast-drift bursts' family, as introduced in Chapter 3. Type III bursts are typically generated by electron beams travelling along 'open' magnetic field lines, whereas J and U bursts are the signatures of electron beams travelling along large-sized closed coronal loops.

The focus of this thesis is on exploring the following key topics:

- Investigating the kinetic properties of electron beam trajectories in the middle corona.
- Examining the physical parameters of expansive closed magnetic loops that extend to the middle corona.
- Assessing the ambient plasma density distributions (electron plasma density model) in the middle corona.

by conducting the three research projects detailed in Chapter 5,6,7.

To achieve the above goals, this thesis consists of three research projects analysing fast-drift solar radio bursts to diagnose electron beam trajectories, plasma density, and magnetic field properties in the middle corona. These studies take full advantage of the capabilities of LOFAR, which is recognized as one of the most advanced radio interferometers available, providing high temporal and frequency

resolution in dynamic spectrum and interferometric imaging data that were previously unavailable (the technology and features of LOFAR are introduced in Chapter 4). Moreover, the research presented in this thesis incorporates multi-wavelength observations from a range of instruments, both ground-based and space-based. This comprehensive methodology offers new strategies and case studies for investigating the aforementioned topics.

1.3 Thesis Outline

As a preface, this chapter offers a lay introduction to the Sun, crafted to assist in understanding the 'What' and 'Why' of the research presented in this thesis. Specific introductions of background knowledge and theories are in the upcoming chapters (Chapter 2, 3, 4), and the three research projects are introduced in three science chapters (Chapter 5, 6, 7).

Chapter 2 presents a review of the fundamental aspects of the solar atmosphere and its associated activities. These activities accelerate electron beams that generate solar radio bursts in the middle corona region, a key focus of study in this thesis.

Chapter 3 provides a review of the theoretical background pertinent to the physical processes behind radio wave generation by accelerated electron beams travelling along both 'open' and closed coronal magnetic flux tubes. Additionally, this chapter introduces various types of solar radio bursts and summarises the understanding in type III, J, and U bursts, as developed in previous studies.

Chapter 4 provides an overview of the instrumental background of this thesis. Specifically, it introduces the principles of the radio interferometry imaging technique that are essential for understanding how a radio interferometer like LOFAR produces solar interferometric imaging data. Additionally, this chapter introduces all instruments and data products involved in the conducted research projects in this thesis.

Chapter 5 introduces the study of a solar radio noise storm recorded on 10th April 2019 by LOFAR from 20 to 80 MHz, identifying 27 type III and 27 J bursts. It outlines a method for calculating beam velocities of J bursts using the 'classic method' from type III burst studies. A statistical analysis compares the exciter velocities of type III and J bursts, finding them similar. The chapter also proposes a novel approach for estimating loop-top plasma characteristics in the middle corona

using J burst data, revealing a decrease in plasma parameters with increasing loop height, aligning with previous findings on small loops. This sets the foundation for the methodologies employed in the discussed research projects.

Chapter 6, the second science chapter, introduces a high-resolution image (around 1 MHz^{-1}) of a large coronal loop, extending to the middle corona at 1.3 $R_{\odot}$ above the solar surface. The image was generated from LOFAR interferometric imaging data of a U burst observed between 20-40 MHz on June 5th, 2020. This study determined the electron beam's velocity variation from the up-flow to the down-flow leg on the radio image, noting an apparent velocity decrease. The ambient coronal plasma density and the physical parameters of the coronal loop from both legs were derived, revealing symmetrical physical properties across the loop.

Chapter 7, the third science chapter, presents a collaborative research project conducted by myself and experts specialising in solar microwave and X-ray analysis. This work introduces a novel approach to assess the coronal density model during flare events through the peak-to-peak delay between radio and microwave flux peak timings. This delay reflects the distance between the microwave and radio emission areas. Utilizing the e-Callisto spectrometer (e-Callisto ASSA station, Benz et al., 2005), four radio bursts between 15 to 86 MHz were identified on June 3, 2021 to analyze the velocity of electron beams accelerated by the flare and the density model above the flare region. The derived density model, enhanced by a factor of 10.5 over Saito's model (Saito et al., 1977), corresponds closely with the measured delay between microwave and radio flux peaks.

At the end of this thesis, Chapter 8 summarises the key findings and how they relate to the key scientific topics introduced in the preface chapter. The final chapter also recommends some future research ideas that will be undertaken to further our understanding of the solar middle corona through radio observations plus multi-wavelength studies, building upon the research introduced in this thesis.

Chapter 2

Solar Atmosphere

To lay the foundation for understanding the research presented in this thesis, this chapter provides an introduction to the Sun's atmosphere and activities, covering the following topics:

1. Different layers of the solar atmosphere.
2. The balance between plasma thermal pressure and magnetic pressure, represented by plasma β.
3. Corona plasma density models, including various famous numerical models developed by previous studies.
4. Coronal loops, the most essential magnetic structures in the solar atmosphere.
5. Solar flares, and the physical process of magnetic reconnection, which releases the stored magnetic energy and accelerates particles, including electron beams, generating radio flux.

2.1 Solar Atmosphere

2.1.1 Photosphere, Chromosphere and Transition Region

The Photosphere of the Sun, the innermost layer of the solar atmosphere, has a thickness of about 500 km and lies above the solar interior (Severino, 2017). Often referred to as 'the surface of the Sun', the Photosphere predominantly emits radiation in the visible wavelengths (400 - 700 nm), appearing as white light that can be directly observed with the human eye (Aschwanden, 2005). A defining characteristic of the Photosphere is its sharp gradient in plasma density, with a pressure scale

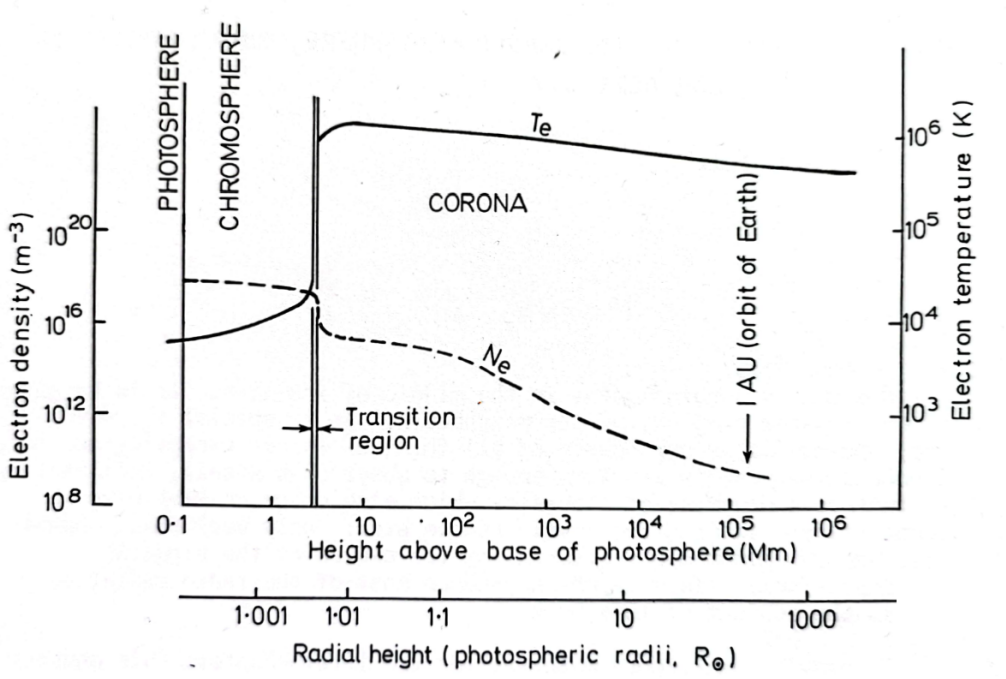

Figure 2.1: The electron plasma temperature (T_e) and density (N_e) exhibit variations from the Photosphere to the outer corona and beyond. The values of these parameters can significantly deviate due to solar activity and other influencing factors, as highlighted by the original source of this figure (Dulk (1985a)).

height of around 100 km. It also possesses the lowest temperature range among the layers of the atmosphere, varying roughly from 6,000 K to 4,000 K, as illustrated in Figure 2.1.

One of the most prominent phenomena in the Photosphere is the appearance of sunspots, temporary dark patches on the Photosphere. Easily observable in the visible spectrum, some larger sunspots can even be discerned from Earth without the aid of a telescope. The 'Yi Jing' ('Book of Changes') by the Chinese documented sunspots as far back as the 9th century BC. Galileo's telescopic observations of sunspots in 1611 marked the beginning of systematic sunspot observations (Bray & Loughhead, 1964; Hathaway & Wilson, 2004). The distinctive dark appearance of sunspots is due to their cooler temperature compared to the surrounding areas, a result of concentrated magnetic flux that inhibits convection. Sunspots are fundamental to understanding 'active regions' filled with intense magnetic loops, as they are the footpoints of emerging magnetic flux tubes. Typically observed in pairs, sunspots exhibit opposing magnetic polarities. The varying number of sunspots over time is a crucial measurement in defining the solar activity cycle, which fol-

lows an 11-year cycle ranging from minimum to maximum activity. From solar minimum to maximum, sunspots decrease in latitude. After the completion of this 11-year cycle, a new cycle begins, characterized by the reversal of the magnetic polarity of sunspots from the previous cycle. This phenomenon leads to a 22-year cycle of recurring magnetic polarity, a discovery made by Hale & Nicholson (1925). This cycle is referred to as Hale's cycle.

Above the Photosphere lies the Chromosphere, a layer approximately 2 Mm thick. As illustrated in Figure 2.1, the temperature in the Chromosphere begins to rise gradually while the density starts dropping. In the Chromosphere, the density scale height is between 100-200 km, decreasing faster than the magnetic fields in comparison to the Photosphere. This results in the plasma gas pressure becoming less dominant than the magnetic pressure in the upper chromosphere region, leading to a situation where the magnetic field starts to dominate (See review paper by Carlsson et al., 2019). This phenomenon is described by a physical parameter known as 'plasma β', which is discussed later in Section 2.2. Following the Chromosphere is the Transition Region, a thin layer about 100 km thick. This region experiences an irregular temperature surge, increasing sharply from the chromospheric temperature of approximately 2.5×10^4 K to around 10^6 K, marking the beginning of the corona (Golub & Pasachoff, 2009). In contrast to the temperature, the electron density in the Transition Region undergoes a sharp decrease, dropping by nearly two orders of magnitude. The reasons for these steep gradients in temperature and density in the Transition Region are not fully understood, constituting one of the most outstanding questions in solar physics for decades. This issue is often referred to as the chromospheric/coronal heating problem.

2.1.2 Solar Corona

The region above the Chromosphere and Transition Region is the solar corona, characterized by extremely high temperatures (approximately 1 MK) and low plasma density that decreases continuously with increasing altitude, as depicted in Figure 2.1. The coronal plasma is extremely tenuous, approximately 10^9 cm^{-3} at the base (Priest, 2014), and get less dense in higher altitude (see section 2.3). On normal days, due to the strength of the photospheric emission being extreme, this region is completely invisible to the naked eye and becomes visible in the optical band

only during a solar eclipse, appearing as a 'crown' around the shadowed moon disk (hence called 'corona' in Latin), as shown in Figure 2.2.

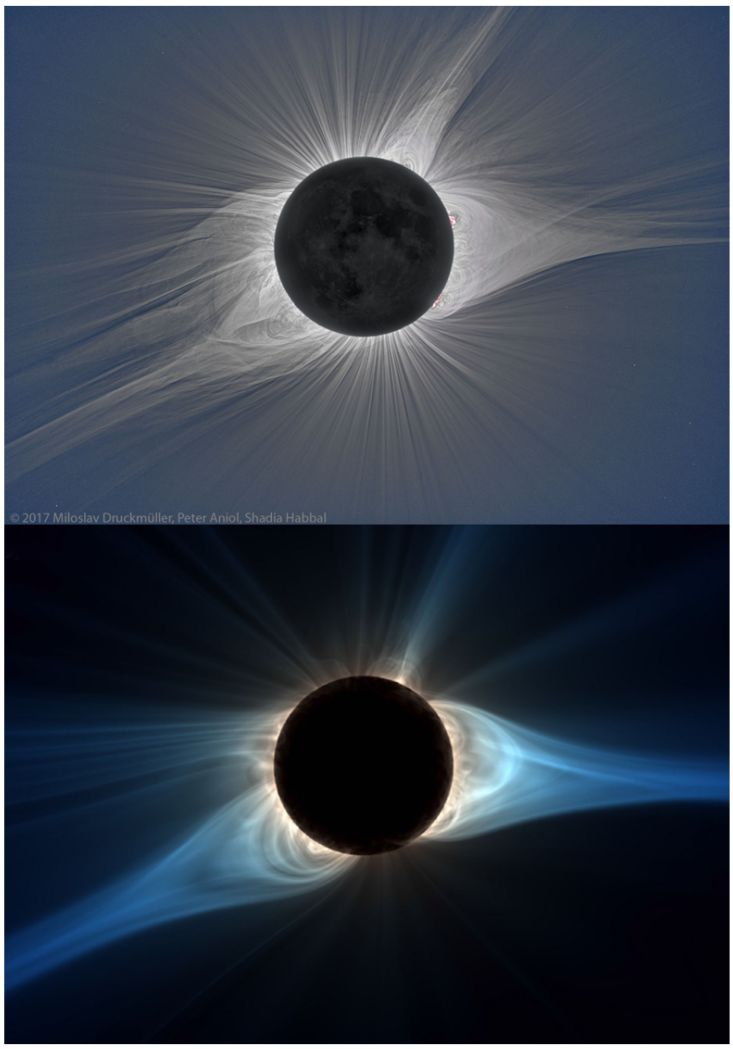

Figure 2.2: Top: A white-light photograph of the corona taken during the August 21, 2017 total solar eclipse. Coronal loops and 'open' magnetic field structures, named 'streamers', can be seen. (Credit: Miloslav Druckmüller, Peter Aniol, Shadia Habbal/NASA Goddard, Joy Ng.) Bottom: A simulated photo of the eclipse corona used for prediction (Published by Mikić et al. (2018)). Generated by using a 3D magnetohydrodynamic model and photospheric magnetic field measurements from the Helioseismic and Magnetic Imager (HMI) aboard Solar Dynamics Observatory (SDO).

The primary emission of the solar corona occurs in the Extreme Ultraviolet (EUV) and X-ray ranges. This is due to the corona being composed of extremely high-temperature, fully ionized gas, referred to as 'coronal plasma,' which can efficiently interact with coronal magnetic fields (Dulk, 1985a; Golub & Pasachoff, 2009). EUV and X-ray coronal emissions are observable by spacecraft positioned outside Earth's atmosphere. These observations are conducted across various wave-

Channel	Primary ion(s)	Region of atmosphere	Char. log(T)
4500 Å	continuum	photosphere	3.7
1700 Å	continuum	temperature minimum, photosphere	3.7
304 Å	He II	chromosphere, transition region	4.7
1600 Å	C IV + cont.	transition region, upper photosphere	5.0
171 Å	Fe IX	quiet corona, upper transition region	5.8
193 Å	Fe XII, XXIV	corona and hot flare plasma	6.2, 7.3
211 Å	Fe XIV	active-region corona	6.3
335 Å	Fe XVI	active-region corona	6.4
94 Å	Fe XVIII	flaring corona	6.8
131 Å	Fe VIII, XXI	transition region, flaring corona	5.6, 7.0

Table 2.1: Primary ions, the atmosphere regions and characteristic emission temperatures, in Kelvin, for each SDO AIA band pass. The original table illustrating this data can be found in Lemen et al. (2012).

lengths, including different Atmospheric Imaging Assembly (AIA, see: Lemen et al., 2012). These passbands are generated by specific primary emitting ions and correspond to their characteristic temperatures, as detailed in Table 2.1. Through EUV and X-ray observations, the solar corona is revealed to be an extremely inhomogeneous medium, with some regions significantly brighter than others. For the purpose of studying the corona, it is generally divided into three different 'regions': (a) Active regions; (b) Coronal holes; (c) Quiet corona. Figure 2.4 displays labeled examples of these three types of regions on a 171 Å AIA solar corona image, by Cargill & de Moortel (2011). In this thesis, I used the EUV solar images (mainly the 171 Å channel) captured by SDO AIA for displaying the solar disk and the solar corona. As it doesn't involve analysis on AIA EUV data, there is no additional introduction to this instrument in Chapter 4.

2.1.2.1 Active regions, Quiet corona and Coronal holes

The solar Active Region (AR), also sometimes referred to as the 'Centre of Activity', is defined by the totality of observable phenomena within a three-dimensional volume (For a detailed review of ARs, see: van Driel-Gesztelyi & Green, 2015). This volume is represented by the extension of the magnetic field from the photosphere to the corona. ARs are revealed by emissions over a wide range of wavelengths, from radio to X-rays, accompanying and following the emergence of strong, twisted magnetic flux (kG, $\geq 10^{20}$ Mx) through the photosphere into the chromosphere and corona. These observable phenomena include the presence of

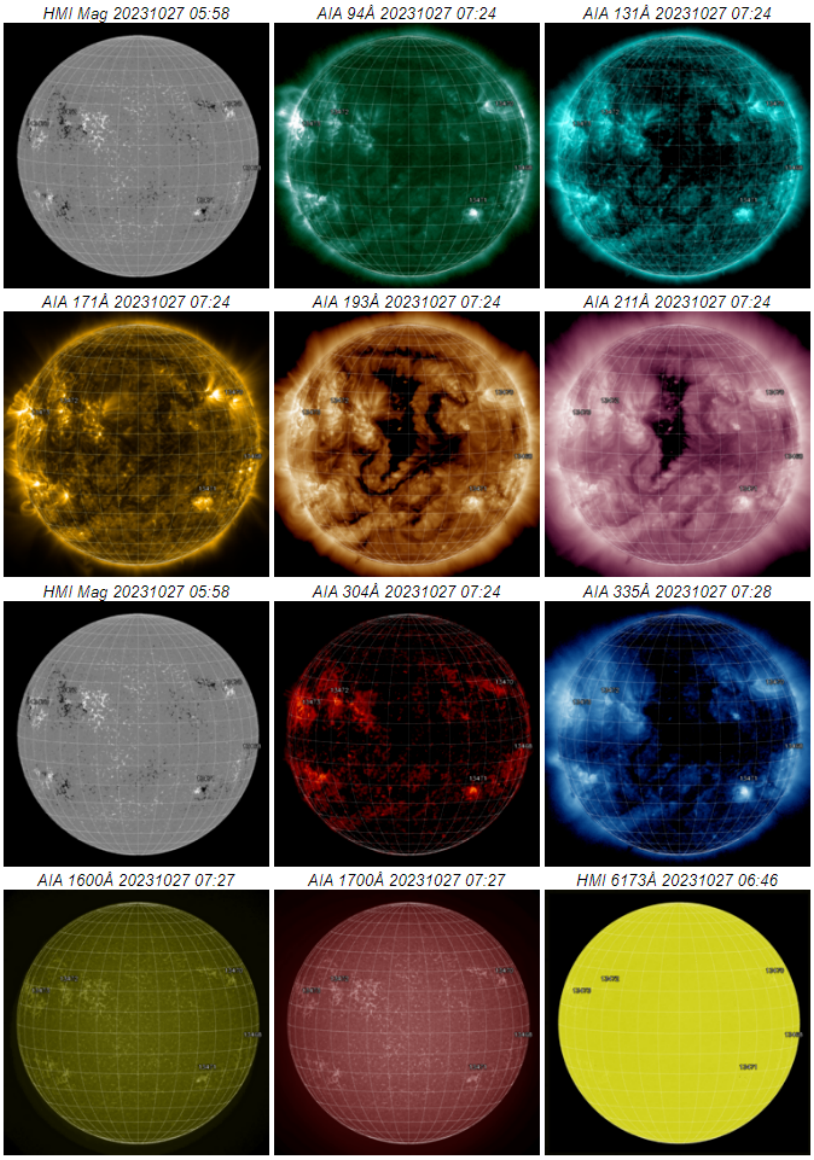

Figure 2.3: Vibrant full-disk images of the sun are captured by the Atmospheric Imaging Assembly (AIA) and the Helioseismic and Magnetic Imager (HMI) onboard the Solar Dynamics Observatory (SDO) spacecraft. The AIA provides observations of the solar atmospheric layers—the chromosphere and the corona—in seven channels within the extreme ultraviolet (EUV) spectrum. Meanwhile, the HMI observes the solar disk at 6173 Å (Angstrom unit, $1\mathring{A} = 10^{-10}$ meter), studying oscillations and the magnetic field at the solar surface, known as the photosphere. It's important to note that these 'colors' of solar images are rendered in pseudo-color for display purposes, as they represent wavelengths shorter than the visible spectrum and are, in fact, invisible to the human eye. These images are downloaded from the SolarMonitor website, developed by a team from Dublin & the Dublin Institute for Advanced Studies. (Accessed date: 2023-10-27).

sunspots on the Photosphere, which are the footpoints of strong magnetic flux tubes emerging from the solar interiors, beyond the Photosphere. In the Corona, ARs

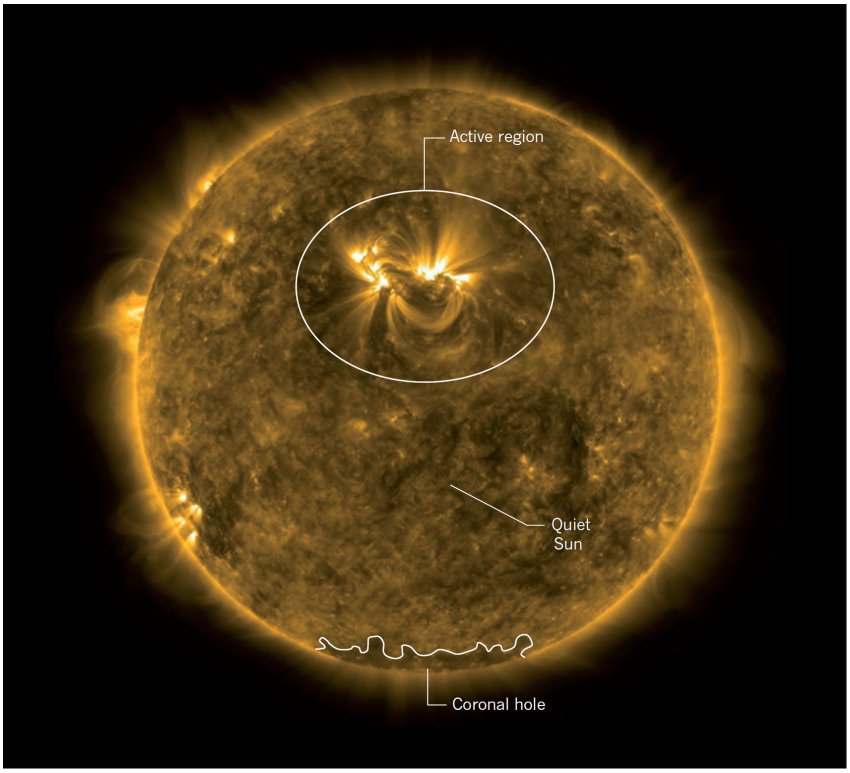

Figure 2.4: AIA image of solar corona at 171 Å with labelled active region, quiet corona and coronal hole. Taken from Cargill & de Moortel (2011).

comprise large groups of strong magnetic loops characterized by complex evolutionary geometrical structures. These coronal loops, connecting opposite magnetic polarities, trap hot plasma and appear bright across a range of wavelengths from X-rays to radio frequencies (due to Plasma $\beta < 1$, explained in Section 2.2). Typically, these loops are hotter and denser than the average solar regions, often referred to as the 'Quiet Corona', because they experience relatively less loss in both mass and thermal energy (Reale, 2014).

The Quiet Sun is defined as the region of the solar surface that is outside of extreme solar activities, Active Regions (ARs), and areas dominated by open magnetic fields, commonly referred to as 'coronal holes'. In the Photosphere and Chromosphere, the Quiet Sun is characterized by the absence of sunspots, pores, and plages (Bellot Rubio & Orozco Suárez, 2019). In the coronal region, known as the Quiet Corona, there is typically a lack of large-scale hot and intense magnetic loops or significant energy release activities.

Coronal holes are identifiable as regions darker than the surrounding corona background in coronagraph images, as shown in Figure 2.4. The defining character-

istic of coronal holes is their 'open' magnetic field configuration, in contrast to the typical closed bipolar magnetic flux tubes that emerge from the interior and make up other coronal structures such as Active Regions (ARs) and the Quiet Corona Golub & Pasachoff (2009). The plasma within coronal hole regions interacts with and propagates within extremely large-scale solar magnetic structures that extend far into interplanetary space, effectively making them open. Since plasma and particles escape more efficiently along these open field lines, the temperature and density of plasma in coronal holes are lower compared to regions where magnetic field lines are closed (see review by Cranmer, 2009). This lower temperature and density characteristic explains why coronal holes appear darker in EUV and X-ray ranges compared to ARs and Quiet Corona regions.

2.1.3 The Inner Corona: Home of coronal loops and solar activities

The inner corona, defined by solar altitudes below 1.5 $R_\odot$ heliocentric distance, is largely composed of closed magnetic structures, excluding the coronal hole regions. Primarily observed in X-ray and EUV bands, the corona's imagery is constructed from bright closed coronal magnetic loop structures, flares, and active regions with strong magnetic fields.

Coronal loops are brighter than the surrounding area because the plasma traveling along the closed magnetic fields ($\beta < 1$) gets trapped, resulting in higher density and more heating compared to the surrounding plasma. Since the intensity of radiation is proportional to the square of the plasma density at a given temperature (based on theories of the intensity of spectral lines), the plasma in the closed loops becomes much brighter than the surroundings, making the closed magnetic structure visible in X-ray and EUV images. In the review paper on X-ray/EUV corona loops by Reale (2014), these loops in the inner corona region are classified as hot, warm, and cool loops depending on their temperatures.

In the inner corona region, not all coronal magnetic loop structures emit intense X-ray and EUV emissions detectable by space-based spectroscopy. However, some of these loops generate radio emissions observable by ground-based interferometers while electron beams travel along these loops. For example, a U burst observed on March 22, 2011, by the Nançay Radioheliograph (NRH) was imaged by Mancuso

et al. (2023) at frequencies of 298.7, 327.0, and 360.8 MHz. The source positions of this burst mapped a closed magnetic loop structure, which was overplotted on the EUV intensity map at 171 Å obtained by the SDO for the same observational time, as shown in Figure 2.5. The imaged loop was identified at an altitude of 0.21 $R_\odot$ within the inner corona, and there were no reliably identified EUV loops in any of the available SDO/AIA EUV channels. As the solar altitude increases, large-scale loops become fainter in X-ray and EUV emission lines due to the lower plasma density, and the diagnostic power of radio emissions from coronal loops becomes more pronounced.

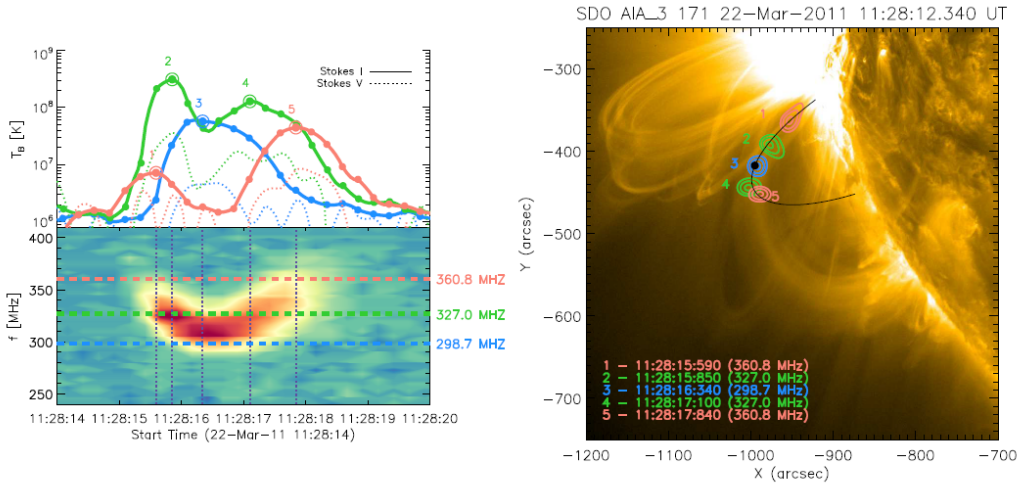

Figure 2.5: Left: Spectral data of a type U burst collected by the e-Callisto spectrometer during the emission (bottom), along with temporal profiles of the radio brightness temperature based on NRH observations (top). Right: Radio source positions were imaged by the NRH at the intensity peaks at 298.7, 327.0, and 360.8 MHz, as labeled on the left panel. An SDO/AIA image taken at 171 Å on March 22, 2011, at 11:28 UT shows the coronal configuration during the type U radio emission. Both figures are taken from Mancuso et al. (2023), as they worked on imaging this example U burst.

2.1.4 The Middle Corona: Transition from closed loops to 'open' magnetic fields

The distinction between the inner, middle, and outer corona has grown increasingly significant recently, with each exhibiting distinct characteristics. The middle corona, as defined by West et al. (2023), spans a heliocentric distance from 1.5 to 6 $R_\odot$. This region serves as a critical bridge between the distinct physical regimes of the inner and outer solar corona.

The key feature of the middle corona is the transition of magnetic flux tube structures from being predominantly closed, as seen in the inner corona, to 'open' fields, characteristic of the outer corona. Outside of coronal holes regions, this transition occurs almost entirely within the middle corona, leading to interactions between 'open' fields and large-sized coronal loops. Recent observations and studies show that the acceleration of the solar wind begins in this region, driven by magnetic field interactions and complex plasma dynamics (See Wexler et al., 2020; Raouafi et al., 2023).

To fully understand the mechanisms behind large-scale coronal magnetic field interactions and plasma outflows and inflows, essential for understanding the birth of 'young solar wind', it is highly demanded to develop models that encompass an extremely diverse set of conditions (Verscharen et al., 2019). The plasma conditions and large-scale magnetic field properties within the middle corona are important for developing such models. However, they remain ill-defined due to historical observational limitations, as the low plasma density in this region results in X-ray and EUV emissions that are challenging to detect compared to the lower solar atmosphere. Seaton et al. (2023) provided a detailed summary of the key questions that remain unclear regarding the middle corona and suggested multi-wavelength observations as strategic recommendations to address outstanding questions about this region of the corona. Nevertheless, radio emissions, generated by accelerated electron beams traveling along magnetic flux tube structures at frequencies equal to or double the background plasma frequency, serve as a crucial diagnostic tool (this is the 'plasma emission mechanism', detailed in the next chapter, section 3.1.2). Solar radio observations enable the tracing of electron beam trajectories and probing of the plasma conditions and magnetic field properties within the middle corona. Notably, fast drift radio bursts (type III, J, and U bursts) are instrumental in:

1. Outlining the geometry of the fast-electron-beam-conducting magnetic field lines threading through the corona.

2. Probing the background corona electron plasma density distribution along the fast-electron-beam-conducting magnetic field lines, which includes both open and closed magnetic flux tubes.

3. Measuring the velocities of fast-electron beams.

This aspect forms the core focus of the study presented in this thesis.

2.1.5 Heliosphere and Solar Wind

Above the middle corona lies the outer corona, defined by the dominance of open magnetic fields that connect to the heliosphere and are observed to be fully radial in structure (for example, see McGregor et al., 2008). The plasma β conditions in the outer corona vary widely, ranging from less than 1 to greater than 1, depending on the event and local conditions. The solar wind is characterized by accelerated energetic particles and plasma frozen in these outwardly propagating open flux tubes. Furthermore, the rotating spiral structure of the magnetic field in the interplanetary medium, as described by Parker (1958), is the well-known 'Parker Spiral'.

The solar wind in the outer corona and the interplanetary medium can be observed through either in-situ measurements or remote sensing. Instruments such as the Parker Solar Probe (PSP) with its Solar Wind Electrons Alphas and Protons (SWEAP) instrument (see Kasper et al., 2016), as well as the Solar Orbiter (SolO) equipped with the Solar Wind Plasma Analyser (SWA) (see Owen et al., 2020) and Energetic Particle Detector (EPD) (see Rodríguez-Pacheco et al., 2020), are specifically designed to take in-situ measurements of the energy, density, velocity, and temperature of electrons and ions that constitute the solar wind and coronal plasma in the outer corona region and the interplanetary medium. The radio emissions in the high solar altitude atmosphere are primarily generated through the plasma emission mechanism in the low-frequency range, which is undetectable by ground-based observatories due to the atmospheric window. In-situ instruments such as the Electromagnetic Fields Investigation (FIELDS) (see Pulupa et al., 2017) onboard the PSP, and the Radio and Plasma Waves (RPW) (see Maksimovic et al., 2020) onboard the SolO, are designed to observe interplanetary radio bursts below 10 MHz. These bursts originate in the outer corona and beyond and are powerful diagnostic tools for the interplanetary magnetic field structure. For example, Chen et al. (2023b) used multiple space-based interplanetary type-III burst measurements (from PSP, SolO, WIND, STEREO) to determine the electron beam propagation path along the Parker Spiral structure.

In this thesis, we utilize both space-based radio observations below 10 MHz

and ground-based radio measurements between 10 to 90 MHz to trace the electron beam propagation from the middle to the outer corona and beyond. This propagation is the origin of type III solar radio bursts and can be used for radio burst classification, as discussed in Chapter 5.

2.2 Plasma β

The behaviour of an important physical parameter is noticeable across the full range of the solar atmosphere: the plasma β. This parameter describes the balance between the plasma thermal pressure and the magnetic field pressure, as defined by Equation 2.1:

$$\beta = \frac{P_{\text{thermal}}}{P_{\text{mag}}} = \frac{2N_e K_b T}{B^2/8\pi} \tag{2.1}$$

where P_{thermal} represents the thermal pressure, and P_{mag} denotes the magnetic pressure. Here, N_e is the electron plasma number density, K_b is the Boltzmann constant, T is the plasma temperature, B is the magnetic field strength.

When the plasma $\beta > 1$, the plasma pressure exceeds the magnetic pressure under local conditions. This indicates that plasma dynamics dominate over magnetic fields. Conversely, when the plasma $\beta < 1$, the magnetic pressure dominates. In this scenario, energetic particles and hot plasma are 'frozen' into the magnetic flux tubes, implying they can only travel along the magnetic field lines.

The distribution of plasma β across the solar atmosphere is illustrated in Figure 2.6. Plasma β decreases from the photosphere (where $\beta > 1$) to the chromosphere and transition region, which have the lowest average plasma β, with $\beta \ll 1$. Then, from the transition region to the corona, β begins to increase towards 1. Note that plasma β varies from structure to structure within the solar atmosphere.

2.3 Corona Plasma Density Models

The radial distribution of plasma density in the solar atmosphere has been extensively studied since the early stages of solar physics. The density distribution along the solar altitude is particularly important in solar radio studies, especially for low-frequency solar radio emissions, which are the core focus of this thesis.

Through the plasma emission mechanism, electron beams travelling along

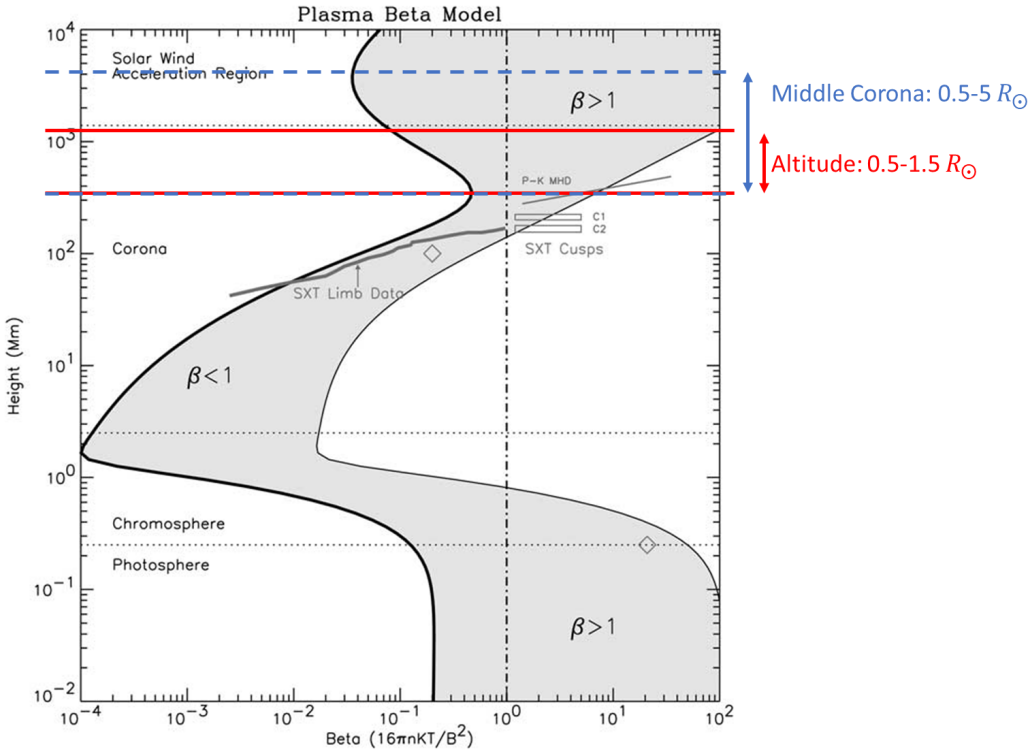

Figure 2.6: The variation of plasma β over the active region is given by Gary (2001). The altitude range of 0.5-1.5 $R_\odot$ is labeled on this plot between red solid lines. This region represents the beginning of the Solar Middle Corona (range between blue dashed lines, 0.5-5 $R_\odot$), which this thesis analyses using radio emissions between 20 to 80 MHz. Plasma β in the solar atmosphere is not uniform, even at the same height. It varies based on the structure and specific events occurring within the atmosphere.

magnetic flux tubes generate electromagnetic waves at frequencies equal to or double the local background plasma frequencies. The plasma frequency is proportional to the square root of plasma density, as defined by the following equation:

$$f_e = (4\pi n_e e^2/m_e)^{1/2}/2\pi = 8.98 \times 10^3 {n_e}^{1/2} \tag{2.2}$$

Where: f_e is the electron plasma frequency, n_e is the electron plasma density, and m_e is the electron mass.

This definition allows us to convert the frequency profile of the observed solar low-frequency radio waves to the radio source's local background plasma frequency and, therefore, determine the corresponding plasma density.

The density can then be further converted to radial height in the solar corona using the numerical coronal density models introduced later in this section. This approach is applicable in cases where the electron beam travels outward radially,

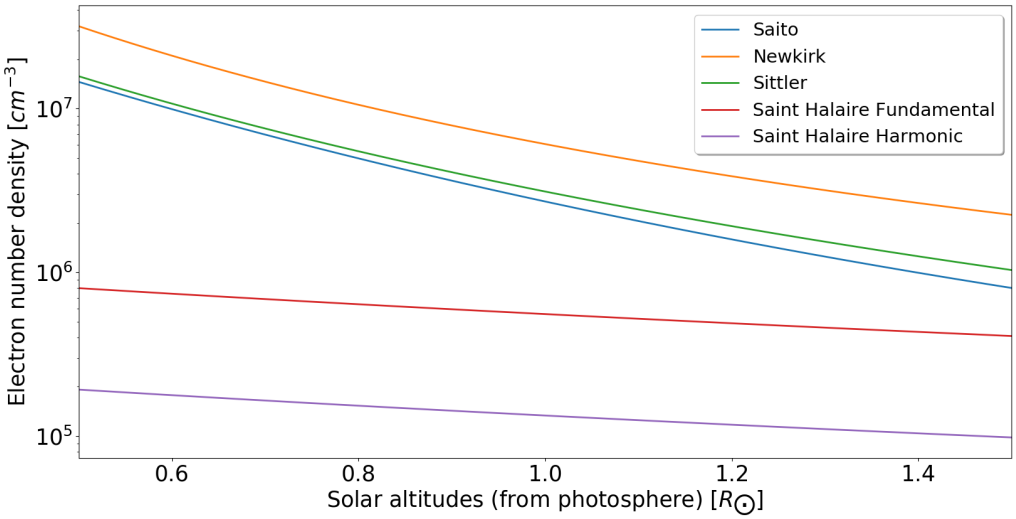

Figure 2.7: Plots of numerical coronal electron plasma density distribution models introduced in this section are provided for Newkirk (Newkirk, 1961), Saito (Saito et al., 1977), Sittler (Sittler & Guhathakurta, 1999), and Saint-Hilaire (Saint-Hilaire et al., 2013). The y-axis represents the electron plasma number density, while the x-axis, ranging from 0.5 to 1.5 $R_\odot$ above the photosphere, corresponds to the altitude and covers the middle corona region studied in this thesis.

as is typical for the generation of type-III solar radio bursts (see section 3.2.1 and corresponding sections that determine electron beam velocities in Chapters 5, 6, and 7 for more details).

Newkirk's model:

Models of the coronal electron density are typically described as a function of solar altitudes. Newkirk (1961) derived a model of electron density in the corona above an active region based on K-corona observations made in Climax, Colorado. This model describes electron plasma density distributions spanning the altitude from the solar photosphere up to 1 $R_\odot$, which overlaps with the bottom of the middle corona region (above 0.5 $R_\odot$) that we are investigating in this thesis (see Figure 2.7, 0.5 - 1.5 $R_\odot$).

Newkirk's coronal density model is described by the following expression:

$$N_Q = N_0 \times 10^{4.32/R} \tag{2.3}$$

Where: N_Q is the electron density over the quiet Sun, $N_0 = 4.2 \times 10^4$ cm^{-3}, and R is the distance in units of $R_\odot$ from the centre of the Sun.

Saito's model:

By analysing white-light coronagraph data from Skylab, Saito Saito et al. (1977) investigated a solar coronal electron density model based on coronal brightness and polarization between 2 and 6 $R_\odot$ heliocentric distance. Saito presented the model across three different scenarios: (1) data unaffected by streamers or coronal holes, referred to as the background model; (2) cases where coronal holes were present on the limb; and (3) cases in polar regions. The widely used background model, also employed in this thesis, describes the solar coronal electron density distribution, $N_e(r)$, by the following expression:

$$N_e(r) = 1.36 \times 10^6 \times r^{-2.14} + 1.68 \times 10^8 \times r^{-6.13} \tag{2.4}$$

Where: r is also the heliocentric height given in units of $R_\odot$.

Saito's model, with a multiplier range from 2.5 to 10.5, is primarily used in this thesis for determining electron beam velocities. Additionally, Saito's model with various multipliers has been employed to describe the inferred coronal density models by using low-frequency solar radio bursts observations in the MHz range, particularly for type III bursts (see section 3.2.1). For instance, Reid & Kontar (2017) inferred the coronal density model as Saito's model times 4.5, based on solar radio images of three U-bursts between 20 to 80 MHz. Similarly, Carley et al. (2016) determined the coronal density distributions to be at a magnitude of 11.5 times Saito's model by imaging a Flare Continuum B and the type III group.

Sittler's model:

Sittler & Guhathakurta (1999) developed a coronal plasma density model using white-light coronagraph data measured by Skylab. Originally, this model was developed by Guhathakurta et al. (1996), utilising the hydrostatic equilibrium solution. Sittler & Guhathakurta (1999) refined this electron density model to fit the observed electron density profile along the solar equatorial plane by Skylab coronagraph observations and in-situ solar wind measurements by Ulysses (Phillips et al., 1995), covering from the bottom of the corona to 1 AU. The solar coronal electron density distribution, $N_{cs}(z)$, is described by the following expression:

$$N_{cs}(z) = a_{cs1} e^{a_{cs2} z} z^2 (1 + a_{cs3} z + a_{cs4} z^2 + a_{cs5} z^3) \tag{2.5}$$

Where: $N_{cs}(z)$ is the electron density variation along the distance z (heliocen-

tric, units in $R_\odot$) in equatorial current sheet regions. The values of the coefficients are as follows: $a_{cs1} = 3.2565 \times 10^{-3}$; $a_{cs2} = 3.6728$; $a_{cs3} = 4.8946$; $a_{cs4} = 7.6123$; $a_{cs5} = 5.9868$.

Saint-Halaire's model:

Developed by Saint-Hilaire et al. (2013), this model is based on a statistical survey of 10,000 type III radio bursts observed by the Nançay Radioheliograph from 1998 to 2008. Saint-Hilaire assumed that emission occurs either at the fundamental or at the second harmonic of the local plasma frequency, and then derived the normalization constant C for the 'solar wind-like' atmosphere model by Cairns et al. Cairns et al. (2009):

$$N(h) = C(h)^{-2} \tag{2.6}$$

Where: h is the coronal altitude above the photosphere, measured in units of $R_\odot$. Under the assumption of fundamental emission, $C = 5 \times 10^6$ cm^{-3}, and under the assumption of second-harmonic emission, $C = 1.2 \times 10^6$ cm^{-3}.

2.3.1 Hydrostatic Scale Height

In the field of planetary sciences, the term 'scale height' refers to the radial distance over which a specific physical quantity in a planet or star's atmosphere decreases by a factor of 'e' (the base of natural logarithms, approximately 2.718). Notably, the density scale height in the solar corona is exceptionally large, estimated at around 50,000 km (Aschwanden, 2005). This is significantly greater than the Earth's atmospheric scale height, which is approximately 8.5 km. The vast difference is attributed to the solar atmosphere's higher temperature and its tenuous plasma environment. For quantitative analysis of phenomena in the solar corona, such as coronal loops, understanding the basic physical parameters, including temperature, density, and pressure, is crucial. The concept of hydrostatic scale height is instrumental in understanding the relationship between these parameters, describing the balance of pressure against gravitational force under the assumption of a constant temperature (isothermal approximation). Dynamic phenomena within the solar corona often progress towards a stable equilibrium. Consequently, most coronal structures are predominantly found in or near a stationary state, and these physical parameters

are indispensable for performing diagnostics based on observed emissions in the EUV, soft X-ray, or radio frequencies.

The formula for calculating the density scale height, λ, of coronal plasma in thermal equilibrium is given by:

$$\lambda = \frac{1+\alpha}{\beta} \cdot \frac{k_B T}{m_P g_\odot}, \tag{2.7}$$

where $\alpha = 1.22$ represents the ratio of electron to proton number, and $\beta = 1.44$ denotes the mean molecular weight. k_B is the Boltzmann constant, m_P refers to the mass of a proton, and $g_\odot$ signifies the gravitational acceleration, given by:

$$g_\odot(r) = \frac{GM_\odot}{r^2}, \tag{2.8}$$

where G is the gravitational constant, 6.6726×10^{-8} dyne cm^{2}g^{-2}, $M_\odot$ is the mass of the Sun, 1.99×10^{33} g, and r is the distance from the centre of the Sun.

It is important to note that within the middle corona range, $g_\odot$ does not remain constant but varies with altitude. A primary focus of this thesis is the use of hydrostatic equilibrium for deriving the physical parameters of large-sized coronal loops. The plasma temperature distributions within these loops have been determined by inferring the ambient plasma density distribution model. This model yields a scale height λ, at constant, which is then used alongside the value of gravitational acceleration at the certain radio source heights to gain insights into these coronal structures. This methodology will be detailed in Science Chapters 1 and 2 (see sections 5.5.2).

Ideal Gas Law

The Ideal Gas Law is a thermodynamic equation of state that describes the relationship between the gas pressure P, the number density n, and temperature T, as follows:

$$P = nk_B T, \tag{2.9}$$

The Ideal Gas Law is widely used to determine the plasma gas pressure in coronal magnetic flux tubes in previous studies (e.g. Aschwanden et al., 1992), and is utilised in defining the solar atmosphere's hydrostatic scale height (see section 3.1 of the book by Aschwanden, 2005).

2.4 Coronal Magnetic Loops

Coronal loops have been the subject of in-depth studies for about 60 years. Since the first X-ray coronal magnetic loops were identified by Vaiana et al. (1968), these loop structures have been commonly accepted as the building blocks of the bright solar corona. As introduced in Section 2.1.3, coronal loops are characterised by their bright arch shapes, due to the plasma being confined within them and isolated from the surroundings. They exhibit a variety in temperature. Thermal coronal loops classified as Cool (0.1-1MK), Warm (1-1.5 MK), and Hot (greater than 2 MK) (Reale, 2014), and size (in the X-ray band, coronal loops span more than two orders of magnitude in size, and in the radio range, even more). By classifying coronal loops by size, from relatively small to large as observed in the soft X-ray band, a summary of typical coronal loop physical parameters (loop length, temperature, density, and pressure) was summarised by Reale (2014) in Table 2.2.

Soft X-ray emissions of the solar corona, with wavelengths between 1 to 100 Å, corresponding to thermal energies of 0.1 to 10 keV and plasma temperatures between 1.5 to 150 MK, are ideally suited for observing plasma in active regions between 1 to 10 MK, and in flaring loops that exceed 10 MK to 50 MK and beyond. Soft X-ray emissions are generated by free-free emission of electrons that are scattered off highly-ionized ions in the corona (see Bremsstrahlung emission in Section 3.1.1).

EUV radiations of coronal loops are produced through the same mechanism, with electron scattering off ions at relatively lower temperatures than in the soft X-ray case. EUV bands cover wavelengths from 100 to 1000 Å and correspond to plasma temperatures between 0.15 to 1.5 MK, making them excellent for observing warm coronal loops almost everywhere in the quiet corona and active regions.

Type	Length $[10^9 cm\ (10Mm)]$	Temperature $[MK]$	Density $[10^9 cm^{-3}]$	Pressure $[dynecm^{-2}]$
Bright points	0.1 - 1	2	5	3
Active region	1 - 10	3	1 - 10	1- 10
Flaring loops	1 - 10	> 10	> 50	> 100
Giant arches	10 - 100	1 - 2	0.1 - 1	0.1

Table 2.2: Coronal loops' physical parameters summarised by Reale (2014). From different regions, and in various size, temperature, density and pressures.

Bright points, which are warm and hot coronal loops (always a small region of bright bipolar field), are less than 10^9 cm in length, and were originally identified as one of the soft X-ray structures by Vaiana et al. (1973) using a Kanigen-coated telescope from a series of rocket missions. The active region and flaring loops are signatures of relaxation from flare-related magnetic reconnection processes, which we will discuss later. They are filled with accelerated, heated plasma and are therefore typically high in temperature, with most classified as hot loops.

Giant arches, extending towards the middle and upper corona region, exist and have been confirmed by many observations. For instance, the EUV observation of the growth of post-flare giant arches and their fading was documented by West & Seaton (2015). Large-sized coronal loops, greater than one solar radius, are rarely seen in the X-ray or EUV range due to the tenuous plasma and temperature. The accelerated electrons propagate along these large magnetic arches, generating radio wave emissions via a coherence emission mechanism (see the plasma emission mechanism detailed in Section 3.1.2). Studying the physical properties of these giant arches by analysing corresponding radio emissions is precisely one of the key objectives and the focus of this thesis, as mentioned earlier.

2.5 Magnetic Reconnection

The solar corona is dynamically shaped by three primary boundary conditions (see Aschwanden, 2005):

1. The generation of new magnetic flux by the solar dynamo from the tachocline, which rises into the corona;

2. The constant twisting of the coronal magnetic field due to the Sun's differential rotation and surface convective motions;

3. The need for continual reconfiguration with the interplanetary magnetic field to avoid excessive magnetic stress.

These factors collectively lead to a state where the coronal magnetic field is under constant strain, necessitating adjustment and restructuring. This restructuring is predominantly achieved through magnetic reconnection, a process where magnetic field lines rearrange themselves and release energy. Magnetic reconnection is not

limited to specific areas; it can occur wherever magnetic stresses accumulate, such as in the transition region's divergent fields, tangled fields in active regions, and at coronal hole boundaries. Magnetic reconnection not only transforms non-potential energy into plasma heating and kinetic energy but also triggers activity events like solar flares and coronal mass ejections, making it a central aspect of the diverse and dynamic phenomena observed in the solar corona.

One of the most fundamental conceptual models of magnetic reconnection is the steady 2D model, also known as the Sweet-Parker model, which was first formulated by Parker (1957); Sweet (1958). This model has been instrumental in many theoretical studies of coronal heating (which explore the reasons behind the corona's high-temperature nature, e.g. Parker, 1963, 1972, 1983; Sturrock & Uchida, 1981; van Ballegooijen, 1986) and solar flares (e.g. Sweet, 1958; Petschek, 1964; Carmichael, 1964; Sturrock, 1966; Hirayama, 1974; Kopp & Pneuman, 1976). The model (see part (a) in Figure 2.8) describes a process that occurs when two different magnetic systems come into contact, such as when a new oppositely directed magnetic field emerges from the Sun and interacts with an existing magnetic field in the solar atmosphere. At the point where these two systems meet, there is a boundary known as the diffusion region (red coloured region in the sketch), with the magnetic field's direction being opposite on each side of it. These two opposite magnetic fields, with plasma of density ρ and conductivity σ, are carried toward the neutral line (as the magnetic field strength tends to zero near the neutral line at the centre of the diffusion region) at a speed v_{in} over a characteristic distance $2L$, and the width of the diffusion region is 2σ. This is where the magnetic field changes connectivity (a positive polarity flows to a different negative polarity). In the diffusion region, the plasma β increases to greater than unity ($\beta > 1$) due to the decrease in magnetic field magnitude, allowing the plasma to flow across the field lines rather than being frozen into the original field. The reconnected field and plasma are then channelled outwards from the diffusion region with speed v_{out} along the direction shown in part (a) of Figure 2.8, driven by the inward-directed magnetic pressure force outside the diffusion region and the outward-directed magnetic tension force. This process is termed the slingshot effect and represents the fundamental conversion mechanism from magnetic to kinetic energy (Aschwanden,

2005; Zweibel & Yamada, 2009).

In the Sweet-Parker reconnection model, the diffusion region has a rectangular shape where the characteristic distance $2L$ (length) is greater than the conductivity 2σ (width). This configuration results in the fluid brought into the diffusion region having to flow out through a thin resistive channel, which causes the reconnection rate to be too slow to explain the typical flare event that involves faster energy release (Aschwanden, 2005). Petschek (1964) proposed a model with a reduced size of the diffusion region, where the characteristic distance is much shorter than in the Sweet-Parker model (see part (b) in Figure 2.8). In Petschek's model, the propagation time of the reconnected field and plasma through the diffusion region is shorter, making the reconnection process faster. If the length L is replaced by a shorter length L', the reconnection rate is increased by $\sqrt{L/L'}$ (see Zweibel & Yamada, 2009). As introduced by Aschwanden (2005), the Petschek reconnection rate is about three orders of magnitude faster than that of the Sweet-Parker model. Therefore, Petschek's model is widely used in explaining fast reconnections, such as those occurring in solar flares.

Apart from the two reconnection models introduced above, there are more complex models that transition from 2D to 3D and from steady to unsteady states. 3D reconnection models exhibit a much richer variety in the geometry of the two or more opposing magnetic field structures in 3D space. For example, 3D X-type reconnections, as introduced by Aschwanden (2005) Section 10.3.1, describe cases of bipolar, tripolar, and quadrupolar magnetic reconnection topologies. These 3D models are more commonly required in the study of solar flares, as sheared and twisted magnetic field configurations are more prevalent during such events.

Since magnetic reconnection models are not the focus of this thesis, interested readers are referred to Aschwanden (2005), Chapter 10.3, for a detailed and comprehensive introduction to 3D reconnection models (Chapter 10 reviews the entire topic of magnetic reconnections in solar atmosphere studies). However, one concept remains unequivocally clear and critical to this study: the magnetic reconnection process converts stored magnetic energy into the kinetic energy of energetic particles, accelerating them to high energies. These accelerated electrons, in turn, produce radiation across a broad electromagnetic spectrum range, including radio

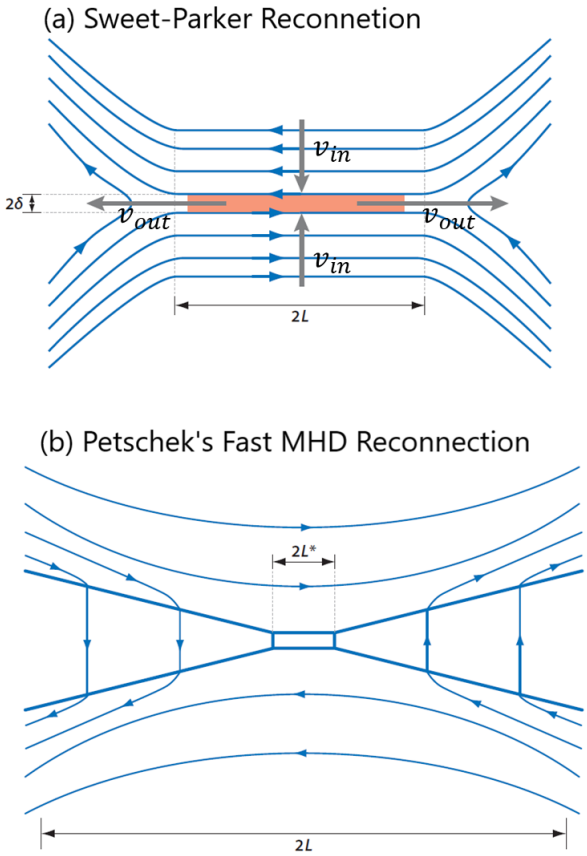

Figure 2.8: Cartoons of two magnetic reconnection 2D models. (a): The Sweet-Parker reconnection model (Parker, 1957; Sweet, 1958), which features a rectangular-shaped diffusion region. Model (b) is Petschek's model (Petschek, 1964), characterised by a shorter diffusion region and capable of explaining the fast energy release phenomena observed in the solar atmosphere. Cartoons credit to Zweibel & Yamada (2009).

waves (see Chapter 3), which are intensely studied in this thesis.

Flare

Solar flares are magnetically driven explosive events caused by the magnetic field above the solar surface becoming unstable and the sudden release of magnetic energy through the magnetic reconnection process. The previously unstable, stressed magnetic fields transform to a lower energy and more relaxed topology, releasing energy into the surrounding and confined plasma in the solar atmosphere, which accelerates particles to very high speeds to the quasi-thermal level (Holman et al., 2011). Although there is no 'uniform' flare, a typical one can release as much as 10^{32} erg of energy (Emslie et al., 2004). The most commonly observed accelerated particles in a solar flare are electrons (electron beams), which gener-

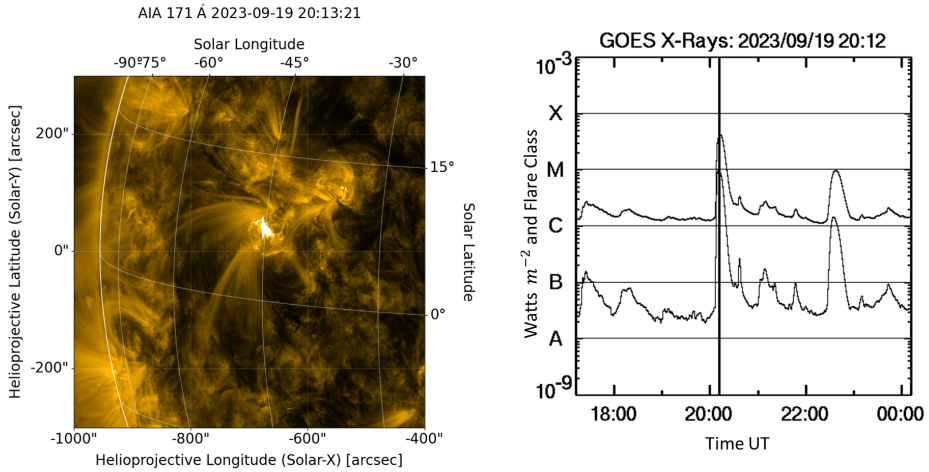

Figure 2.9: An M-class flare on September 19, 2023, at 20:13 UT was classified by GOES soft X-ray measurements based on its X-ray flux intensity. The flare is visible in the AIA coronal image at 171 Å, located at Longitude: -45°, Latitude: 10°. AIA image data were downloaded and generated using the Sunpy Python package (The SunPy Community et al., 2020), and the GOES X-ray plot was captured from the NASA (2023) website.

ate emissions in various wavelengths in different scenarios and through different mechanisms.

The main identification and classification of flares occur in the soft X-ray spectrum, determined by the X-ray flux measured by the Geostationary Operational Environmental Satellite (GOES) (see http://www.swpc.noaa.gov). Depending on the X-ray flux magnitude observed by GOES, in units of [$Watts\ m^{-2}$], letters B, C, M, and X are used to represent increasing orders of magnitude. For example, in Figure 2.9, on September 19, 2023, a flare was identified in the GOES measurement at 20:13 UT in the 'M' class, and the bright EUV emission of the flare is visible in the AIA image of the solar corona at 171 Å.

The most widely accepted and fundamental model of a solar flare is called the CSHKP model, which involves the concept of magnetic reconnection (the name is derived from the initials of the four authors who developed it: Carmichael, 1964; Sturrock, 1966; Hirayama, 1974; Kopp & Pneuman, 1976). The concept of the CSHKP model (also referred to as the standard model) can be briefly described using Figure 2.10:

- Magnetic flux ropes emerge from the photosphere from the turbulent convective zone (the region below the photosphere) via magnetic buoyancy.

- The emerged magnetic flux tube grows in the lower solar atmosphere (Photosphere and Chromosphere). The footpoints of these loops undergo shear motion relative to each other, and the loops can twist together. This results in a current sheet forming between a rising plasmoid and newly formed loop apex (see (c) in Figure 2.10).

- Magnetic reconnection (as introduced above) occurs along the current sheet.

- The accelerated particles in the downward outflow of the reconnection propagate towards the chromosphere, increasing the local plasma density and leading to non-thermal bremsstrahlung emission (see Chapter 3, and also see Brown, 1973), which produces hard X-ray (HXR) radiation at the footpoint (ribbons shown as yellow bars in (b), and pink dots imaged in the left panel image). During this step, chromospheric plasma is heated and ablated up into the corona along the flare loop, driven by the overpressure of the chromosphere, termed chromospheric evaporation/ablation (e.g., see: Fisher et al., 1985; Zhang & Ji, 2013). This is a critical process where plasma upflows into the coronal region and heats to over 10 MK, strongly emitting in X-rays.

- Accelerated energetic particles (electron beam) in the upward outflow by reconnection along open field lines that extend to the heliosphere, or large coronal loops extend to the middle and upper corona, generate Langmuir waves and produce electromagnetic waves at the local plasma frequency (or double of it) in radio ranges. This is the plasma emission mechanism, detailed in the next chapter and is the key mechanism to produce observed solar radio signals that are intensely studied in this thesis.

A solar flare is not only a significantly complex spatial but also a temporal phenomenon in the solar atmosphere, typically described in three phases: Pre-flare, Impulsive, and Decay phase. The Pre-flare phase describes the stage preceding the main impulsive explosion, characterised by magnetic flux rising and emerging from the solar surface and interacting with the existing magnetic loop structures. Thermal Bremsstrahlung emission drives the increase in EUV and soft X-ray radiation during this phase. The Decay phase is characterised by the slowly decaying emission observed in X-ray and EUV emissions, due to the plasma cooling by thermal

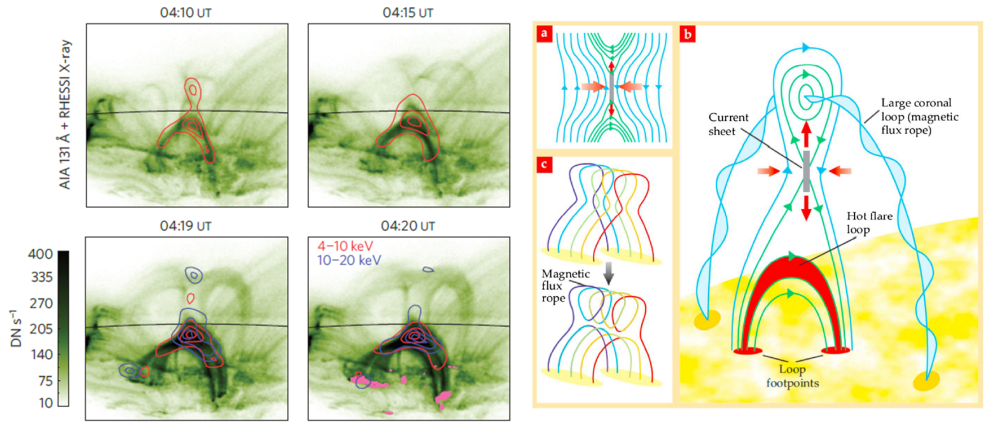

Figure 2.10: Left: This composite image from Su et al. (2013) showcases a flare that occurred on 17 August 2011 at 4:19 UT. It composites the SDO AIA 131 Å band (green image), flare regions on the solar surface as measured by the 1600 Å band (shown in pink on the surface), and red and blue contours from RHESSI X-ray images in the 4–10 keV and 10–20 keV energy bands, respectively. These images are comparable to the sketch on the right. Right: The sketches illustrate the standard model for magnetic eruption events that produce solar flares. (a) depicts the magnetic reconnection process; (b) shows the reconnection process resulting in a standard two-ribbon flare (ribbons are the two yellow bars at the footpoints of flare structures in (c)); (c) compares the flare region magnetic field states before and after reconnection, highlighting the outflow of flare plasma confined in the flux rope.

conduction followed by radiation (see Culhane et al., 1970).

Between the Pre-flare and the Decay phase, the Impulsive phase of a solar flare describes the period of the magnetic reconnection process and the acceleration of energetic particles to non-thermal velocities, travelling downwards and upwards from the current sheet region (the diffusion region of reconnections). The downward-travelling particles produce hard X-rays (HXR) at the flare footpoints via collisional non-thermal thick-target emission, and microwave emissions by gyrosynchrotron emission when electron beams are trapped in the magnetic fields of the flare arch. Consequently, impulsive HXR and microwave emission during a flare, both generated by non-thermal electrons travelling downwards, exhibit similar temporal profiles (see Neupert, 1968; White et al., 2011; Fletcher et al., 2011). The Impulsive phase also involves upward-streaming electron beams, which produce radio waves. There are typical temporal delays from the X-ray and microwave flux peak (White et al., 2011), as the distance between the radio emission region and the location of acceleration is longer than for X-rays and microwaves, due to source separations. This is because electron beams require a distance of propagation to be-

come unstable enough for Langmuir wave growth, known as the instability distance (e.g., see Reid et al., 2011; Reid & Kontar, 2013; Reid & Ratcliffe, 2014; Reid & Kontar, 2018a). Thus, the origin of the delay time between the microwave and the radio wave peak flux during an impulsive flare is the distance from the acceleration site to both wavelengths' emission regions. In Chapter 7, I utilised the nature of the delay time between the correlated peak fluxes of microwave and radio waves during an impulsive flare to investigate the coronal plasma density distribution model and electron beam velocities above this flare region.

Coronal Jet

Solar coronal jets are smaller-scale plasma ejections from the bottom of the solar atmosphere towards the outer layers, compared to solar flares. They generate radiation observable in X-rays at temperatures ranging from 10^4 to 10^7 K (such as, Shibata et al., 1992; Chifor et al., 2008), as well as in the EUV range (such as, Wang et al., 1998; Sterling et al., 2015; Chandra et al., 2015; Joshi et al., 2020), and are important sources of significant mass and energy input to the upper solar atmosphere (Raouafi et al., 2016). Including X-ray and EUV jets, the phenomenon of 'jets' encompasses many subclasses, such as EUV macrospicules (large and long-lived jets (see Loboda & Bogachev, 2019)) and $H\alpha$ macrospicules and surges (cool and dense ejections typically observed in chromospheric lines (see Nóbrega-Siverio et al., 2021)). Moore et al. (2010) highlighted that the main differences among the above-listed jets are their plasma temperatures, with 4×10^6 K for X-ray jets, $\sim 10^5$ K for EUV jets and macrospicules, and $\sim 10^4$ K for $H\alpha$ macrospicules and surges. Regardless of the subclass to which a jet belongs, the fundamental driver of the jet is magnetic reconnection that converts stored magnetic energy into kinetic energy, accelerating particles outwards into space. In this dimension, jets are similar to flares but have different topological evolution in the relaxation and reconstruction of the stressed magnetic fields. A standard jet model introduced by Shibata et al. (1992) described the magnetic reconnection occurring between small-scale emerging magnetic loops and the surrounding pre-existing coronal field that has negative polarities (see Figure 2.11). In Moore et al. (2010)'s work, about two-thirds of coronal X-ray jets are standard jets. Another type of jet, called blowout jets, also involves the reconnection process. As jet physics is not the focus of this thesis, only brief introductions are provided here, and interested readers are referred to the review paper by Raouafi et al. (2016) and the PhD thesis by Joshi (2021).

The processes of solar jets involve magnetic reconnections conducive to particle accelerations and subsequent transport upwards to the upper corona. Consequently, the jet-accelerated electron beams also generate radio bursts. The joint observations of type III bursts and soft X-ray (SXR) jets have been studied by various authors (e.g., Aurass et al., 1994; Kundu et al., 1995; Raulin et al., 1996). Correlations between type III bursts and EUV jets have also been observed, of-

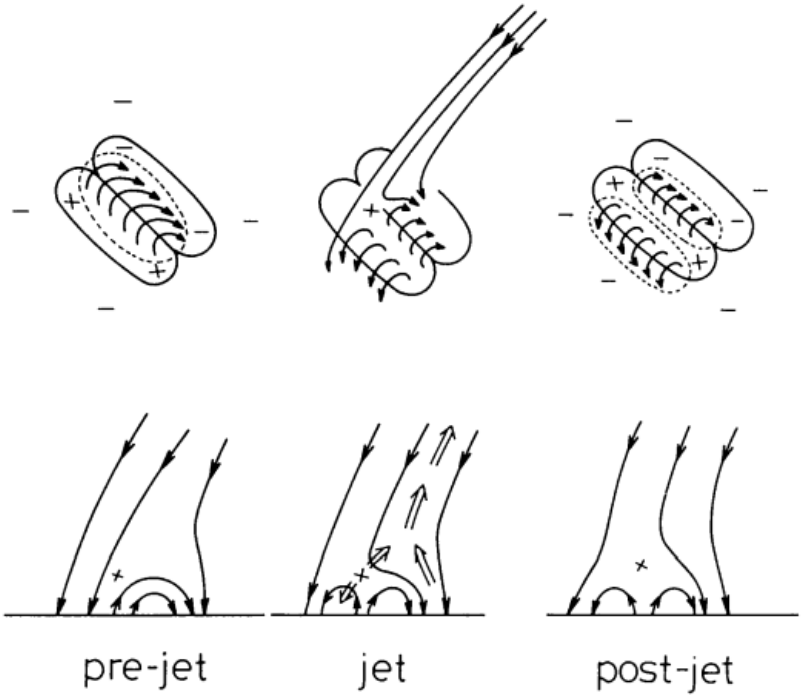

Figure 2.11: Sketches of the physical process of standard jet model. Pre-jet is where an emerging flux surrounding by pre-existing fields with negative polarity. The middle cartoons shows the reconnection reconstruct the magnetic fields and accelerate particles travelling outwards, and generate intense X-ray and EUV emissions identified as a jet. Post-jet illustrate the relaxed magnetic field tropology after the jet. These sketches taken from Shibata et al. (1992).

ten associated with solar energetic electron events (e.g., Innes et al., 2011; Klassen et al., 2011; Chen et al., 2013). Reid & Ratcliffe (2014) succinctly concludes the relationship between coronal jets and type III solar radio bursts in section 2.5.2. In this thesis, the type U bursts studied in Chapter 6 are correlated with coronal jets observed in the AIA 171 Å band.

Chapter 3

Radio Sun

Since the first identification of solar radio emissions in February 1942, during World War II, using a military-developed radar in Britain to monitor the national sky, it has been commonly believed that these emissions predominantly radiate from the higher layers of the solar atmosphere. Figure 3.1 displays the sun as observed from frequencies ranging from 25.8 GHz to 24.6 MHz. It is evident that lower frequency radio emissions below 240 MHz originate from the outer layer, in contrast to the microwave sun observed in GHz. This is because the frequency of low-frequency solar radio emissions is equal to or double the ambient plasma frequency, as they are generated via the plasma emission mechanism (introduced later in this chapter).

Although a number of mechanisms are relevant to solar radio emission in the corona, these include gyroresonance and gyrosynchrotron emissions (from thermal and non-thermal electrons gyrating in the magnetic field, respectively), as well as Bremsstrahlung emission (free-free, electron-ion interaction). The first two mechanisms, termed incoherent emissions (where 'incoherent' means the summation of radiation generated independently by many individual particles), occur predominantly in the lower corona. This region has a higher plasma density environment and consists of strong and small-scale magnetic fields. However, in the middle and outer corona, where the plasma is more tenuous and the distances electron beams travel are large enough for the initial beam velocity to become unstable for Langmuir wave growth, the mechanism producing solar radio emissions transitions predominantly to plasma emission mechanisms. This coherent emission means radiation is efficiently produced by a set of waves (in our case, three waves) that are coherent in phase, as illustrated in Figure 3.2.

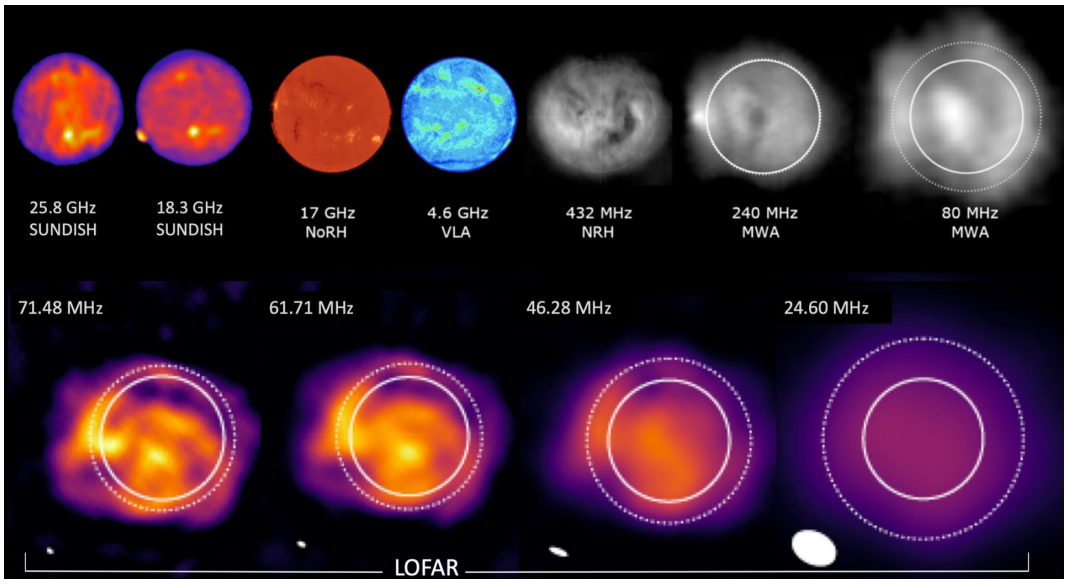

Figure 3.1: Images of the Sun at frequencies from 25.8 GHz to 24.6 MHz are presented. Progressing from the outer left to the lower right, the observations were captured by the Nobeyama Radioheliograph (NoRH), Very Large Array (VLA), Nançay Radioheliograph (NRH), Murchison Widefield Array (MWA), and Low-Frequency Array (LOFAR). The solid circles in the images on the right represent the size of the Sun as observed in visible light. This figure was published by Zhang et al. (2022).

3.1 Radio Emission Mechanisms

3.1.1 Incoherent Solar Radio Emission

There are two types of incoherent emission mechanisms that play a significant role in explaining solar radio emissions: Bremsstrahlung emission and Gyromagnetic emissions, the latter encompassing both gyroresonance and gyrosynchrotron processes.

Bremsstrahlung emission, also known as free-free emission, results from electrons being accelerated by the Coulomb force during interactions with ions within the range of the ion's Coulomb field. This process translates the electron's kinetic energy into radiation, embodying the principle that the acceleration of charged particles generates electromagnetic radiation (see Larmor, 1897). The term 'free-free' denotes the state of the electron, which remains free both before and after this interaction (Nindos, 2020).

Gyromagnetic emissions are generated by free electrons that change their velocity direction due to the presence of a magnetic field. The components of electron velocity perpendicular to the magnetic field are accelerated by the magnetic com-

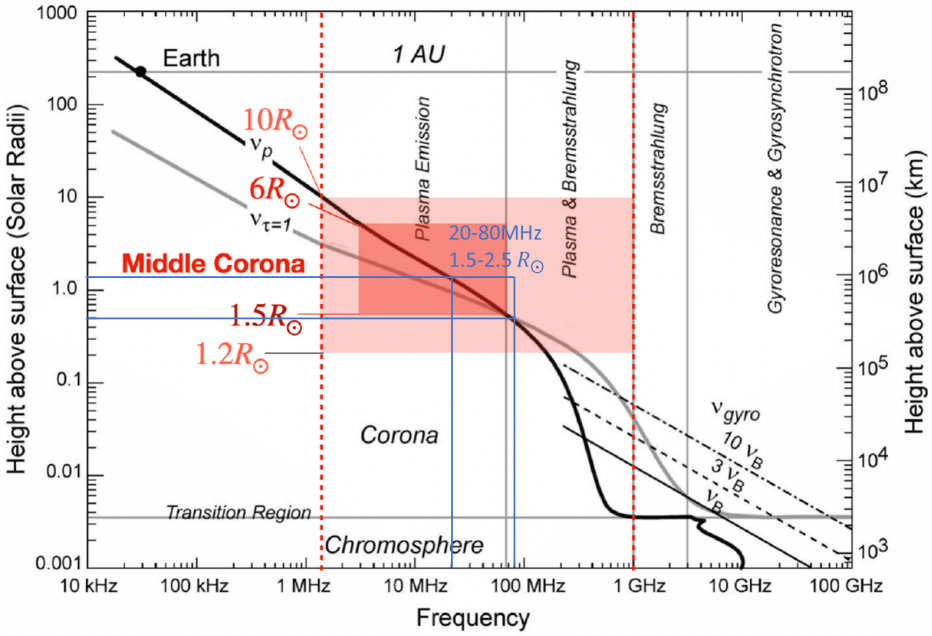

Figure 3.2: Radio frequencies are associated with specific altitudes in the solar atmosphere. The dark pink box defines the middle corona region, spanning from 1.5 to 6 $R_\odot$. The blue lines demarcate the 20 to 80 MHz region, characteristic of solar atmospheric frequencies approximately from 1.5 to 2.5 $R_\odot$, marking the boundary region between the inner and middle corona. The radio emissions are generated through plasma emission mechanisms by electron beam trajectories. (Adapted from Chen et al. (2023a), and originally sketched by Gary & Hurford (2004), who describes the sources for the temperature, density, and magnetic field values used in this plot.)

ponent of the Lorentz force. As detailed by many reviews on solar radio emission mechanisms, such as Melrose (1985a) and Nindos (2020), when the electron energy corresponds to quiet coronal temperatures (within the thermal speed range and at non-relativistic energies, approximately 10^6 K), the Gyromagnetic radiation power is distributed at the electron's gyrofrequency and its harmonics, known as gyroresonance emission. If the electron energy reaches mildly relativistic levels (ranging from a few tens of keV to a few MeV), the radiation power is distributed across a wide frequency range at harmonics of the gyrofrequency. This occurs for both thermal and non-thermal electron energy distributions, and this type of gyromagnetic emission is termed gyrosynchrotron emission. In conclusion, and as generally accepted regarding solar incoherent radio emissions, gyroresonance emission is the primary emission mechanism above sunspots with strong magnetic fields in the microwave range, while gyrosynchrotron emission is the predominant emission mechanism in solar flares that accelerates electrons to mildly relativistic energy levels.

3.1.2 Plasma Emission Mechanism

In the middle and outer corona, where the plasma becomes more tenuous and the electron beam travel distances are sufficiently large, the initial beam velocity may become unstable for Langmuir wave growth. Consequently, the mechanism producing solar radio emissions predominantly transitions from the incoherent emission mechanisms introduced earlier to the plasma emission mechanism, as illustrated in Figure 3.2. The low ambient plasma temperature and density in the middle and upper corona render incoherent emission inefficient. As a result, the brightness temperature of low-frequency bursts is too high to be explained by any incoherent mechanism.

The plasma emission mechanism is currently the most widely accepted process for generating low-frequency solar radio bursts in the MHz range and beyond, as depicted in Figure 3.2. This mechanism is especially recognized as the predominant model for type III burst generation. Such bursts, along with the low-frequency fast-drift bursts family (which includes type III, J, and U bursts, as detailed in Section 3.2), are the primary focus of this thesis.

The theory of the plasma emission mechanism was originally proposed by Ginzburg & Zhelezniakov (1958), who introduced the model for the generation of type III bursts. This model has been further developed by numerous studies (e.g., Sturrock, 1964; Smith, 1970; Melrose, 1980; Dulk, 1985a; Melrose, 1987). It considers the two-stream instability of an electron beam, which, when accelerated during magnetic energy release activities at low altitudes in the solar atmosphere and traveling along magnetic flux tubes in the solar corona, generates plasma waves (Langmuir waves). These waves then transform into observable radio emissions at plasma and double plasma frequencies through nonlinear plasma processes.

The theory of the plasma emission mechanism is depicted in Figure 3.3. This diagram delineates four steps in the theoretical framework describing two types of radio emissions produced by an accelerated electron beam:

1. **Acceleration of the Electron Beam:** Initiated by magnetic energy release in the solar atmosphere, predominantly through magnetic reconnection, this step converts the stored magnetic energy in solar atmospheric magnetic fields into kinetic energy for the electron beam.

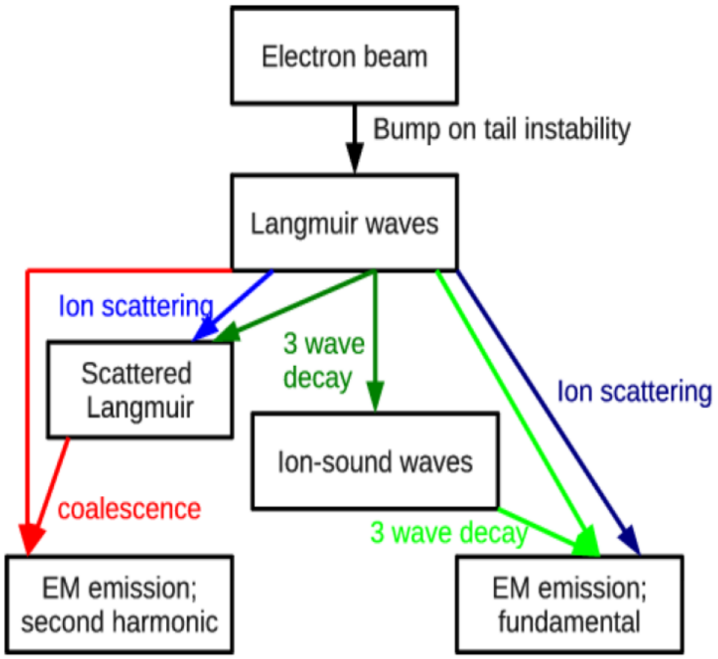

Figure 3.3: Flow diagram illustrating the plasma emission mechanism is credited to Reid & Ratcliffe (2014), adapted from Melrose (2009).

2. **Bump-on-Tail Instability:** As the electron beam propagates along magnetic flux tubes in the corona, faster electrons outpace slower ones, creating a differential velocity. This leads to a 'bump-on-tail' instability, fostering the growth of plasma Langmuir waves at the local ambient plasma frequency.

3. **The Fundamental (F) Emission ($f_F = f_p$):** This phase involves the conversion of Langmuir waves into electromagnetic waves at the same frequency, facilitated either by scattering off plasma ions or by decay processes involving ion-sound waves.

4. **The Second Harmonic (H) Emission ($f_H = 2f_p$):** The coalescence of two opposite Langmuir waves (the opposite direction Langmuir wave being a side product of the fundamental emission process) can generate second harmonic emissions. This results in electromagnetic waves at twice the frequency of the local background plasma frequency.

The acceleration process of the electron beam (Step 1) driven by magnetic reconnection, is detailed in Section 2.5. During solar flares, the accelerated electron beam can propagate upwards through 'open' magnetic field lines, initiating the

plasma emission mechanism process and generating radio flux in the low-frequency range from MHz to kHz. Alternatively, when the beam propagates downwards into the dense chromospheric plasma, these nonthermal electrons produce Hard X-ray (HXR) emissions through the bremsstrahlung process and microwave emissions via gyrosynchrotron emission (see White et al., 2011; Holman et al., 2011; Kontar et al., 2011). This step underscores the importance of comparing the temporal behaviour of flare radiation observed across different wavelengths, which is crucial for diagnosing the kinetic properties of the electron beam and the corresponding plasma and magnetic field conditions in the flare region. This topic forms the research focus of Chapter 7.

The second step in the plasma emission mechanism theory, the Bump-on-tail instability, leads to the presence of Langmuir turbulence, which is a pivotal step in the process. Langmuir waves, first identified by Tonks & Langmuir (1929) in their study of arc discharges, are longitudinal plasma electron waves. These waves are electron plasma oscillations modified by the thermal motions of the electrons. They exist only above the plasma frequency, denoted as $\omega/\kappa \geq v_e$ (where ω is the angular frequency, κ is the wavenumber, and ω/κ is the phase velocity), and are strongly damped through the collisionless Landau damping mechanism by thermal electrons, except for $\omega/\kappa \geq 3v_e$ (Melrose, 1985b).

The Bump-on-tail (or 'bump-in-tail') instability arises due to the instability of the stream of the accelerated electron beam, which exhibits a positive gradient in its velocity distribution function, as illustrated in Figure 3.4. The A-B region, where the gradient is positive, indicates that there are more electrons moving faster than the Langmuir wave phase velocity V_{ph} than there are slower ones (Sarkar et al., 2015). In this scenario, fast electrons outpace slower ones, exciting waves through energy exchange between the particles and waves for electrons with speed V_e close to V_{ph} (as observed in the A-B region of Figure 3.4). Slower electrons ($V_e < V_{ph}$) gain energy from the Langmuir wave, limiting wave growth, while faster electrons ($V_e > V_{ph}$) lose energy to the waves, facilitating the growth of these waves.

The energy exchange between particles and waves through the Bump-on-tail instability not only influences the growth of the waves but also alters the kinetic properties of the electrons. This process, known as 'quasi-linear relaxation', in-

creases the kinetic energy of slower electrons (which gain energy from the waves) while reducing that of the faster ones (which lose energy to the waves), thereby smoothing out the positive gradient and decelerating the energy transfer. Electron beam propagation in the solar corona undergoes the process of quasi-linear relaxation, as demonstrated by Kontar (2001a). This process showcases the electron distribution function $f(v,t)$ and the spectral energy density of Langmuir waves $W(v,t)$ at various times (see Figure 3.5), leading to the appearance of a plateau in velocity space with a zero gradient. The generation of Langmuir waves by an accelerated electron beam and the interaction between the beam and waves in the solar corona constitutes a complex area of study that has evolved over the years. While it is related to the work presented in this thesis, it does not constitute the primary focus. For detailed studies and discussions of the theory, refer to Grognard (1985); Kontar (2001b,a). In conclusion, the most significant outcome of the Bump-on-tail instability (Step 2) is the generation of Langmuir waves by the accelerated electron beam travelling in the corona. The frequency of Langmuir waves equals the local ambient plasma frequency. Through wave-wave interactions, introduced in the following part of this section, these Langmuir waves are converted into electromagnetic waves (the radio waves under study) at the same frequency (Step 3: F emission) or at double this frequency (Step 4: H emission).

The conversion of Langmuir waves into electromagnetic waves and other types of waves through wave-wave interaction processes is a crucial component of the plasma emission mechanism theory. The converted transverse electromagnetic waves, which are observable, radiate at either the local plasma frequency, as indicated in the 'EM emission: fundamental' block in Figure 3.3, or at twice the local plasma frequency, as shown in the 'EM emission: second harmonic' block. These correspond to steps 3 and 4, respectively, as mentioned at the beginning of this section. These physical processes are also not the focus of this thesis, and this part aims to give the reader a full but brief picture of the mechanism only. Detailed description can be found in Melrose (1980, 2009, 2017).

For the fundamental emission, two possible processes are analogous to those for Langmuir waves: scattering by plasma ions, and decay involving ion-sound waves. The ion scattering process, proposed in the original version of the plasma

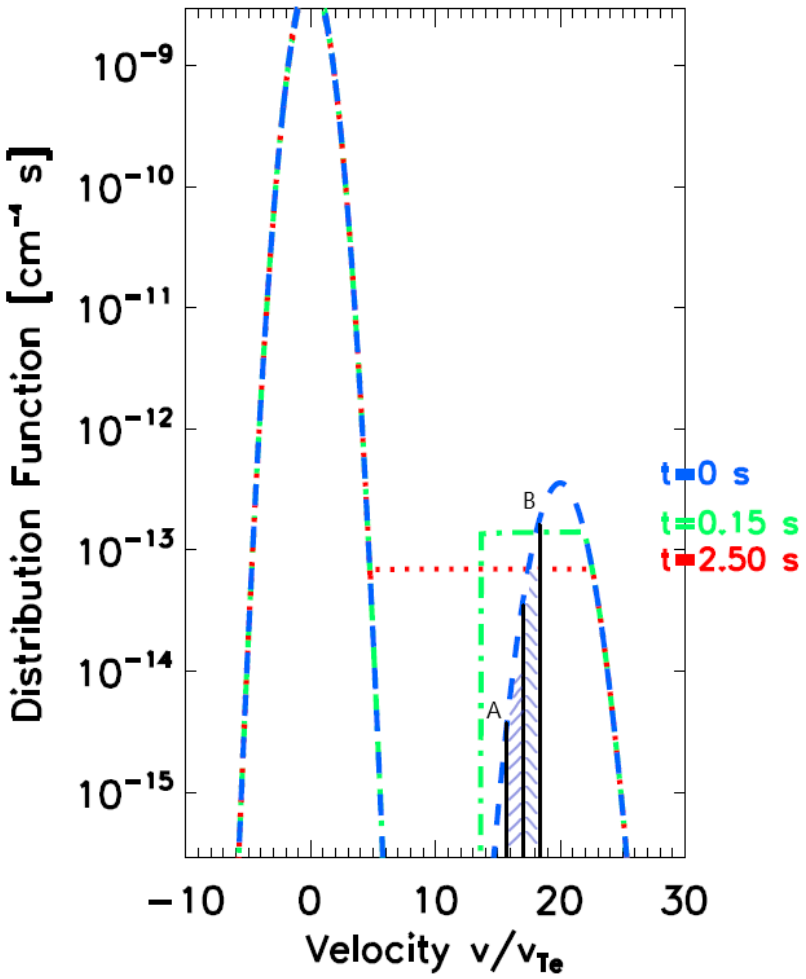

Figure 3.4: An example of a multiple-peaked electron velocity distribution function and its evaluation over time from $t = 0 to 2.5$ seconds is presented. When $t = 0$, the A-B region indicates where the gradient is positive, and the electron beam is unstable. This condition represents the 'bump-on-tail' instability, which is conducive to Langmuir wave growth. The electron distribution function relaxes to create a plateau in velocity space with a zero gradient ($t = 0.15, 0.25s$) after producing Langmuir waves. The figure is adapted from Reid (2011)'s PhD thesis.

emission mechanism by Ginzburg & Zhelezniakov (1958), involves the scattering of Langmuir waves into transverse waves off thermal ions. This scattering of Langmuir waves off thermal ions is attributed to the interaction with the Debye shielding cloud of electrons moving in conjunction with the ion. This process is similar to Thomson scattering, though it involves a cloud of electrons rather than a single electron. As a result, the ion scattering process can directly convert Langmuir waves, L, into transverse electromagnetic waves at the same frequency, T_F (see Melrose, 1985a;

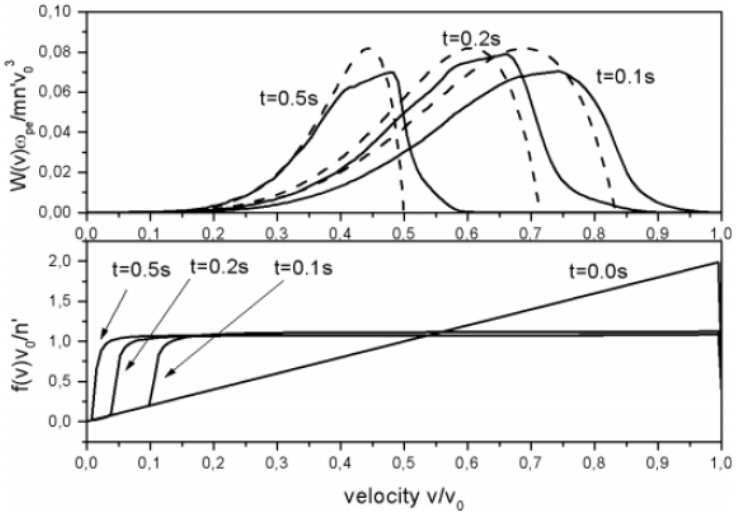

Figure 3.5: Electron distribution function $f(v,t)$ and spectral energy density of Langmuir waves $W(v,t)$ at various times, for the case where the plasma density decreases with distance. When $t = 0$, it correlate to the beginning stutus as similar as the A-B region in Figure 3.4 that $f(v,t)$ has the positive gradient. After quasi-linear relaxation, the smoothing out the positive gradient leads to the apperance of plateau (that $df/dv = 0$). Figure adapted from Kontar (2001a).

Reid & Ratcliffe, 2014). The ion scattering process can also produce ion-sound waves, S (proposed by, e.g., Lin et al., 1986), and an oppositely directed Langmuir wave, L', by the three-wave interaction (involves two waves beating to generate a third wave, see, e.g., Robinson et al., 1994; Reid & Ratcliffe, 2014; Melrose, 2009, 2017). This step can be described as:

- $L \rightarrow T_F$: Represented by the blue line linking 'Langmuir waves' to 'EM emission: fundamental' in the flowchart (Figure 3.3), this describes the scattering of Langmuir waves off thermal ions.

- $L + S \rightarrow T_F$ **and** $L \rightarrow T_F + S$: Shown by the bright green lines linking 'Langmuir waves' with 'Ion-sound waves' and 'EM emission: fundamental' in the flowchart, these represent the coalescence and decay of Langmuir waves with ion-sound waves.

- $L \rightarrow L' + S$: Illustrated by the dark green lines linking 'Langmuir waves' with 'Ion-sound waves' and 'Scattered Langmuir', as well as the left blue line on the left-hand side of the flowchart, this process is also generated by the decay of Langmuir waves.

The fundamental emission process, involving complex three-wave interactions, stands in contrast to the comparatively simpler second-harmonic emission process. In this process, back-scattered Langmuir waves, denoted as L', coalesce with the beam-generated waves to produce the second harmonic emission. This step can be described as: $L + L' \rightarrow T_H$, where T_H represents the transverse electromagnetic waves at double the frequency of the L and L' waves ($f_{T_H} = 2f_{T_F} = 2f_L$). This correlation is indicated by the red line in the flow chart. For further study and reviews of solar radio generation and plasma emission mechanisms, refer to Reid & Ratcliffe (2014); Melrose (2017).

Through the plasma emission mechanism described in this section, an electron beam traveling in the solar corona, especially in the middle corona regions, generates transverse electromagnetic waves at radio frequencies ranging from MHz down to kHz that equal or double the ambient plasma frequency. This allows the conversion of the observed radio flux frequencies into the ambient plasma density along the electron beam's travel path. According to the plasma frequency definition:

$$f_e = \sqrt{\frac{n_e e^2}{\pi m_e}} \tag{3.1}$$

where n_e is the ambient plasma density, m_e is the electron mass, e is the charge of an electron.

3.2 Solar Radio Bursts

Solar low-frequency radio fluxes can be observed by ground-based radio observatories, such as radio telescopes or interferometers, as well as by space-based low-frequency instruments operating in different frequency ranges. The observations are typically presented in the form of 'dynamic spectrum' data, which constitutes the fundamental form of solar radio data products. The dynamic spectrum, as illustrated in Figure 3.6, represents the radio flux observations in a two-dimensional format. The Y-axis of the spectrum denotes the frequency of the observed radio flux, while the X-axis indicates the time of observation. Consequently, the intensity shown on the spectrum corresponds to the flux of the radio waves, typically measured in units of [sfu] (Solar Flux Unit, $1\ sfu = 10^{-19}\ erg \cdot cm^{-2} \cdot Hz^{-1}$). This implies that each frequency channel on the dynamic spectrum captures the variation of flux

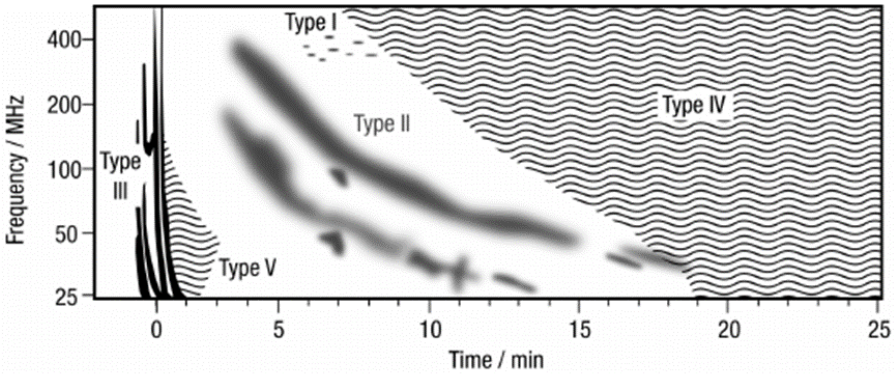

Figure 3.6: Solar radio bursts are classified from type I to V based on their morphology in the dynamic spectrum, as outlined by Ganse et al. (2012).

over time. On the dynamic spectrum, the observed radio fluxes often exhibit bright 'bursts' characterised by various shapes and structures in their frequency-time profiles. These variations are due to different emission mechanisms or specific electron beam trajectories. Consequently, these distinctive features are classified into different types of radio bursts. Typically, bursts are categorised into five standard types based on their morphological characteristics. There are numerous reviews (see Dulk, 1985a; Bastian et al., 1998; Nindos et al., 2008).

Type I, II, and III bursts were the earliest identified types of solar radio bursts (see Wild, 1950). Type I bursts consist of numerous short-duration bursts, each lasting from 0.1 to 3 seconds, with narrow frequency bandwidths of a few MHz. These bursts often appear in groups and are characterised by a broadband continuum, persisting for durations ranging from a few hours to several days (McLean, 1971; Karlický, 2017). A group of Type I bursts can be structured, forming what is known as a Type I burst chain (Elgaroy & Ugland, 1970). These chains drift towards lower frequency ranges and have been used to determine the magnetic fields in their sources, assuming the radial velocity of the sources is equal to the Alfvén velocity (based on the empirical model by Sarma (1994), and has been utilised by, e.g., Sodré et al. (2015)). The emission mechanism of Type I bursts remains somewhat unclear. McLean (1981) proposed a mechanism wherein these emissions are generated by electrons accelerated by interactions among coronal magnetic fields, particularly due to the emergence of new magnetic structures in the corona above active regions.

Type II bursts are characterised by a slow frequency drift, mean value at $0.08 - 0.11\ MHzs^{-1}$ during solar cycle 23 and 24 (see Kumari et al., 2023), from high to low frequencies. This drift is associated with the motion of shocks moving outward through the solar corona. It is generally accepted that these shocks are linked to Coronal Mass Ejections (CME/CMEs, large expulsions of plasma and magnetic field from the Sun's corona. For their shocks related science, see: Morosan et al., 2019b; Maguire et al., 2020). The radio waves are generated by electron beams accelerated at the shock (see type II radio bursts review by Gopalswamy, 2000). Consequently, the gradient of the frequency drift of the 'backbone' of type II burst (accompanied by rapidly drifting stripes of radio emission emanating from the "backbone" toward both high and low frequencies), over time can be indicative of the speed of the Type II burst's exciter electron beam, and thus, the velocity of the CME front shocks.

Before delving into Type III bursts, this section provides a brief overview of Type IV and V bursts, as these types are not directly related to the work presented in this thesis. Type IV bursts are characterised by broad-band continuum emission and are divided into two main sub-types: 'moving' and 'stationary' IV bursts (see Fokker, 1963; McLean, 1985). Moving IV bursts are identified by their frequency drift from high to low frequencies, whereas stationary IV bursts do not exhibit this characteristic. Moving IV bursts are now recognised in association with CMEs and can serve as a useful diagnostic tool for determining CME magnetic field strength (see, e.g., Carley et al., 2017). On the other hand, stationary IV bursts typically show no apparent source motions and are more frequently observed (Dulk, 1985b). While the physical process of IV burst formation is not yet fully understood, one hypothesis suggests that stationary IV bursts most likely originate from gyro-synchrotron electrons trapped inside post-eruption flare loops, which remain stationary following CME expansion (see, e.g., Morosan et al., 2019a).

Type V bursts are characterised by their long duration, typically lasting a few minutes, and often appear on the dynamic spectrum as diffuse continua following Type III bursts. This often makes them difficult to identify, as they can be mistakenly considered as a part of the preceding Type III burst (White, 2007). A notable feature of Type V bursts is their polarisation, which often contrasts with that of the

preceding Type III burst. While Type V bursts are not the main focus of this thesis, more detailed information can be found in Suzuki & Dulk (1985), which provides a comprehensive summary of the main characteristics of Type V bursts.

Type III bursts, along with their sub-fractions, Type J and U bursts, are recognised as 'fast-drift' bursts due to their rapid frequency drift observed on the dynamic spectrum. These bursts were among the first to be identified, with Type III being one of the three types reported by Wild (1950) (the type III burst named by Wild et al., however, such bursts were identified even earlier by Payne-Scott et al., 1947; Payne-Scott, 1949), and Type J and U bursts first identified by Maxwell & Swarup (1958). Type III, J, and U bursts are invaluable as diagnostic tools for investigating flare-accelerated electron beams, as well as for understanding the associated coronal plasma conditions and magnetic field properties along the electron beam trajectory path. The subsequent Section 3.2.1 offers a detailed introduction to this family of fast-drift bursts (For a comprehensive review on Type III bursts, including discussions of J and U bursts, I recommend reading Reid & Ratcliffe, 2014). Utilising observations of Type III, J, and U bursts in the low-frequency range (10-90 MHz) for exploring the physical properties and processes of the solar middle corona, as mentioned at the beginning of this chapter, is the primary focus of this thesis.

3.2.1 Fast-drift Bursts: Type III, J and U bursts

Type III, J, and U bursts are categorised within the same family of solar radio bursts, known as fast-drift bursts, due to their similar characteristics on the dynamic spectrum and the analogous emission process (Suzuki & Dulk, 1985). Fast-drift bursts are classified based on their rapid frequency drift rate (df/dt) on the dynamic spectrum. These bursts are commonly believed to be generated by accelerated electron beams travelling along magnetic fields ('open' or closed fields) in the solar corona. Specifically, the exciters of Type III bursts travel at speeds approximately between 0.1 to 0.5 times the speed of light (c) (for example, see Alvarez & Haddock (1973); Aschwanden et al. (1995); Meléndez et al. (1999); Klassen et al. (2003), and my paper Zhang et al. (2023) that is presented in Chapter 5). The frequency drift rate, df/dt, can be used to determine the speed of electron beams, and will be introduced later and discussed throughout the works presented in this thesis.

Type III bursts are produced when the accelerated high-speed electron beam

generates Langmuir waves at the same frequency as the local ambient plasma. These waves are then converted into radio waves through either fundamental or second-harmonic emissions (the plasma emission mechanism, see Section 3.1.2). The electron beam generating Type III bursts travels along open field lines extending radially from low to high altitudes in the corona. As introduced in Section 2.3, an increase in altitude within the solar corona leads to a decrease in background plasma density. This decrease results in a characteristic frequency drift from high to low frequencies on the dynamic spectrum. The change in plasma density with altitude is a critical factor in solar radio physics. Consequently, the high speed of the electron beams, as they traverse regions with decreasing plasma density, is reflected by the high df/dt observed on the dynamic spectrum. An example of a Type III burst is shown in Figure 3.7 in a dynamic spectrum that combines multiple frequency ranges.

Type J and U bursts are generated through the same process as Type III bursts, but with a crucial difference in the trajectory of the electron beams. In these cases, the beams travel along large-sized coronal loops. The curved geometry at the top part of these loops forces the electron beam to transition from a mostly radial to a horizontal trajectory. As the electron beam propagates, the gradient of the background plasma density decreases because the radial travel distance reduces, reaching zero at the loop apex, and then the gradient gains a positive sign by travelling along the down-flow leg of the loop. This change in plasma density gradient is manifested on the dynamic spectrum as a 'negative-zero-positive' frequency drift rate, creating the distinctive 'J' or 'U' shapes. Inverted 'J' and 'U' shapes may also appear, depending on the orientation of the frequency-axis. The primary distinction between J and U bursts is the observability of the descending component, characterised by a positive frequency drift rate. This descending component is produced as the electron beam travels downwards along the down-flow leg of the coronal loop, encountering an increasing ambient plasma density gradient along its path. An example of a Type U burst is illustrated in Figure 6.1. This particular burst is the subject of study in the work presented in Chapter 6.

This thesis uses low-frequency 'fast-drift bursts' as powerful diagnostics of the solar middle corona plasma and magnetic field properties, as well as to study the

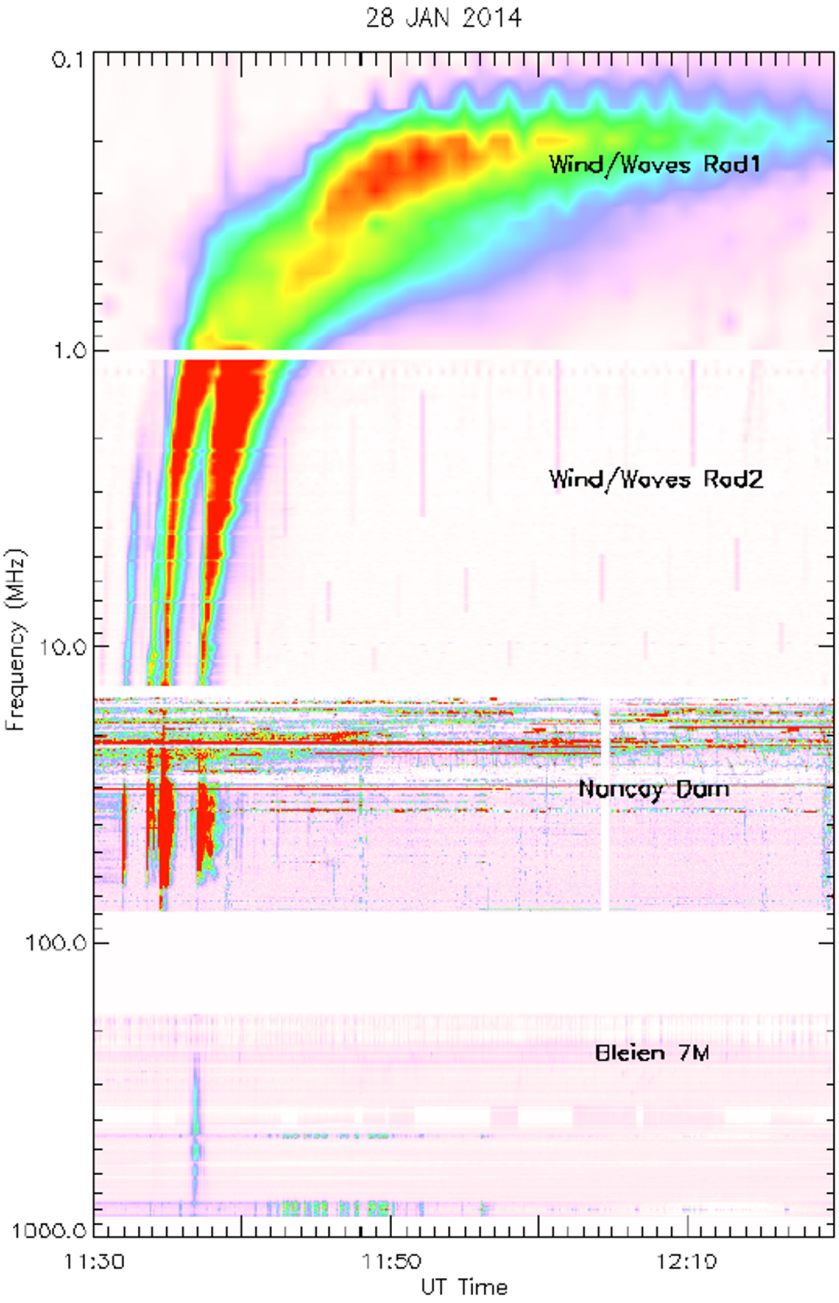

Figure 3.7: An example of an interplanetary Type III radio burst on a dynamic spectrum, observed by multiple observatories across different frequency ranges, is as follows: Frequencies from 900 to 200 MHz were observed by the Bleien telescope (Benz et al., 2009a), frequencies between 80 and 15 MHz by the Nançay Decametre Array (NDA) (Lecacheux, 2000), and the range from 14 to 0.1 MHz by space-based observations from the WAVES experiment onboard the WIND spacecraft (Bougeret et al., 1995). This combined dynamic spectrum credit: Reid & Ratcliffe (2014).

trajectories of accelerated electron beams in this region. The core focus of the study presented in this thesis, using type III, J, and U bursts, has been illustrated at the end of Section 2.1.4. However, type III, J, and U bursts have specific roles in studying

these topics. Type III bursts, and the high-frequency part of the J and U bursts (where the flux shows a relatively constant frequency drift rate before decreasing), are used to determine the coronal plasma density model and beam velocities, as the background corona electron plasma density distribution along the open magnetic fields can be described by well-studied numerical models, such as many introduced in Section 2.3. On the other hand, type J and U bursts are powerful for studying the plasma density distributions and electron beam trajectories along the top part of closed coronal magnetic loops, where the magnetic fields are horizontally bent and then point toward the sun. This part of very large loops that reach the middle corona can only be accessed and studied by low-frequency J and U bursts, rather than type III bursts observed in the same frequency range. Therefore, the loop-top plasma parameter distributions are estimated using J and U bursts, and the downward leg of the large coronal loop is studied using the U burst's descending leg component in this thesis. Methodologies are detailed in the science chapters of this thesis.

The following summary outlines some general characteristics of Type III, J, and U bursts across several topics. Understanding these characteristics is crucial before delving into detailed discussions in the science chapters of this thesis:

Frequency and time

Type III bursts typically originate at frequencies ranging from tens to hundreds of MHz and can even start at lower frequencies, including hundreds of MHz or beyond. During large solar flares, Type III bursts can commence at very high frequencies, such as in the GHz range (see, for example, Benz et al., 1983; Staehli & Benz, 1987; Meléndez et al., 1999). The stopping frequency of Type III bursts varies, with some bursts ending above 100 MHz and others extending down to around tens of kHz, near the plasma frequency near Earth. Bursts below 1 MHz are classified as 'Interplanetary Type III bursts' (IP Type III bursts) and can be observed by space-based radio instruments.

There are several models proposed to explain the stopping frequency of Type III bursts. One possibility is that the electron beam propagates along closed loops and stops emitting as it does not reach regions of lower plasma frequency. The plasma density gradient along the loop becoming small could also lead to an increased quasilinear time (characteristic time for wave-particle interaction), reducing

the rate of Langmuir wave growth (see Reid & Kontar, 2017). Additionally, Reid & Kontar (2015) investigated the role of the radial expansion of the guiding magnetic flux tube in affecting the stopping frequencies of Type III bursts. This expansion decreases the electron beam density, rendering it too stable for further Langmuir wave growth.

The burst duration of Type III bursts is widely accepted to vary inversely with frequency, a notable characteristic of their light curve, with rise times typically being shorter than decay times. Historically, the decay time of these bursts has been characterized as exponential across a broad range of intensities (Elgaroy & Lyngstad, 1972; Evans et al., 1973). The analysis work of Reid & Kontar (2018a) has provided new insights into these time characteristics. The rise, peak, and decay time profile can be used to determine the front, middle, and back of the electron beam speed. They suggest that the time profile of Type III bursts is more accurately represented by an asymmetric Gaussian profile rather than an exponential one, especially at higher frequencies. Moreover, it has been observed that the duration of Type III bursts, including both the rise and decay times, increases as a function of decreasing frequency. Reid & Kontar (2017) applied a similar method to determine the motion of the front, peak, and back of the electron beam generating U bursts. This, along with other studies, underscores that the frequency-time evolution is a crucial tool for studying the dynamics of electron beams generating fast-drift bursts, and a characteristic parameter to describe the frequency-time profile is the frequency drift rate of a burst, df/dt, in units of [Hz or MHz $\cdot$ s^{-1}].

Frequency drift rate and electron beam velocity

The drift rate of a Type III burst, an important parameter, is approximately 100 MHz/s in the metre radio wave range (see Suzuki & Dulk, 1985). This rate is typically measured in observational studies of radio bursts through various methods. One approach involves using the rise time profile of bursts to define the frequency drift rate. For instance, Alvarez & Haddock (1973) studied Type III bursts between 3 MHz and 50 kHz, combining data from eighty bursts up to a higher range at 550 MHz. They reported that the frequency drift rate follows the power law $df/dt = -0.01 f^{1.84}$ over four orders of magnitude range of frequencies, where f is in MHz and t in seconds. Alvarez & Haddock (1973)'s study represents a signif-

icant survey of Type III burst frequency drift rates. Since then, numerous studies have found the drift rate to be slightly lower than this prediction (for example, a comparison between several notable drift rate estimations, by Alvarez & Haddock (1973); Mann et al. (1999); Melnik et al. (2011), can be found in Zhang et al., 2018). Zhang et al. (2018) developed an automatic event recognition-analysis system using advanced computer vision methods, providing a statistical survey of the frequency dependence of the drift rate $df/dt = -0.0672f^{1.23}$ through a least-squares fitting of half a solar cycle of solar radio burst observations in the 10 to 80 MHz range.

The frequency drift rate of a fast drift burst can be used to estimate electron beam velocity along the radial axis, by assuming a numerical coronal plasma density model. This has been a classical methods applied by many previous studies (so many studies, almost every studies of type III, J, U bursts that using dynamic spectrum data, e.g. Dulk et al., 1987; Poquerusse, 1994; Klassen et al., 2003; Aschwanden et al., 1995; Meléndez et al., 1999; Reid & Ratcliffe, 2014; Reid & Kontar, 2017; Zhang et al., 2023; Dabrowski et al., 2023). Assuming a coronal density model, $N_e(r)$ (as introduced in Section 2.3), the frequency as a function of radial distances in the corona, $f(r)$, can be determined from the definition of the plasma frequency, given by $f = 8.98 \times 10^3 n_e^{1/2}$. Consequently, the frequency drift rate df/dt can be converted to dr/dt, representing the speed of the exciting electron beam. This method will be detailed in the science chapters of this thesis. Determining electron beam velocities is a key step involved in the three research projects that form the core of this thesis. Chapter 5 and 6 of this thesis present several methods for determining the velocities of electron beams that generate Type III, J, and U bursts. These methods include using peak flux time profiles of bursts on the dynamic spectrum, a novel strategy involving the high-frequency components of Type J and U bursts, and the application of solar radio imaging to directly estimate beam speeds.

F and H structures, and circular polarisation

When an excited beam of electrons propagates in the corona and radiates radio waves through the plasma emission mechanism, as introduced earlier in this chapter, both fundamental (F) and second-harmonic (H) emissions can be generated and observed. From radio bursts (commonly fast-drift bursts, and also type II bursts) ob-

served below 100 MHz, both fundamental and harmonic emissions are frequently seen, as documented in various studies (e.g., Wild et al., 1954; Stewart, 1974; Dulk & Suzuki, 1980; Suzuki & Dulk, 1985; Robinson et al., 1994). In such instances, the phenomenon is referred to as the Fundamental-Harmonic (F-H) pair of a Type III burst, which can also apply to Type J and U bursts. If an F-H pair is present, the fundamental component always starts at lower frequencies compared to the harmonic. This is because both the fundamental (F) and second-harmonic (H) components are generated by the same electron beam at the same location and under identical background plasma conditions. Consequently, the frequency of the harmonic emission is higher, being double that of the background plasma frequency and the F component waves. Therefore, the appearance of F-H pairs in fast-drift bursts serves as a robust strategy for classifying the fundamental and second-harmonic flux of the selected burst.

In cases where no apparent F-H pair is generated and observed, the classification of the radio flux as either F or H emissions can be determined through polarization measurements. F and H components exhibit different degrees of circular polarization, with F emissions generally being more polarized than H emissions, as shown in various studies (McLean, 1971; Suzuki & Sheridan, 1978; Dulk & Suzuki, 1980; Suzuki & Dulk, 1985). Specifically, Dulk & Suzuki (1980) conducted an analysis of 714 F-H pairs, which revealed that, on average, the H component had a circular polarization degree of 0.12, while the F component exhibited a higher polarization degree of 0.35. Consequently, the degree of circular polarization emerges as a crucial parameter in radio burst measurements, providing a strategy to accurately classify a burst as either fundamental or harmonic emission.

Source size

The size of fast-drift bursts increases with decreasing frequency. For Type III bursts, measurements across various frequencies show average sizes of 2 arcminutes at 432 MHz and 4.5 arcminutes at 150 MHz (Full Width Half Maximum, FWHM), as determined by Saint-Hilaire et al. (2013). At lower frequencies, the sizes further increase to 11 arcminutes at 80 MHz and 20 arcminutes at 43 MHz (Dulk & Suzuki, 1980), 5 degrees at 1 MHz, and 50 degrees at 100 kHz (Steinberg et al., 1985). At the extremely low frequency of 20 kHz, the size reaches approximately 1 Astro-

nomical Unit (AU) (Lin et al., 1973). A comprehensive summary of these measurements and observations of source sizes can be found in Reid & Ratcliffe (2014). Figure 3.8 illustrates a combination of many previous studies, displaying a linear fit in log-space between the source size in length, denoted as σ_{size} in [degrees], with frequency f in [MHz]. The FWHM depends on the observing frequency quantified as: $\sigma_{size} = (11.78 \pm 0.06) f^{-0.98 \pm 0.05}$, summarized by Kontar et al. (2019).

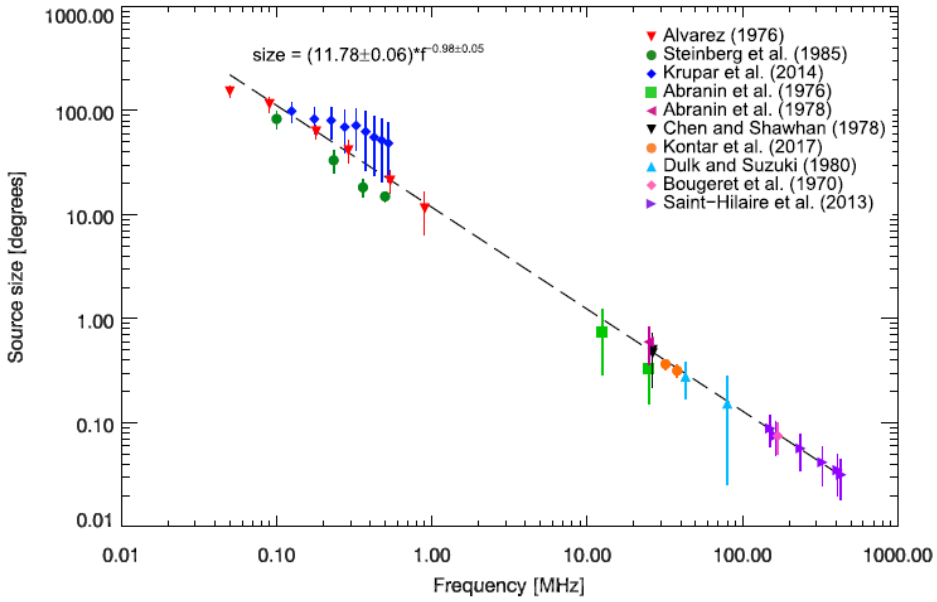

Figure 3.8: Over last 50 years of type III bursts measurements ranging from 0.05 to 500 MHz by several authors (). Source sizes (FWHM, in [degrees]) of type III solar radio observations vs. frequency (f, in [MHz]). A combination of observations is plotted as indicated by the legend, and a weighted linear fit was applied to the data in log-space. This plot credit: Kontar et al. (2019).

For Type J and U bursts, a similar trend is observed, with lower frequency radio sources appearing larger than those at higher frequencies within the same burst. For instance, Suzuki (1978) used the Culgoora radioheliograph to produce radio images of a Type U burst at frequencies of 43, 80, and 160 MHz. These images revealed that the half-intensity contour of the 43 MHz source is larger than that of the 80 and 160 MHz sources, regardless of whether it is on the ascending or descending leg of the burst.

The coronal plasma turbulence between the radio sources and the observer scatters the radio wave, introducing the scattering effect. This effect causes deviations in the observed radio burst images from the actual emission source, compli-

cating radio image interpretation. As extensively studied and discussed by Kontar et al. (2019, 2023), one of the most significant impacts of this scattering is the apparent increase in radio source size in radio images from to the actual size of the source (See Figure 3.9).

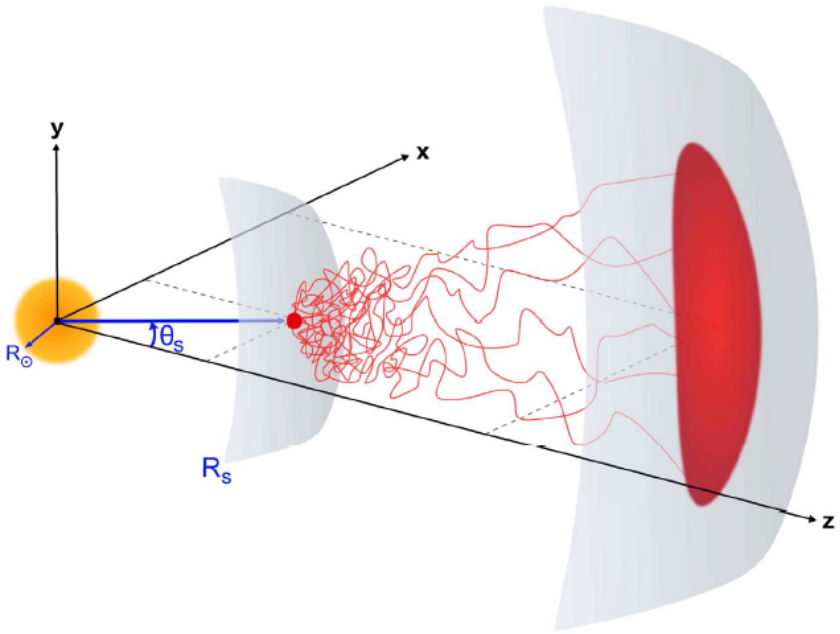

Figure 3.9: Cartoon showing the Sun-centered Cartesian coordinate system (x, y, z), where the z-axis is directed toward the observer. Photons from a point source of radio emission at R_s on radial coordinate and polar angle θ_s are scattered by cross a sphere at a distance large enough that scattering is no longer important, resulting in an apparent source size and position indicated by the red region. This cartoon credit: Kontar et al. (2019).

The scattering effect is an indispensable consideration when studying radio bursts using solar radio imaging measurements, a key technique presented in the Chapter 6. In addition to increasing the size of radio sources on images, the scattering effect also shifts the source position outward from the Sun's center and increases the source's major-minor axis ratio (changes the source shape) based on the observational angle, particularly as the actual radio source approaches the solar limb plane (again, for an in-depth study of the scattering effect, see Kontar et al., 2019, 2023). The impact of the scattering effect is thoroughly discussed in Chapter 6. While the study of solar radio wave scattering is not the primary focus of this thesis, it remains a potential direction for further research, as introduced in Chapter 8.

Chapter 4

Instrumentation: Ground-based Interferometry and Space-based Instruments

4.1 Radio Interferometry

Radio telescopes are crucial instruments in the exploration of the radio universe, including the study of the radio Sun. They operate primarily in two modes. The first mode is akin to the operation of optical telescopes, with the radio telescope functioning independently using a single radio signal receiver, typically a dish-antenna receiver. In this mode, the radio telescope captures signals from outer space, analogous to how an optical telescope captures light. This process involves placing a detector at the focal point of the radio telescope, allowing for the direct reception and analysis of radio waves from space. The performance of this stand-alone mode radio telescope is how good is the angular resolution, refer to the ability to observed fine structure of the radio source within small angular distances on the sky plane when perform imaging (mirroring the concept of the pixel resolution of the camera when taking photo). The angular resolution of the single disk antenna radio telescope can be describe by the Rayleigh criterion stated in the equation:

$$\theta \approx 1.22\frac{\lambda}{D} \tag{4.1}$$

where θ is the angular resolution (in [radians]), λ is the wavelength of electromagnetic waves, and D is the diameter of the instrument's aperture.

Achieving better angular resolution for low-frequency radio signals necessitates a larger aperture size. However, in practical scenarios, constructing such large apertures presents significant engineering and cost challenges. A prime example of the current limits in aperture size is the Five hundred meter Aperture Spherical radio Telescope (FAST, Nan et al., 2011), constructed by China, which stands as a testament to the maximum feasible size of filled-aperture radio telescopes. The requirement for even better resolution in radio measurements and imaging leads to the necessity of the second mode of radio telescope operation. This mode, calls radio interferometer, build by two or more smaller receiver placed apart from each other with a fixed distance (form an array of receivers, calls interferometric arrays), achieve the require angular resolution by as large as needed baseline distance. The angular resolution of an two element interferometer is:

$$\theta \sim \frac{\lambda}{B} \tag{4.2}$$

Where B is the baseline, refers to the distance between the two receivers. The interferometer effectively simulates a much larger telescope, provides a solution to the constraints faced in the first mode associated with aperture size.

In radio interferometry, two or more radio telescopes are linked and synchronized to observe the same region of the sky simultaneously. A prime example of this technique in action include the LOw-Frequency-ARray (LOFAR) — the main instrument utilized in this thesis. By connecting multiple receivers, a radio interferometer can process and integrate the signals received from each pair of antennas in an interferometric array. This coordinated combination of measurements from different locations enables the creation of extremely high-resolution images of astronomical radio objects. The underlying principle of this technique is that by integrating data from numerous antenna pairs.

In the work presented in this thesis, especially in the second science chapter (Chapter 6), we utilized LOFAR solar radio imaging data and its corresponding pipeline and software to conduct all necessary data processing for generating images from imaging data of radio sources associated with the selected bursts. This section designed to provide a brief overview of the background theory of radio interferometric imaging technique. While radio interferometry is a vast field of study

and not the primary focus of this thesis, it serves as an essential tool and instrumentation technique for our research. For a more detailed summary and comprehensive review of the principles of radio interferometry, I highly recommend the book by Thompson et al. (2017). This book provides an excellent overview of the subject. Additionally, as suggested by Thompson, it is advisable to first study the basic principles of Fourier Transform, which are fundamental to understanding radio interferometry, by reading Bracewell (2000). This sequential approach to the material will provide a solid foundation in the key concepts underlying radio interferometric techniques. The introduction of the interferometer and interferometric imaging in this chapter also credits the Physics 728: Radio Astronomy course online handout by Gary (2019), organised by the New Jersey Institute of Technology.

4.1.1 Interferometer and Interferometric Imaging

Basic unit of an interferometer array

The simplest configuration of an interferometer array is a single baseline between two antennas. The following part of this section introduces the fundamental principles of how this basic unit of an interferometer array responds to plane waves, which is the fundamental of the interferometric imaging technique. This includes introductions to the Fourier Transform relation between the 'complex visibility' and the 'sky brightness distribution'.

When a plane wave incident from directly overhead arrives at the antennas, it will be in phase (see Figure 4.1, left sketch). If the signal travels the same distance through cables to the correlator (indicated with an $\otimes$ in the figure, representing a multiplication), the signal from the two antennas will produce a maximum signal response. However, when a plane wave comes from a different direction, at an angle θ, as shown by the middle sketch in Figure 4.1, the wave will reach the 'Ant 1' antenna later than 'Ant 2', resulting in the signal being slightly out of phase. This discrepancy leads to a response less than maximum, as the out-of-phase signals are multiplied together. Nevertheless, this sketch illustrates an exceptional scenario where the waves arrive at 'Ant 1' exactly in phase with the signal received earlier by 'Ant 2', yielding a maximum response again. The angle of the secondary maximum responds can be described by:

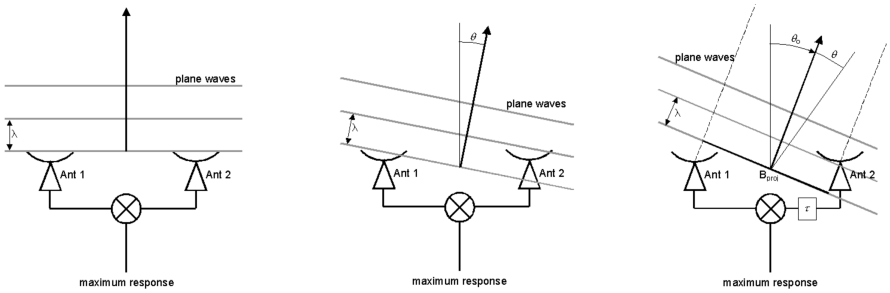

Figure 4.1: Cartoon sketch of a two-element interferometer responds to a plane wave. Left: plane waves incident from directly overhead of the unit (multiplication, and produce maximum responds). Middle: plane wave comes from a slightly different direction with angle θ from the vertical (out of phase, less response). Right: A delay τ inserted in one antenna to steer the phase center to a direction θ_0. Credits by Gary (2019)

$$\theta = sin^{-1}\frac{\lambda}{B} \tag{4.3}$$

In this context, 'B' represents the distance between the two antennas of this basic unit, and the angle θ denotes the angular separation of interference fringes in the sky plane, also referred to as the fringe spacing. To be more specific, when a two-element interferometer observes the sky plane, the maximum response occurs at angles of θ multiplied by an integer. This results in a fringe pattern across the sky, as illustrated in Figure 4.2.

The observation in the real case will be done over multiple bandwidth Δv (in frequency, [MHz]). As the fringes depends on the wavelength λ as shown in Figure 4.1, and the value of fringe spacing, θ, will be an path length equal to the wavelength. This results that at a different band will have a different spacing, describe by:

$$\theta = sin^{-1}\frac{c}{B\Delta v} \tag{4.4}$$

Here, c represents the speed of light. In this scenario, destructive interference across the band poses a problem because, at large angles, frequencies begin to interfere with each other. This implies that only the highest frequency bands, which have the smallest fringe spacing, can be effectively used for observation. This approach results in a narrow field of view, as depicted by the angle θ in the middle sketch of Figure 4.1. This angle represents the only maximum usable for observation without multi-band interference (where the integer equals 1 when multiplied by the fringe

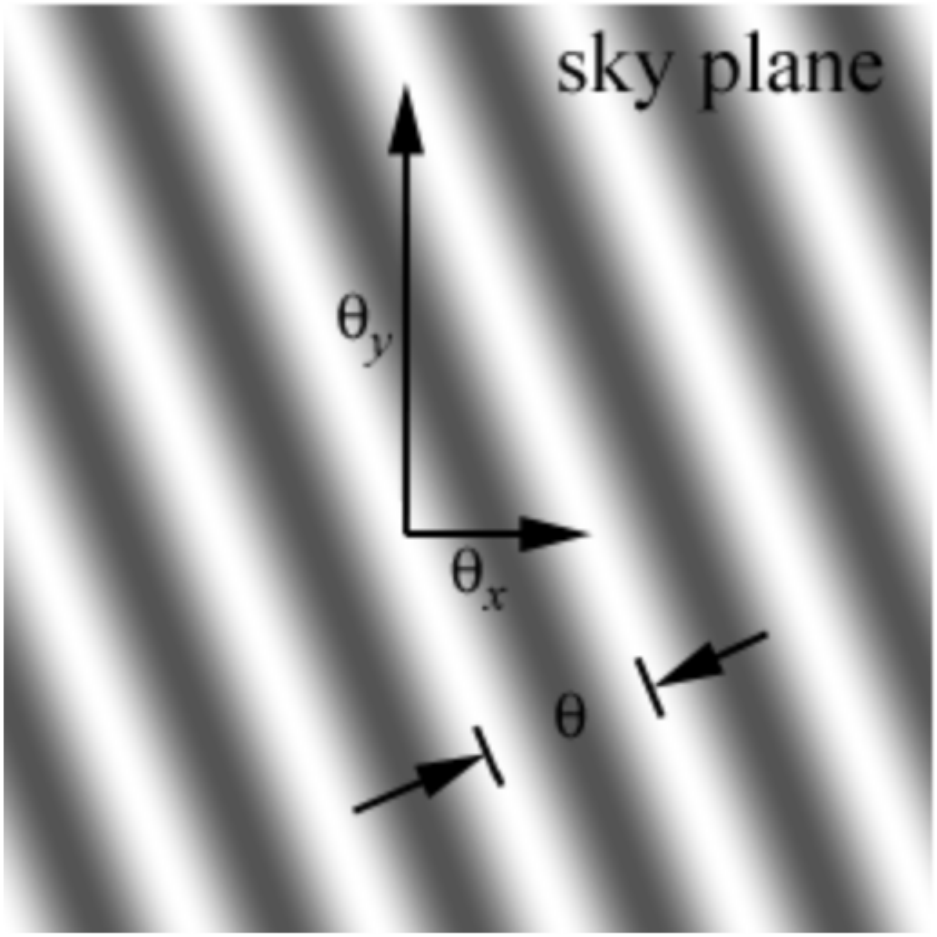

Figure 4.2: Fringe patterns in the sky plane, with angular separation θ is the fringe spacing. Credits by Gary (2019)

spacing of the highest frequency band). To address this limitation, the two-element interferometer can introduce a delay, τ, into the signal path of one of the antennas. This adjustment allows for 'steering' the phase center, as demonstrated in the right sketch of Figure 4.1. The additional τ inserted into 'Ant 2' alters the phase of the signal, forming a new phase center directed towards θ_0 (called the 'tracking delay'). This adjustment enables the observation of fringe spacing on the sky plane relative to this new phase center direction. Consequently, the B in Equation 4.3 becomes B_{proj} in the left sketch, indicating a shift from direct overhead observation.

Basic unit of interferometer response to sources

Based on the theory of how one basic unit responds to a plane wave, we define the maximum response at the phase center as the *cosine* component of the signal (notation: x). When a phase shift of $\pi/2$ is applied to the signal from one of the

antennas, we measure a new signal called the *sine* component (notation: y). Mathematically, the amplitude of the wavefront is expressed as:

$$a = (x^2 + y^2)^{1/2} \tag{4.5}$$

and the phase of the wavefront is:

$$\varphi = \tan^{-1}(y/x) \tag{4.6}$$

The above definitions are essential in explaining how the interferometer responds to sources in the sky. This is easier to illustrate with an example, as demonstrated by Gary (2019) in their lecture handout, also referenced here.

Consider using one unit of a two-element interferometer with B_{proj}, whose fringe spacing is $\theta = 30$ arcseconds, to respond to a point source in the sky with amplitude a_1, located at an angular distance $\theta_1 = 10$ arcsec. The phase φ_1 will be $\varphi_1 = 2\pi\theta_1/\theta = 2\pi/3$. The *cosine* component of the interferometer measured is $x = a_1\cos(2\pi/3) = -a_1/2$, and the *sine* component: $y = a_1\sin(2\pi/3) = \sqrt{3}a_1/2$. As shown in Figure 4.3 (a) and (b), for a point source with a_1 and θ_1, the interferometer response in terms of a_1 and φ_1 on the phasor diagram. This vector shown in the phasor representation can be written as:

$$a_1\ exp(i\varphi_1) = a_1\ exp(i2\pi\theta_1/\theta) \tag{4.7}$$

Then, when considering more than one point source in the sky, such as two point sources, the resultant response of the interferometer is the vector sum of the two vectors corresponding to the individual responses of each source (refer to Figure 4.3 (c) and (d)). This vector sum can be expressed mathematically as:

$$a_r\exp(i\varphi_r) = a_1\exp(i2\pi\theta_1/\theta) + a_2\exp(i2\pi\theta_2/\theta) \tag{4.8}$$

Expand this concept further, when observing a continuous distribution of brightness (source with size) in the sky, it can be considered as a collection of point sources, and the vector sum can be conclude by:

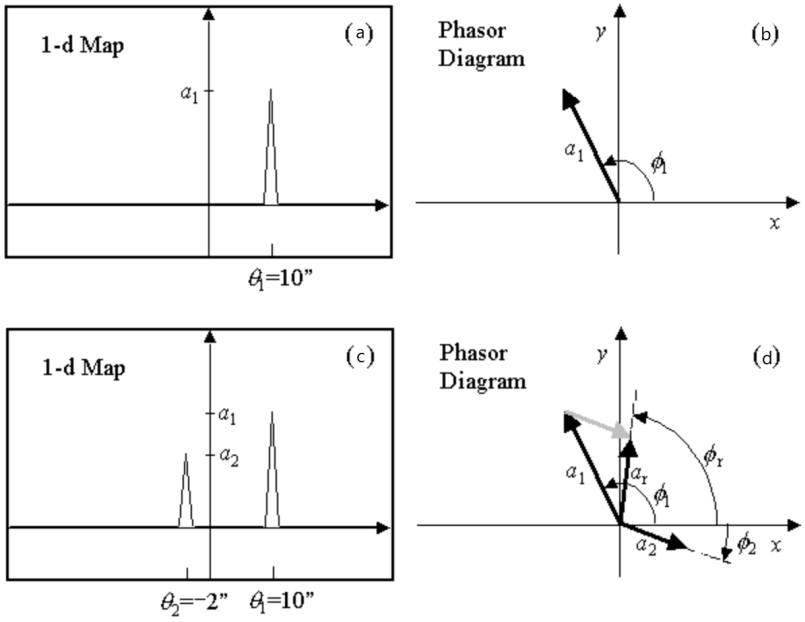

Figure 4.3: (a): The 1-D spatial map of a point source in the sky with amplitude a_1 and spatial coordinate θ_1. (b): The interfeomneter responds in terms of amplitude a_1 and phase φ_1. (c): Two Point Sources with a_1, a_2 and θ_1, θ_2 on 1-D spatial map. (d): Phasor diagrame of the interferometer responds to the two point source in (c), a_r and φ_r are the vector sum of the two source respondses. Credits by Gary (2019)

$$a_r \exp(i\varphi_r) = \sum_i a_i \exp(i2\pi\theta_i/\theta) \tag{4.9}$$

Imaging: From Measured Visibilities to Dirty Map

To perform interferometric imaging of a radio source on a two-dimensional sky plane, it is necessary to measure the two-dimensional spatial frequency spectrum in the u,v plane. The spatial frequency is defined by $s = (u^2+v^2)^{1/2}$, with $s^{-1} = \theta = the fringe spacing$. Similarly, it is essential to define a two-dimensional coordinate system, l,m, on the sky, with its origin being the reference position or phase reference position. Specifically, for two spatial coordinates x,y in meters, the corresponding spatial frequencies, u,v, in wavelengths are defined as $u = x/\lambda$ (the x-component of s) and $v = y/\lambda$ (the y-component of s), measured along axes in the east–west and north–south directions, respectively. l and m are defined as the cosines of the angles between the direction (l,m) and the u and v axes, respectively. Therefore, if we limit our image to a small area of sky near the phase center (small

angular coordinates l, m), l and m can be approximated as the components of this angle, measured in radians, in the east–west and north–south directions, respectively.

Using these variables, the equation 4.9 becomes:

$$a_r \exp(i\varphi_r) = \sum_i a_i \exp((i2\pi(ul + vm))) \tag{4.10}$$

and the left hand side of this equation is the definition of the response of the interferometer, as 'complex visibility', $V(u,v)$. Also, define the brightness distribution of the sky is $I(l,m) = a_i$. And there is a two-dimensional Fourier Transform relationship between $V(u,v)$ and $I(l,m)$:

$$V(u,v) = \int\int I(l,m) \exp(-i2\pi(ul + vm)) dl dm \tag{4.11}$$

Inversely, the sky brightness distribution $I(l,m)$ can be obtained by measuring the 'complex visibility' $V(u,v)$ and apply the inverse Fourier Transform:

$$I(l,m) = \int\int V(u,v) \exp(i2\pi(ul + vm)) du dv \tag{4.12}$$

In conclusion, if there is an area of the sky with a distributed brightness, it can be described by the sky brightness distribution $I(l,m)$. The visibility function $V(u,v)$ is then the Fourier Transform of this brightness map (refer to Figure 4.4 (a) and (d)).

Furthermore, as the Earth rotates and the source moves across the sky, the process of an interferometer measuring visibility function u, v (actually after sampling the visibilities) over an extended period is known as Earth Rotation Synthesis, results the projected baselines to change with time, tracing out portions of elliptical paths. (See Gary (2019)'s lecture notes figure 9. for an array of antennas Earth Rotation Synthesis).

Sampling the visibilities and make a dirty map

We understand that each sky brightness distribution $I(l,m)$ corresponds to a specific visibility function $V(u,v)$. However, a radio interferometer does not measure the continuous $V(u,v)$. Instead, it utilises a series of antenna pairs (forming an array of antennas) to measure only certain values within the continuous (u,v) range

in the visibility function. This subset of measurements is referred to as the sampling function, denoted as $S(u,v)$, and also called the u,v coverage. The sampled visibility function, expressed as $S(u,v)V(u,v)$, constitutes the actual data provided by the interferometer array. By performing the inverse Fourier Transform on this data, we obtain the 'dirty image', denoted as $I_D(l,m)$, given by:

$$I_D(l,m) = \int\int S(u,v)V(u,v)\exp(i2\pi(ul+vm))dudv \tag{4.13}$$

We recognize the Fourier Transform of the sampling function, $S(u,v)$, as the synthesized beam, $B(l,m)$, also known as the point-spread-function (PSF) or the diffraction pattern of the aperture. This implies that if we observe a unit point source at the phase center, we can obtain the brightness map of $B(l,m)$. Consequently, the 'dirty image' (or the dirty map) is the result of convolving the synthesized beam with the true brightness of the source, expressed as $I_D(l,m) = B(l,m) * I(l,m)$.

Up to this point, we have obtained images of the sky (the 'dirty map' $I_D(l,m)$) from the actual measurements of the coherence function (the sampled visibilities, $S(u,v)V(u,v)$). Figure 4.4 from Gary (2019) illustrates the relationship between visibility, the sampling function, sampled visibility, the sky map, the synthesized beam, and the dirty map.

Until this stage, we have introduced the basic concept of interferometric imaging, which involves measuring sampled visibility and producing a 'dirty map' of the sky's brightness. In practical scenarios, several tasks related to imaging data processing need to be undertaken throughout the above steps. These tasks include, but are not limited to:

- Calibration of the visibility: Using a source with a known position to determine the location of the antennas in the interferometric system, thereby enabling high-accuracy observations of unknown sources. (See section 10.1 in the book by Thompson et al., 2017)

- Weighting of the visibility data: This is done to control the point spread function because the synthesized beam may have large sidelobes, akin to typical antennas, which need to be minimized. (See section 10.2.2 in the book by Thompson et al., 2017)

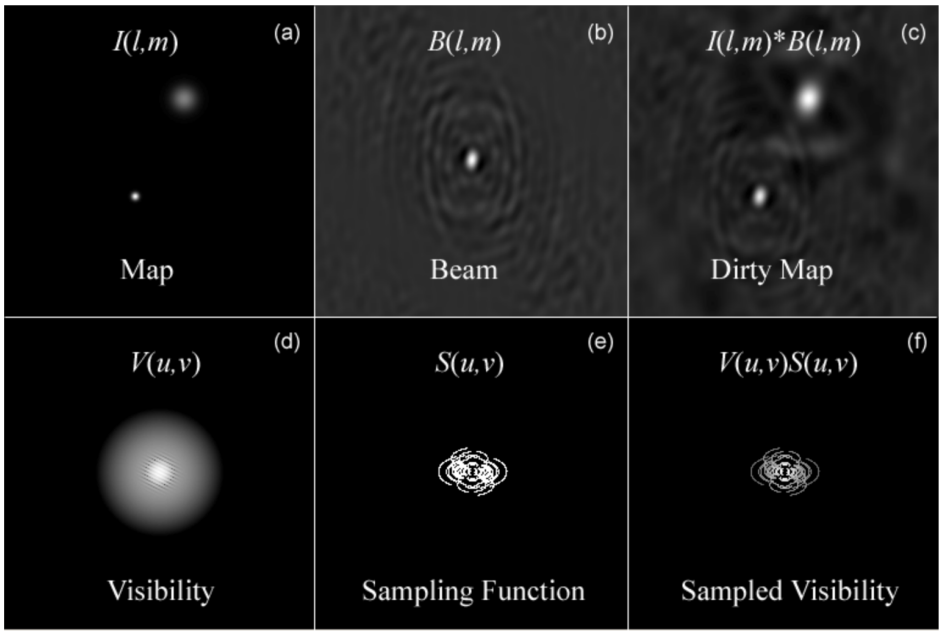

Figure 4.4: (a) An example sky map showing the distribution of brightness. (d) The Fourier Transform of the map produces the visibility function. (e) The sampling function of the interferometer, whose Fourier Transform yields the synthesized beam shown in (b). (f) The sampled visibilities, representing the actual measurements made by an interferometer, whose Fourier Transform generates the dirty map as depicted in (c). (c) The dirty map, which is the convolution of the synthesized beam with the true brightness of the source. Credit for this illustration goes to Gary (2019).

Deconvolution: From 'Dirty map' to 'CLEAN map'

After obtaining a dirty map image, a process known as 'Deconvolution' is necessary to produce a high-quality image (the desired radio image) that closely resembles the original sky brightness distribution. This step involves the use of the CLEAN deconvolution algorithm, a critical tool for generating the restored image. The algorithm estimates the main lobe (the 'clean beam') of the point spread function (PSF) and adds the residuals. The CLEAN algorithm, devised by Högbom (1974), is now the most successfully developed algorithm based on the same function and is widely applied in astronomical interferometric imaging. For detailed and additional information, I recommend Chapter 11 of the book by Thompson et al. (2017).

Conclusion of Using the Solar Interferometric Imaging Technique in This Thesis

The whole Section 4.1 has summarized some important steps, starting from the principle of how a basic unit of an interferometer (comprising two antennas)

responds to plane waves and sources in the sky, through to generating a 'dirty map' of the sky, and then to the deconvolution of the 'CLEAN map'. The algorithms for all these steps are thoroughly detailed in the comprehensive textbook by Thompson et al. (2017). The work presented in Chapter 6 involved imaging a type U burst observed by LOFAR, utilizing the LOFAR interferometric imaging data and the corresponding software to process the data through the steps introduced in this section. Specifically, these software and packages include:

1. LOFAR's The Default Pre-Processing Pipeline (DPPP): provides functions for flagging, averaging, gain calibration, and various other operations. (See the corresponding section of the LOFAR Imaging Cookbook webpage: Diepen & Dijkema, 2021)

2. WSClean: Stands for 'W-stacking CLEAN', provides functions for deconvolution, gridding, weighting, and imaging. (See the WSclean paper by Offringa et al. (2014), and the WSclean manual webpage: Offringa (2023))

4.2 Ground-based instrument 1: The LOw-Fequency-ARray (LOFAR)

The Low Frequency Array (LOFAR, and International LOFAR Telescope (ILT); van Haarlem et al., 2013) is a new generation low-frequency radio interferometer designed and constructed by the Netherlands Institute for Radio Astronomy (ASTRON). As the left map in Figure 4.5 shows, LOFAR is an international radio interferometer network consists of thousands of antennas in 38 stations in the Netherlands, six stations are in Germany, three in Poland, and one station each in France, Ireland, Latvia, Sweden, and the United Kingdom, plus more stations to be build in the future in Italy and Bulgaria (updated informations of stations can be found in ASTRON website: AST, 2024).

LOFAR is capable of operating in frequency ranges from 10 to 240 MHz. This range is critical for a broad spectrum of astrophysical studies due to the Earth's ionospheric cutoff 'radio window' near 10 MHz, which describes the range of frequencies of EM waves that can propagate through the Earth's atmosphere and thus be observed by ground-based observatory facilities. To fully explore this low-frequency

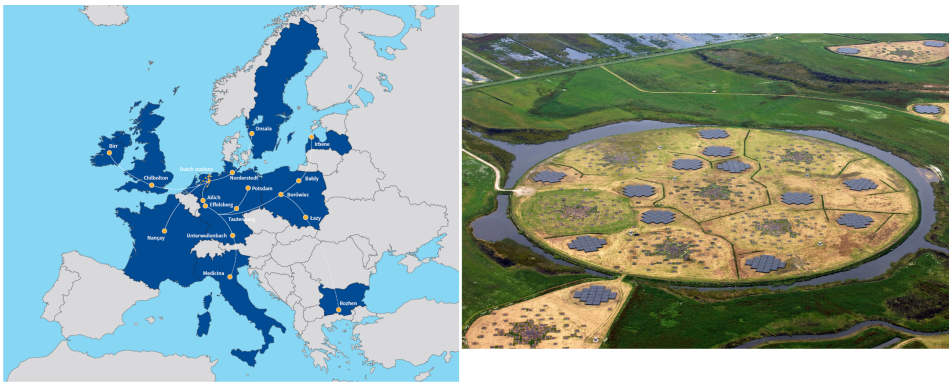

Figure 4.5: Left map: The current map of international LOFAR telescopes AST (2024). Right photo: Aerial photo of the Superterp, the heart of the LOFAR core. There are groups of big black blocks laying in arrays in the photo, these are high-band antennas (HBAs), and the small blocks are low-band antennas (LBAs). van Haarlem et al. (2013)

regime, previously under-observed, LOFAR provides measurements with unprecedented resolution, including temporal resolution in subseconds and frequency resolution in kHz, and offers interferometric radio imaging with resolutions of tens of arcseconds (van Haarlem et al., 2013).

LOFAR's dipole antenna stations have no moving parts and are distributed across Europe. All pointing can be done electronically, and they can point in multiple directions simultaneously. Signals from individual dipole stations are digitized and then transported via a high-speed fibre network, known as the LOFAR Wide-Area Network (WAN), to a central processing facility located in the north of the Netherlands. Data streams from individual dipole stations are combined and further processed by the Central Processing Systems (CEP).

Further processing includes interferometric imaging, tied-array beamforming, and real-time triggering on incoming station data streams. The major advantage of CEP is that multiple processes can run in parallel.

The photo on the right of Figure 4.5 shows the Superterp, which is the heart of the LOFAR core. From the photo, it can be clearly seen that LOFAR has two types of small and relatively low-cost receiving elements: high-band antennas (HBAs, 110 - 240 MHz) and low-band antennas (LBAs, 10 - 90 MHz).

For the lower frequency band, the LOFAR LBAs operate from the ionospheric radio cutoff window at around 10 MHz to the radio band around 90 MHz, which corresponds to the plasma frequency between coronal altitudes of roughly 0.7 to 1.4

solar radii above the solar photosphere. However, in Figure 4.6, the spectra on the left show that the effective performance in both the lowest frequency bands (around 10 MHz) and the higher frequency bands between 80 to 90 MHz are limited due to the appearance of strong radio-frequency interference (RFI).

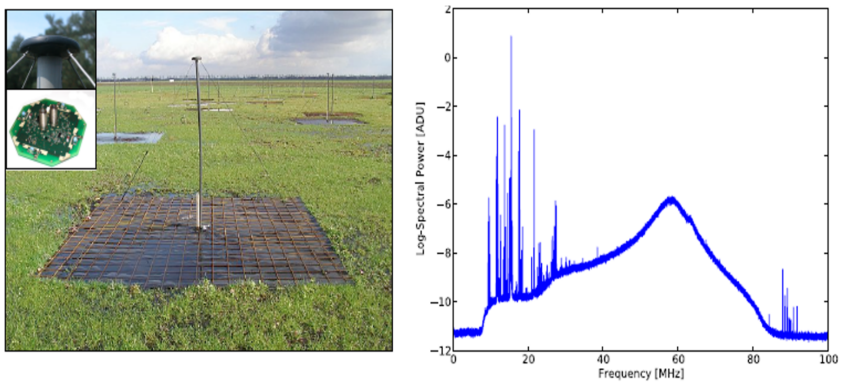

Figure 4.6: Left photo: a single LOFAR LBA dipole including the ground plane. Right: median average spectrum of LBAs in station CS003. Peaks are due to ionospheric reflection of sub-horizon RFI back towards the ground.

The LOFAR High-Band Antennas (HBAs) operate in the frequency range of 110-250 MHz. However, the range above 240 MHz experiences strong Radio Frequency Interference (RFI), so the default operational band is between 110-240 MHz. Although HBAs encounter similar RFI issues as Low-Band Antennas (LBAs), the degree of RFI varies across the entire frequency band and is much less pronounced than in LBAs. Due to the design of the Receiver Unit (RCU), there are three frequency bands available in HBAs: 110-190 MHz, 170-230 MHz, and 210-250 MHz.

LOFAR can operate in beamformed mode, providing not only tied-array beam images but also high time and frequency resolution dynamic spectrum data. To produce radio images, the beamformed mode sums the beams from multiple stations and forms an array of beams, called a 'tied-array beam', which divides the sky within the Field of View (FOV). A notable example is the work by Morosan et al. (2015), from which Figure 4.7 is derived. In this work, they mapped the solar disk (the yellow circle) and its surroundings using 170 tied-array beams to 'chop' the sky plane in the Hexagon FOV. The red circle in (a) represents the full-width half-maximum (FWHM) of the beam at zenith at 60 MHz. Figures (b) and (c) show dynamic spectrum data measuring solar radio flux during the same period,

displaying different signatures of multiple radio bursts as their beams pointed to different positions over the solar disk, resulting in varying intensity values even at the same time and frequency band.

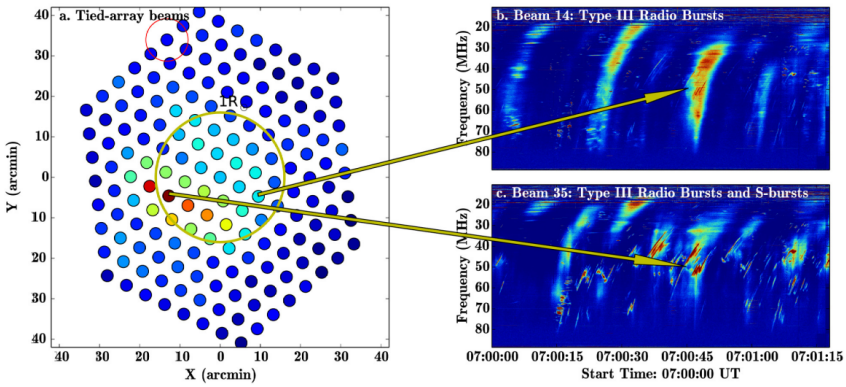

Figure 4.7: LOFAR tied-array beam imaging observation of solar radio bursts. (a) Map of 170 beams in an array forming the tied-array beam, covering the sun in a field-of-view (FOV) of approximately 1.3°. (b) and (c) show the dynamic spectrum of station beams 14 and 35 during the same period, respectfully. The arrows pointed at these dynamic spectra at the same time and frequency band represent the corresponding intensity value in (a). (This figure credit: Morosan et al., 2015)

Another data output provided by the beam-formed mode is the high-resolution dynamic spectrum data, produced by summing up multiple stations' flux measurements after correcting for geometric delay. In this thesis, we intensively analyse LOFAR solar dynamic spectrum data produced by this mode.

Another LOFAR mode used in this thesis is the interferometric mode. The basic concept of the interferometric imaging technique has been introduced earlier in this chapter. Operating in this mode, the central correlator of LOFAR produces correlated visibilities involving as many station beams as possible across the international LOFAR network. The data is then stored in a file format known as 'measurement set' (MS), ready for further processing using various LOFAR interferometric imaging pipelines. In the second science chapter (Chapter 6) of this thesis, we used the Default Pre-Processing Pipeline (DPPP; Diepen & Dijkema, 2021) and WSClean (Offringa et al., 2014) to conduct all the necessary steps to produce high-frequency, temporal, and spatial resolution solar radio images from the raw MS files recorded by LOFAR operating in interferometric mode.

4.3 Ground-based instrument 2: e-Callisto solar spectrometer

e-Callisto (Compound Astronomical Low frequency Low cost Instrument for Spectroscopy and Transportable Observatory: Benz et al., 2009b) is an international solar radio spectrometer networks that continuously observe the solar radio spectrum for 24h per day through all the year through world-wide distributed instruments/stations, as shown in Figure 4.8 the world map with e-Callisto network distributions. Each stations' Observation coverage during a year can be accessed at e-Callisto website at Monstein & Claudia (2023).

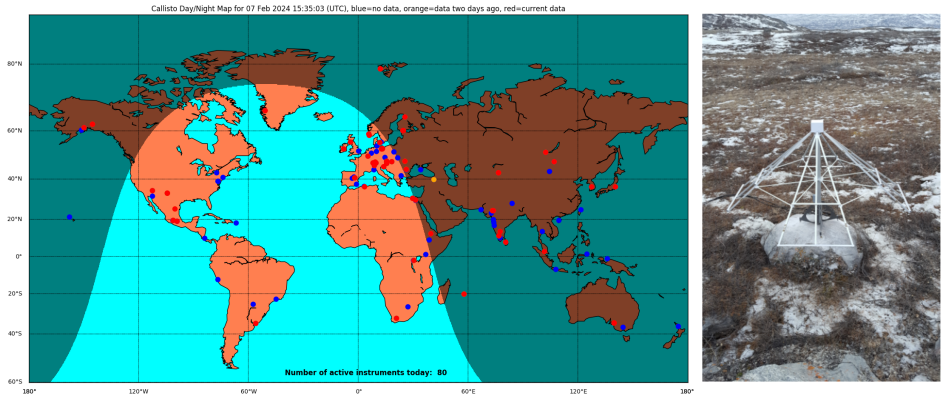

Figure 4.8: Left: World map and e-Callisto instruments and stations distribution. Each dot on the map represents up to five antennas, with different designs and operating in different frequency ranges. Right: The e-Callisto Greenland station's antenna at Observatory ISR Kellyville near Kangerlussuaq in Greenland. This antenna operates between 10 - 110 MHz and provides the radio burst measurements for the U-burst studied in Chapter 6, offering the capability of below 20 MHz observations in addition to LOFAR's range. (Figures credit: Monstein & Claudia, 2023)

The e-Callisto instruments operate in different frequency ranges, as there are various types of antennas across the worldwide networks (a description of e-Callisto spectrum files can be found at Monstein & Claudia (2023)). The station and antenna we used in this thesis is the Greenland station, which uses a circular polarisation antenna (see Figure 4.8 right photo) operating between 10 to 110 MHz. Figure 6.1 displays the U-burst by combining e-Callisto and LOFAR dynamic spectra to show that the turning frequency of the U-burst is below 20 MHz, where LOFAR has limited ability to take measurements due to RFI.

4.4 Ground-based instrument 3: Nancay Decameter Array (NDA)

The Nançay Decameter Array (NDA) was erected between 1975 and 1977 at the radio astronomy station near the village of Nançay in Sologne, France, with the principal aim of routinely monitoring Jovian and solar decametric (DAM) emissions in the 10–100 MHz (30–3 m) range from the Earth's surface. As a high gain phased array of relatively modest size, the NDA consists of 144 helical antennas, yielding an effective area of roughly 7000 m^2 at 25 MHz. It is organised into two sub-arrays for right-handed and left-handed polarisation, each featuring a wide main lobe (approximately 6 $\times$ 10 degrees). For detailed insights, refer to the review by Lamy et al. (2017) on NDA observations and related science.

A multitude of scientific findings regarding the solar corona have been derived from NDA observations, including studies on electron beam propagation in the upper corona (, e.g., Briand et al. (2008); Kerdraon et al. (2010); Melnik et al. (2015)) and the research presented in Chapter 6 of this thesis (Zhang et al., 2024). This work leverages circular polarisation measurements from the NDA, utilising both the NewRoutine and Mefisto receivers, which filter data on-the-fly, for frequencies above and below 35 MHz. These observations are crucial for determining the emission mechanisms of the U burst under study.

4.5 Space-based instrument: Parker Solar Probe (PSP-FIELDS)

Parker Solar Probe (PSP) is a NASA mission that travels much closer to the Sun than any previous spacecraft in human history (Fox et al., 2016). It was launched on 12 Aug. 2018 and flew within 9 solar radii of the solar corona for the first time in history, taking in situ measurements that revolutionise our understanding of the solar corona.

There are five main instruments onboard the PSP spacecraft, with the most important scientific payloads to this thesis being the Electromagnetic Fields Investigation (FIELDS) (Bale et al., 2016), shown in Figure 4.9. This instrument is primarily designed for measuring the electromagnetic fluctuations in the solar wind.

It contains five antennas, four outside the heat shield and one in the shade of the shield. As part of the FIELDS payload, the Radio Frequency Spectrometer (RFS) is designed to take measurements of solar radio bursts in the inner heliosphere (see Pulupa et al., 2017) between 10 kHz to 19.2 MHz.

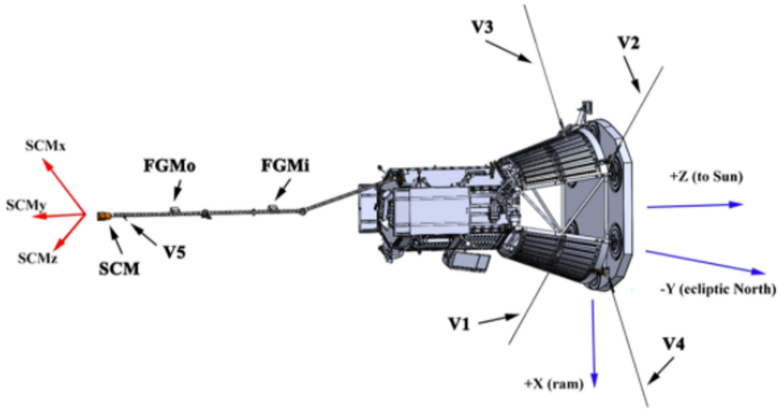

Figure 4.9: PSP FIELDS. The RFS electric field measurements (bandwidth from 10 kHz to 19.2 MHz) come from four antennas v1-v4 mounted near the PSP heat shield, and magnetic field measurements come from the MF winding of the search coil magnetometer (SCM). (Figure credit: Pulupa et al., 2017)

Compared to LOFAR, PSP FIELDS captures solar radio bursts in a lower frequency range, correlating to higher coronal altitudes (roughly from 5 $R_{\odot}$ to 0.5 AU). The combination of PSP and LOFAR measurements on the same burst or burst storm provides a complete picture of the accelerated electron beam propagation from the middle corona to the upper corona and interplanetary space. In the first science chapter (Chapter 5), combining PSP-FIELDS and LOFAR measurements of the same solar radio storm reveals identical flux structures of type III bursts continuations in the interplanetary type III burst region (see Figure 5.1).

Chapter 5

Science Chapter 1 - Deriving Large Coronal Magnetic Loop Parameters Using LOFAR J burst Observations

Zhang et al. (2023), Solar Physics (first-authorship publication, been published)

5.1 Abstract

Large coronal loops around one solar radius in altitude are an important connection between the solar wind and the low solar corona. However, their plasma properties are ill-defined as standard X-ray and UV techniques are not suited to these low-density environments. Diagnostics from type J solar radio bursts at frequencies above 10 MHz are ideally suited to understand these coronal loops. Despite this, J-bursts are less frequently studied than their type III cousins, in part because the curvature of the coronal loop makes them unsuited for using standard coronal density models. We used LOFAR and PSP-FIELDS solar radio dynamic spectrum to identify 27 type III bursts and 27 J-bursts during a solar radio noise storm observed on 10 April 2019. We found that their exciter velocities were similar, implying a common acceleration region that injects electrons along open and closed magnetic structures. We describe a novel technique to estimate the density model in coronal loops from J-burst dynamic spectra, finding typical loop apex altitudes around 1.3 solar radius. At this altitude, the average scale heights were 0.36 solar radius, the average temperature was around 1 MK, the average pressure was 0.7 mdyn cm^{-2}, and the average minimum magnetic field strength was 0.13 G. We discuss how these parameters compare with much smaller coronal loops.

5.2 Introduction

During the early stages of researching solar radio bursts, Maxwell & Swarup (1958) observed a new spectral characteristic in solar radio emissions with an inverted "U" shape on dynamic spectra. Since then, this type of burst has been called the type U solar radio burst. If there is no emission on the second half of the burst (descending leg), such bursts are called inverted type J or simply J-bursts. J and U-bursts are generally known as fast-drift solar radio bursts (e.g. Krueger, 1979) according to their rapid frequency drift from high to low frequency, although U-bursts also have a positive drift rate on the descending leg. Both J and U-bursts are generally believed to be generated by accelerated electron beams propagating along closed magnetic loops in the solar corona (e.g. Klein & Aurass, 1993; Karlicky et al., 1996). Similar to J-bursts, the most common fast-drift burst is the type III solar radio burst (see review by Reid & Ratcliffe, 2014), which is generally accepted to be produced by electron beams traveling along "open" flux tubes.

The plasma emission mechanism based on the work of Ginzburg & Zheleznikov (1959) is the most accepted radio emission process for the majority of these coherent fast-drift solar radio bursts. Electron beams generate Langmuir waves near the local background plasma frequency. These Langmuir waves can subsequently coalesce with ion sound waves and are converted into electromagnetic waves at the same frequency, a process known as fundamental emission. Langmuir waves can also coalesce with other Langmuir waves travelling nearly in the opposite direction to produce electromagnetic waves at double the Langmuir wave frequency, a process known as harmonic emission. One signature of harmonic emission is the low degree of circular polarization, around 10 % (Dulk & Suzuki, 1980), with fundamental emission having a higher average circular polarization, around 35 %. During solar type III burst storms, fast-drift bursts are usually observed with a low degree of polarization, indicating that harmonic emission is more common (e.g. Kai et al., 1985). The degree of circular polarization of U-bursts between 10 – 300 MHz is generally low, which suggests that J and U-bursts are more commonly produced by harmonic emission in this frequency range (e.g. Labrum & Stewart, 1970; Aurass & Klein, 1997).

Thanks to the development of the plasma emission mechanism theory, fast-

drift radio bursts are important diagnostic tools for probing solar coronal loop characteristics when the plasma density is too low for standard EUV and X-ray analysis, around $10^{7.5}$ cm^{-3} at altitudes around one solar radius and above. For the low background plasma densities at these altitudes, we note that Coulomb collisions do not play a significant role in electron beam kinetics. As well as coronal loop characteristics, we can also use these radio bursts to identify the properties of the electron beams that drive radio burst emission.

The electron beam velocity can be estimated by knowing the exciter travel distances by estimating a coronal density model, and the time duration from the dynamic spectra. In general, type III bursts exciter velocities are generally accepted between 0.1 and 0.5 c (e.g. Reid & Ratcliffe, 2014; Carley et al., 2016). Poquerusse (1994) estimated exciter velocities of normal type III bursts (in range 100 to 500 MHz) of $v_e \approx 0.3$ c, where c is the speed of light, by assuming a density model with scale height $H \lesssim 10^5$ km. They found velocities of electron beams generate type-IIId bursts close to the speed of light because they have shorter observed characteristic frequency drift time (≈ 0.7 second). Similarly, type III bursts exciter speed estimated by Dulk et al. (1987) in the frequency between 30 and 1980 kHz had an average speed of 0.14 c, which is close to Klassen et al. (2003)'s estimation that the average exciter speed of interplanetary (IP) type III bursts is 0.15 c. Between frequencies 30 to 70 MHz, Reid & Kontar (2018a) selected 31 type III bursts observed by LOFAR and derived average exciter velocities from the peak time of each radio burst is around 0.17 c in average.

Estimating exciter velocities cannot be directly applied on J-bursts. This is because the curvature part of the J-burst dynamic spectrum is due to an accelerated electron beam travelling along the bent part of the closed loops, where standard numerical coronal density models cannot be applied. Many studies determined J-burst exciter velocities using different methods. Labrum & Stewart (1970) analysed 29 clearly defined U-bursts in the 10 – 200 MHz range and estimated average exciter speed at 0.25 c by using time duration measured at double of the turnover frequency. Reid & Kontar (2017) measured three J and U-bursts' exciter velocities by estimating the exciter positions using radio images, finding average speed determined from the peak time of the radio bursts was 0.21 c. At higher frequency ranges, other

studies estimated the beam velocity between 0.16 c to 0.53 c using the Coulomb collisional time (e.g. Yao et al., 1997; Wang et al., 2001; Fernandes et al., 2012).

Based upon exciter velocity studies, it is generally considered that J and U's exciter velocities have the same order as exciter velocities from type III bursts (e.g. Labrum & Stewart, 1970). However, what is not clear is whether the same active region would produce accelerated electron beams with similar velocities near the footpoint of magnetic loops confined to the corona (emitting J-bursts) and magnetic loops that extend into the heliosphere (emitting type III bursts). Different properties might be expected in these magnetic loops, e.g. very different plasma properties exist near the footpoint.

As well as exciter velocities, the physical parameters of coronal loops can be determined by analysing J or U-bursts. For example, Aschwanden et al. (1992) analysed three U-bursts detected by the *Very Large Array* (VLA) in the range of 1.1 – 1.7 GHz in August 1989. After measuring average electron beam velocities of 53 Mm/s (0.18 c), Aschwanden et al. (1992) derived loop apex altitudes around 130 Mm and determined the upper limit for the density scale height was $\approx$ 370 Mm. Aschwanden et al. (1992) provided another way of determining the scale height value, using the definition of scale height for the coronal plasma in thermal equilibrium and deriving the scale height from the observed loop apex temperature. Many high frequency U and J-bursts studies derived the loop pressure by using the Rosner–Tucker–Vaiana Law (RTV Law: Rosner et al., 1978), which describes the relationship between the loop size, temperature and pressure (e.g. Aschwanden et al., 1992; Yao et al., 1997; Wang et al., 2001; Fernandes et al., 2012). Moreover, the lower limit of the magnetic field strength is mostly determined by applying the plasma β formula, which is the ratio of thermal to magnetic pressure.

Although Aschwanden et al. (1992) provides a good example for determining coronal loop physical parameters and electron beam properties from U-bursts, the coronal loop is low in altitude due to the high observational frequency range provided by VLA. Lower frequency range J-bursts have been studied in a similar way as well. Recently, Dorovskyy et al. (2021) analysed a U-burst observed by the *Giant Ukrainian Radio telescope* (GURT) on 18 April 2017 in the frequency band 10 – 80 MHz. Dorovskyy et al. (2021) assumed a beam speed similar to observed

type III exciter speeds at 0.2 c for fundamental emission and 0.33 c for second-harmonic emission. Dorovskyy et al. (2021) then estimated the density profile of the closed coronal loop by assuming the loop temperature at 1.4 Mk (and twice as high temperature 2.8 Mk) from Mann et al. (1999)'s measurement.

We analyse type III and J-bursts observed during a solar radio noise storm. In Section 5.4, we analysed 27 type III and 27 J-bursts observed by LOFAR between 20 to 80 MHz. We classified radio bursts by combining LOFAR and PSP dynamic spectrum to check continuities of type III bursts and drift rate of J-bursts. Then, we determined exciter velocities from the drift rate of type III bursts and the high frequency part (type-III-like part) of J-bursts to make the comparison. In Section 5.5, we analyse 24 selected J-bursts during the radio noise storm and inferred ambient plasma density model of coronal loops by assuming the exciter velocity remains constant while travel along closed flux tubes and loop top geometry is semi-circular in shape. Then we estimated coronal loop parameters (including temperature, pressure and minimum magnetic field strength) distributions of the loop top by using the density scale height value from the inferred density model. In Section 5.6, we discuss the results of the comparison between exciter velocities propagated along the "open" and "closed" coronal loops. We also compare the physical parameters we estimated for large coronal loops to smaller loops estimations studied by Aschwanden et al. (1992). Moreover, we discuss factors that affect coronal loop physical parameters estimations in this work.

5.3 Instruments and Observations

5.3.1 LOFAR Observations

We focus on a solar radio burst noise storm, which was observed on the 10th of April 2019 from 13:42 to 15:39 UT by the LOFAR LBA that operate between 20 and 80 MHz. We used the data from the LOFAR observation project LT10_002. LOFAR provides high resolution spectral data with a sub-band width of 0.192 MHz and a time resolution of 0.01 s. To improve the signal to noise ratio for the radio burst spectroscopy analysis, we integrate the time resolution to approximately 0.1 s. The 60 MHz bandwidth was covered irregularly using 60 sub-bands. Type III and J-bursts were mostly observed during the solar radio burst noise storm, which pro-

vides opportunities to statistically analyse both types of radio bursts during the same solar activity event.

5.3.2 PSP observations

We used data measured by the PSP-FIELDS. The radio noise storm occurred during the second PSP perihelion observing campaign and so FIELDS was in burst mode, providing the time–frequency spectrum of radio flux observations with a temporal resolution of seven seconds. The high-frequency receiver (HFR) has 64 frequency channels between 1.3 and 19.2 MHz (see Krupar et al., 2020).

The combination of PSP and LOFAR measurements provide a relatively larger scale picture of the accelerated electron beam transport and the coronal structure along its travel path. We used data from RFS/HFR because its highest frequency channel (19.7 MHz) is close to LOFAR LBA's lowest channel (20 MHz), which provides the best continuities between the two spectra. An example of ten minutes of data during the radio noise storm is presented in Figure 5.1. On 10 April 2019, PSP was 0.25 AU away from the Sun and 0.78 AU away from the Earth. The radio signal took approximately six minutes to travel to LOFAR after being observed by PSP. We corrected the time difference between the PSP and LOFAR measurements when we combined the dynamic spectrum in Figure 5.1.

5.4 Electron Beam Velocities

5.4.1 Classification of Type III and J-Bursts

During the noise storm, fast drift solar radio bursts were observed on the LOFAR dynamic spectrum between 20 to 80 MHz, and the PSP observed interplanetary (IP) type III solar radio bursts between 1.3 to 19.2 MHz. We classified a type III burst as a radio burst that was observed both by LOFAR and by PSP. For example, from the ten minutes of data in Figure 5.1, we can see on the PSP dynamic spectrum (upper panel) there are five radio bursts that can be identified as type III bursts that extend below 20 MHz. As Figure 5.1 shows, the lower sensitivity of PSP means that many weaker type III bursts were observed in LOFAR but not in PSP, and they were ignored for this study. We classified a J-burst as a radio burst that showed a clear turnover frequency in the LOFAR dynamic spectrum before 20 MHz. By combining the PSP and LOFAR observations in different wavelength ranges, we

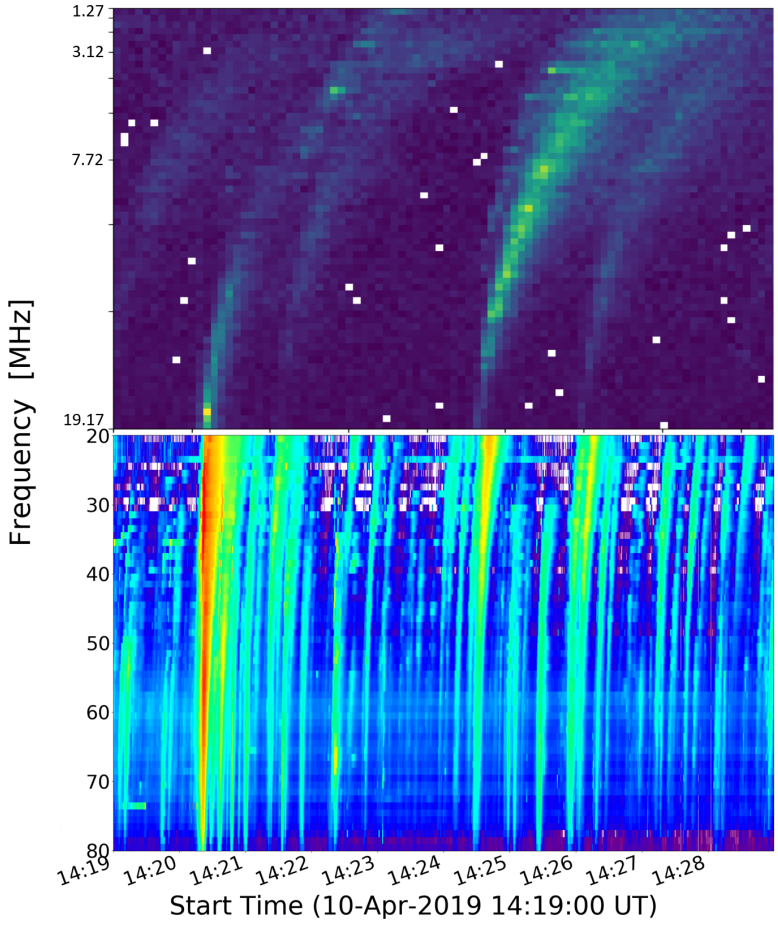

Figure 5.1: Ten minutes of data combining LOFAR and PSP dynamic spectrum, used for classifying type III and J-bursts during the noise storm on the 10th April 2019. Top: PSP RFS radio observations between 1.3 – 19.2 MHz; Bottom: LOFAR LBA observation between 20 – 80 MHz. There are five interplanetary (IP) type III bursts identified in the PSP dynamic spectrum that are also observable by LOFAR.

identified 27 type III bursts and 27 J-bursts.

5.4.2 Velocity Estimations

Whilst electron beam velocities have been estimated from type III bursts and J-bursts individually in many studies, electron beams velocities have never been simultaneously reported during the same radio noise storm. Despite having similar reported velocities, we aim to identify here whether there is any systematic trend between electron beams accelerated in closed and open flux tubes. The electron beam (exciter) velocity is related to the frequency drift rate of radio bursts via

$$\frac{\mathrm{d}f_\mathrm{e}}{\mathrm{d}t} = \frac{\mathrm{d}f_\mathrm{e}}{\mathrm{d}n_\mathrm{e}} \frac{\mathrm{d}n_\mathrm{e}}{\mathrm{d}l} \frac{\mathrm{d}l}{\mathrm{d}t}, \tag{5.1}$$

where f_e is the plasma frequency, $\frac{df_e}{dt}$ is the frequency drift rate, n_e is the background electron density, l is the path of the electron beam, and $\frac{dl}{dt}$ is the exciter velocity.

We identified the maximum flux points for each frequency sub-band for the selected bursts on the LOFAR dynamic spectrum to determine the drift rate. Figure 5.2 shows an example of a type III burst (left) and a J-burst (right) between 45 to 80 MHz. The black dots are the maximum flux points in time. Note the nearly constant frequency drift rate for the type III burst between 80 and 45 MHz, and the change in the frequency drift rate for the J-burst around 50 MHz. These maximum flux points provide the temporal and frequency profile of the bursts drifting on the dynamic spectrum. By assuming fundamental or second-harmonic emission, we converted the observational frequencies f_{obs} to the ambient plasma frequencies f_e ($f_{obs} = f_e$ for the fundamental emission, $f_{obs} = 2f_e$ for the second-harmonic emission). Then we converted the plasma frequency to the ambient plasma density and applied a solar coronal plasma density model to determine associated distances, and hence we obtained the exciter velocities of our identified type III bursts. We assumed the Saito model (Saito et al., 1977) times a factor of 4.5. The multiplier of the density model's magnitude was derived by Reid & Kontar (2017), who derived three empirical density models multiplied by constant factors to fit the three J/U-bursts density distributions. The Saito $\times$ 4.5 density model is given by

$$n_e(r) = 4.5 \times \left(1.3 \times 10^6 \left[\frac{r}{R_\odot} \right]^{-2.14} + 1.68 \times 10^8 \left[\frac{r}{R_\odot} \right]^{-6.13} \right), \tag{5.2}$$

where $n_e(r)$ is the coronal electron number density, in units of cm^{-3}, as a function of solar radius r measured from the solar centre.

The J-bursts have exciters that are propagating along the apex of a coronal loop. Therefore the standard coronal density model, which assumes an open flux tube does not capture how the corresponding plasma density changes at the apex of these closed coronal loops as the geometry is different. Therefore we defined the "type-III-like" part of the J-bursts as the ascending leg where the drift rate remains roughly constant. For the J-burst shown in Figure 5.2 this was above 60 MHz. We then found exciter velocities from the J-burst maximum flux points in this higher

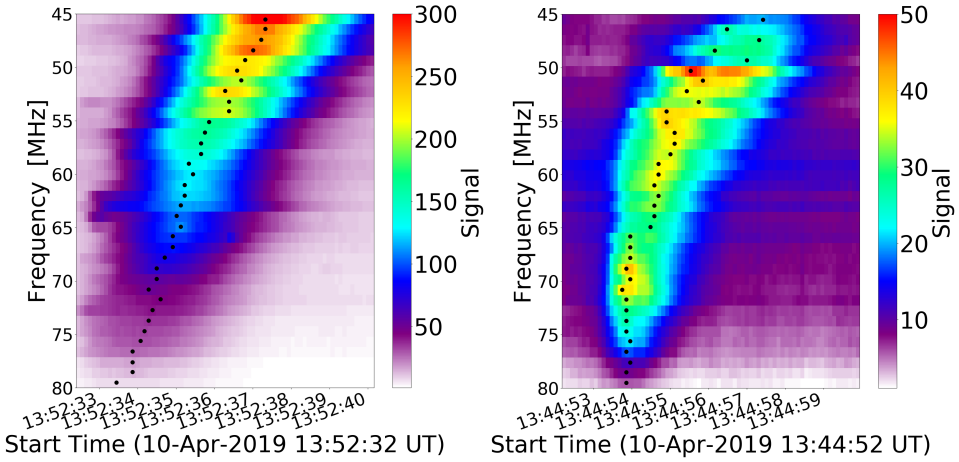

Figure 5.2: Type III burst (**left**) and a J-burst (**right**) on the dynamic spectrum. Type III and J-bursts show rapid drift from high to low frequencies. Type III bursts have relatively constant frequency drift rate, and J-bursts show decreased frequency drift rate. **Black dots** on both dynamic spectra are maximum flux points for each frequency band, and their time profiles show frequency drift.

Table 5.1: Average exciter velocities of all identified type III and J-bursts.

	Fundamental emission Average velocity [c]	Second-harmonic emission Average velocity [c]
27 type III bursts	0.16 ± 0.03	0.18 ± 0.05
27 J-bursts	0.17 ± 0.04	0.22 ± 0.05

frequency range, where there was no obvious change in the frequency drift rate, using the same density model as we used for the type III bursts.

Table 5.1 shows the average exciter velocities found by analysing all the identified type III and J-bursts. Under the assumption of fundamental emission mechanism, type III bursts average exciter velocity is 0.16 c which is very close and within the standard deviation of the J-bursts' average at 0.17 c. If all identified bursts are assumed as second-harmonic emission, type III burst exciters' average velocity is 0.18 c which again is within one standard deviation of the J-burst average exciter velocity of 0.22 c. Although type III and J-bursts' exciter velocities are close, there is a systematic increase in the J-burst exciters compared to the type III burst exciter velocities.

5.5 Physical Parameters of Coronal Loops

This section introduces the methodology and strategy for determining large coronal loops' parameters directly from J-burst dynamic spectrum data. These physical properties include:

1. Inferring the coronal plasma density model of the coronal loop top, yielding the coronal density scale height, λ, of such large loops.
2. The loop temperature distribution, $T(r)$, as the gravitational acceleration varies along the loop.
3. The loop pressure distribution, $P(h)$, using the ideal gas law.
4. The loop minimum magnetic field strength, $B(h)$, using the condition of plasma beta being less than one.

There are some important assumptions used throughout the methodology, summarised here:

1. Assuming Saito's model multiplied by 4.5 for calculating the electron beam velocity from the high-frequency part of each J-burst, where the numerical density model is valid.
2. Assuming the electron beam propagates along the coronal loop at a constant speed. This assumption is used to determine the travel distances of the electron beam along the loop top part.
3. Assuming the loop top part is assumed to be semi-circular in shape. This helps to determine the heights of the radio sources, and therefore the loop's altitude.
4. Assuming the solar coronal plasma is in hydrostatic equilibrium, to determine the loop's temperature from the density scale height and the local gravitational acceleration.

Figure 5.3 is a flowchart summarising the methodology for determining coronal loops' physical parameters from 24 selected J-bursts during the noise storm. Each step is detailed in the corresponding subsections.

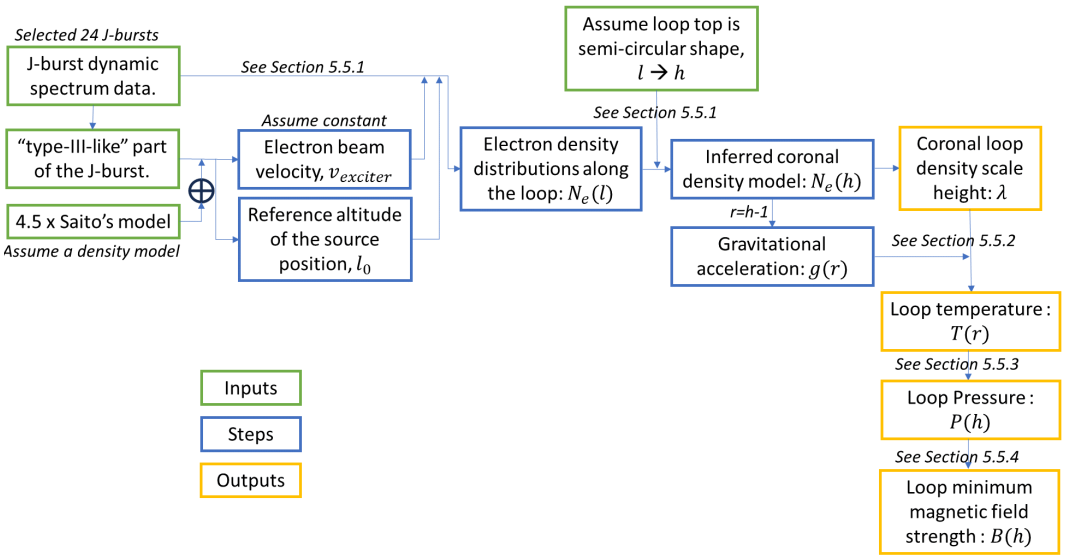

Figure 5.3: Flowchart of methodology deriving large coronal loops' physical parameters directly from J-burst dynamic spectrum data.

5.5.1 Coronal Loop Density Model

The change in the drift rate of the J-bursts at the turnover frequencies provides information about the change in electron density at the apex of the closed magnetic loops. We can therefore use the J-burst drift rates to estimate the background electron density of large coronal loops.

We begin by estimating the travel distance of the electron beam along the loop top, where the generated radio flux exhibits decreases in frequency drift rate. Assuming that the exciter velocity does not change along the loop, we determine the travel distance using the exciter velocity, v_{exciter}, calculated from the "type-III-like" part of the J-burst, and the times, t of the maximum flux points in the J-burst. The travel distance along the coronal loop $l(t)$ is given by

$$l = l_0 + v_{\text{exciter}}(t - t_0), \tag{5.3}$$

where l_0 is the reference altitude of the source position, derived from the highest frequency of the J-burst and our assumed density model (Saito model $\times$ 4.5). The start time t_0 is the time of the max flux point at this frequency, and the term $t - t_0$ is the travel time of exciter along the apex of the magnetic loop.

The travel distance along the loop, l, does not reflect the altitude of the loop

apex. If we want to know the loop altitude, we must assume the loop geometry. In this study, we assume the loop top is a semi-circle. We then converted the travel distance profile along the loop l to a solar altitude h.

We determined the coronal loops' electron density distributions with solar altitude $n_e(h)$ using the times of maximum flux at each frequency and the exciter profile in solar altitude as a function of time. Assuming that the coronal loop is in hydrostatic equilibrium, we then model the $n_e(h)$ with an exponential of the form

$$n_e(h) = n_0 \exp\left\{\left(\frac{-h}{\lambda}\right)\right\}, \tag{5.4}$$

where n_0 is the reference plasma density, a constant derived from density associated with the height l_0, and λ is the hydrostatic density scale height.

During this solar radio storm, we identified 24 J-bursts for inferring the coronal density model and deriving large coronal loops' physical parameters. These J-bursts have frequency drift rates that decreases in the lower frequency range and relatively noiseless dynamic spectrum backgrounds.

From all 24 selected J-bursts, we found a total of 898 frequency sub-bands ranging between 25 and 80 MHz. Using the time of maximum flux for all individual sub-bands, we found the average loop altitudes and hence the average electron density model within the loops. The minimum and maximum solar altitudes above the photosphere were from 0.79 to 1.85 $R_\odot$, respectively. The average density model is shown in Figure 5.4a. The points were averaged every 0.1 $R_\odot$ from 0.79 to 1.42 $R_\odot$, which contained 94.2 % of all maximum flux points in this range. There were only a few J-bursts that extended to higher altitudes. The electron number density decreases from 2.0×10^7 cm^{-3} to 1.6×10^6 cm^{-3}. The error bars in Figure 5.4 represent the standard deviation of all points considered.

In Equation 5.4, the value of the scale height, λ, is inferred by fitting an exponential curve to the $n_e(h)$ profile derived from maximum flux points of each selected J-burst. The average background coronal density scale height of 24 inferred coronal loop plasma density models is 0.36 $R_\odot$ ($2.5 \times 10^{10} \pm 4.9 \times 10^9$ cm). The largest density scale height we derived among 24 J-bursts is 0.5 $R_\odot$ (3.5×10^{10} cm), and the lowest is 0.26 $R_\odot$ (1.8×10^{10} cm). The average value of N_0 is 5.1×10^9 cm^{-3}, from the lowest 5.1×10^8 to the largest 1.8×10^{10} cm^{-3}.

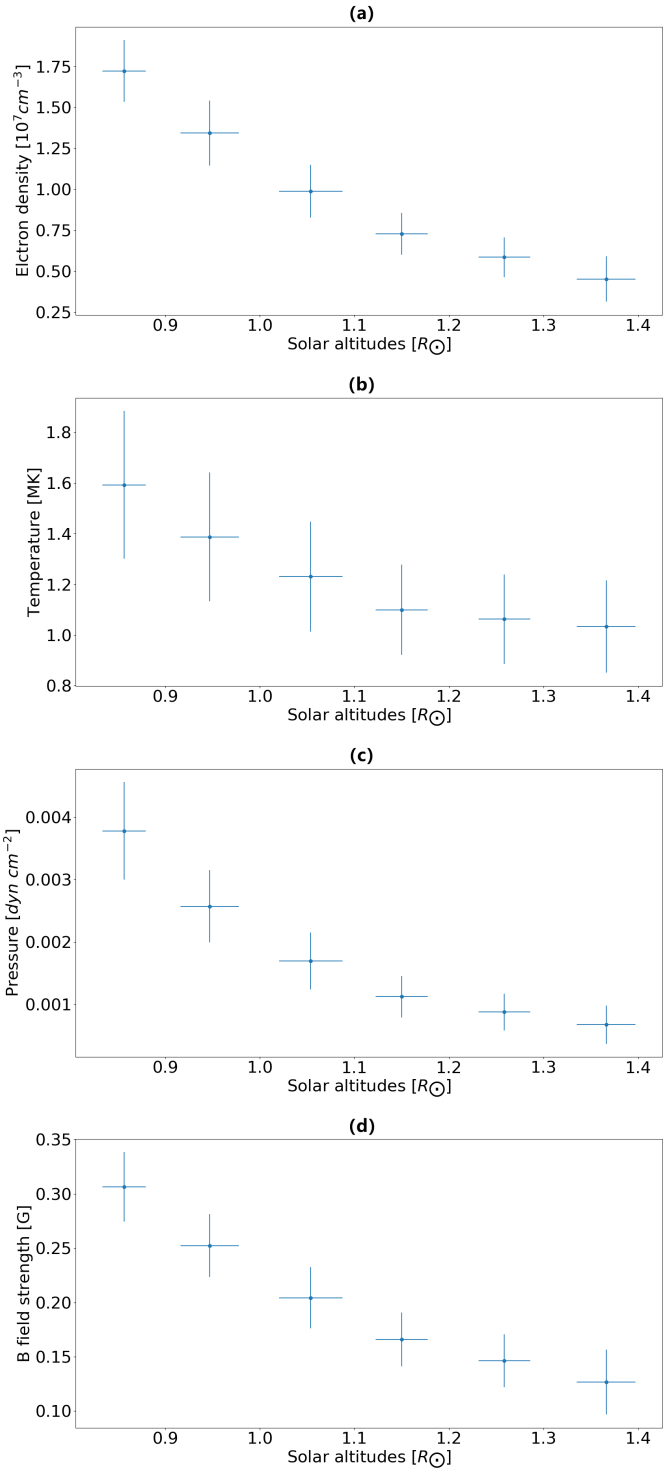

Figure 5.4: Coronal loop plasma parameters inferred from 24 J-bursts, averaged every 0.1 solar radius. **(a)** electron density, **(b)** temperature, **(c)** pressure, **(d)** minimum magnetic field strength. Error bars are calculated from the standard deviations to show the spread in results. The value is the average of each 0.1 solar radius.

5.5.2 Coronal Loop Temperature

The density scale height λ is proportional to the electron temperature T and inversely proportional to the gravitational acceleration of the Sun. Assuming the solar coronal plasma is in hydrostatic equilibrium, the density scale height λ, as determined from the exponential density model in Equation 5.4, is given by (see Aschwanden et al., 1992; Aschwanden & Acton, 2001)

$$\lambda = \frac{1+\alpha}{\beta}\frac{k_B T}{m_P g_\odot}, \tag{5.5}$$

where $\alpha = 1.22$ is the ratio of electron to proton number, and $\beta = 1.44$ is the mean molecular weight, k_B is the Boltzmann constant, m_P is the mass of a proton, and $g_\odot$ is the gravitational acceleration. In contrast to the U-burst studied at the high frequencies by Aschwanden et al. (e.g. 1992), we analysed J-bursts at much lower frequencies, and hence much larger coronal altitudes. Whilst Aschwanden et al. (e.g. 1992) assumed the value of $g_\odot$ at $1\,R_\odot$ from the solar centre, we considered $g_\odot$ as a function of solar altitude such that

$$g_\odot(r) = \frac{GM_\odot}{r^2}, \tag{5.6}$$

where G is the gravitational constant, $M_\odot$ is the mass of the Sun, and r is the distance from the centre of the Sun, such that $r = h + 1$.

For each selected J-burst, we determined the coronal loop temperature distributions as a function of solar altitude by combining Equation 5.5 and Equation 5.6 such that

$$T(r) = \frac{\beta}{1+\alpha}\frac{m_P \lambda}{k_B}\frac{GM_\odot}{r^2}, \tag{5.7}$$

where λ is the density scale height value inferred from the selected J-burst. Similar to the gravitational acceleration, the loop temperature is inversely proportional to the square of solar altitude.

By analysing all 24 J-bursts, using the 898 frequency sub-bands, the lowest temperature was 0.7 MK, and the highest temperature was 2.1 MK. The loop-top temperature decreases from the lower to the upper solar corona. Figure 5.4b shows the average temperature is 1.6 MK at the beginning around $0.86\,R_\odot$ and then drops

to 1.0 MK around 1.37 $R_\odot$ above the photosphere.

5.5.3 Coronal Loop Pressure

To obtain the loop pressure, $P(h)$, we applied the ideal gas law

$$P(h) = n_e(h) k_b T(h), \tag{5.8}$$

using our previously deduced background electron density profile $n_e(h)$ and the temperature profile $T(h)$. Figure 5.4c shows the average loop pressure decreasing with increasing altitude, from 3.8×10^{-3} dyn cm^{-2} aroud 0.86 $R_\odot$ to 0.7×10^{-3} dyn cm^{-2} around 1.37 $R_\odot$.

5.5.4 Coronal Loop Magnetic Field Strength

It is generally accepted that the magnetic pressure is larger than thermal pressure in the solar corona. This is the reason that accelerated particles in the solar corona propagate along magnetic field lines as they are "frozen" in magnetic fields. The plasma beta, β_p, presents the ratio of the thermal pressure, $P_{thermal}$, to the magnetic pressure, $P_{magnetic}$, which is less than one in the solar corona (see plasam β introduced in Section 2.2).

In a similar way to Aschwanden et al. (1992), we can rearrange the plasma β equation (Equation 2.1) to estimate the upper bound of the magnetic field strength using

$$B(h) > [8\pi n_e(h) k_b T_e(h)]^{0.5}. \tag{5.9}$$

We note that $B(h)$ is proportional to the square root of the plasma pressure and thus has the same trend as the other parameters. Figure 5.4 d shows magnetic field strengths of 0.31 G around 0.86 $R_\odot$ to 0.13 G around 1.37 $R_\odot$.

5.6 Discussion

5.6.1 Type III and J-Bursts Exciter Velocities

By analysing 27 type III and 27 J-bursts, we found that the average exciter velocities were comparable (see Table 5.1). There is a small increase in the J-burst velocities, but any difference between the bursts lies within the standard deviation. The larger velocities under harmonic emission are related to the decreased gradient of the coro-

Table 5.2: Average plasma parameters of large and small coronal loops, near their apex. Large coronal loop parameters were estimated from our 24 low frequency J-bursts, at an altitude of 1.37 $R_\odot$. Small coronal loop parameters were estimated from three high frequency U-bursts analysed by Aschwanden et al. (1992), at altitudes of 0.18 $R_\odot$.

Plasma Parameters	Large Coronal Loops	Small Coronal Loop
Density scale height	$0.36 \pm 0.07\,R_\odot$	$0.51 \pm 0.09\,R_\odot$
Density	$(4.5 \pm 1.4) \times 10^6\,cm^{-3}$	$6.3 \times 10^9\,cm^{-3}$
Temperature	$1.0 \pm 0.2\,MK$	$7.0 \pm 0.4\,MK$
Pressure	$0.0007 \pm 0.0003\,dyn\,cm^{-2}$	$6.1 \pm 0.4\,dyn\,cm^{-2}$
Minimum magnetic field strength	$\geq 0.13 \pm 0.03\,G$	$\geq 12\,G$

nal density model at higher altitudes. Given the same density model assumed for the type III bursts and the initial part of the J-bursts, the radio drift rates are similar. This result reinforces the previous hypothesis that both radio bursts are signatures of electron beams propagating along magnetic loops, with the change in J-burst drift rate indicating electron propagation near the loop apex.

That we do not see much change in the exciter velocity suggests there is no discernible difference in the acceleration properties of the corresponding electron beams. We might have expected a difference because the larger magnetic structures ("open" loops) that are responsible for type III bursts are likely to have smaller background electron densities and temperatures, in a similar way that coronal holes have cooler, less dense plasma to the surrounding corona. It may be the case that the particle acceleration in the radio noise storms occurs at the same region and, accelerated beams have access to different magnetic structures as the particle acceleration evolves over time. Whatever the case, models of radio noise storm acceleration need to take into account the similar electron beam velocities from J-bursts and type III bursts.

5.6.2 Coronal Loop Physical Parameters

The average coronal loop altitudes that we found in this study were around 1.37 $R_\odot$. This altitude is very similar to the 1.45 – 1.6 $R_\odot$ loop apex that was inferred from LOFAR imaging observations of two J-bursts and one U-burst (Reid & Kontar, 2017). The altitudes might be similar as we inferred a background density model (Saito×4.5) that was similar to these large coronal loops. Nevertheless, the similar

loop apex that we found give confidence in our novel technique for estimating the density model in the curved part of these large coronal loops.

The coronal loop altitudes are much smaller than those estimated by Dorovskyy et al. (2021). The main difference between our work and Dorovskyy et al. (2021) is that they did not infer a density model but assumed an exciter speed of 0.33 c. This assumed speed directly led to the large altitudes that they estimated for the coronal loop in the study, and is larger than the speeds that we infer, around 0.2 c.

The average plasma parameters that we estimated can be found in Table 5.2. We report the average plasma parameters at the loop altitude of 1.37 $R_\odot$, near the apex of most loops, as all parameters vary with altitude. We also report the average plasma parameters found by Aschwanden et al. (1992) who analysed three U-bursts observed by the Very Large Array between 1.3 and 1.7 GHz, at an approximate altitude of 0.18 $R_\odot$.

For our larger coronal loops, we found similar density scale heights to Aschwanden et al. (1992). This result implies that density scale heights are independent on the size of the coronal loop. However, more coronal loops should be studied, in different active regions and different altitudes (e.g. 0.6 $R_\odot$) before concluding such a result.

The ratio of density scale height to loop altitude in our study is smaller than one, around 0.26. This is in comparison to being greater than one from the results of Aschwanden et al. (1992). As such, we were not able to use the RTV scaling law (Rosner et al., 1978) to estimate the plasma temperature using

$$T \approx 1.4 \times 10^3 (pL)^{-\frac{1}{3}}. \tag{5.10}$$

Aschwanden et al. (1992) compared both methods, finding very similar plasma temperatures, and hence similar plasma pressures. If indeed the density scale height does not vary significantly with loop height then the RTV law is only useful for more compact coronal loops with altitudes under 0.3 $R_\odot$.

We estimated the loop top temperature of large coronal loops at an average of 1.0 ± 0.2 MK, which is cooler than smaller loops estimated by Aschwanden et al. (1992) at an average of 7 MK. This agrees with conclusions by Dorovskyy et al.

(2021) that large loops have lower loop top temperature than smaller ones. The main difference that we infer from Aschwanden et al. (1992) is that we do not take the value of $g_\odot$ to be constant, but instead vary it as a function of solar altitude, h. The temperature dependence is then proportional to $(h+1)^{-2}$ (see also Equation 6.1), and therefore it naturally explains the smaller temperatures at higher altitudes.

The pressure we obtained at the apex of large coronal loops was significantly smaller than found by Aschwanden et al. (1992). This occurs naturally from the ideal gas law, primarily based upon the smaller densities, as the difference in plasma temperature is minimal.

We found the minimum magnetic field strength of larger coronal loops to be significantly smaller than was found by Aschwanden et al. (1992). Again, this mainly comes directly from the decrease in plasma pressure. If one assumes a standard dipole approximation of $B(r) \propto r^{-3}$, where r is the distance from the centre of the Sun, the 12 G that Aschwanden et al. (1992) find at a distance of $r = 1.18\,\mathrm{R}_\odot$ would correspond to 1.48 G at a distance of $r = 2.37\,\mathrm{R}_\odot$, close to the loop apex we estimate in this study. This is significantly larger than the 0.13 G we estimated from our data. Such a result is expected, given the coronal tendency of the magnetic field to decrease exponentially with altitude (Solanki et al., 2006), due to the increasing volume the magnetic field can fill as r increases. For an exponential model of $B = B_0 \exp(-br)$, we can tentatively use our two data points to find the reference magnetic field of $B_0 = 1.2$ kG and the scale factor of $b = 3.9$. However, one must remember that the magnetic field varies significantly between different coronal loops, and our magnetic field estimates are only a lower estimate, based upon $\beta < 1$.

Zaitsev & Kronshtadtov (2017) discussed two types of coronal loops, which are i) the tube cross-section does not change much with height in the corona and $\beta < 1$; ii) the tube cross-section increases with height and $\beta > 1$. As indicated by Zaitsev & Kronshtadtov (2017), the first loop type is typical for most magnetic loops observed in the corona and is why we used this condition to estimate the minimum magnetic field strength. With a solar wind dependence of $B \propto r^{-2}$ and $B = 3 \times 10^{-5}$ G at 1 AU (e.g. Verscharen et al., 2019), we would predict a magnetic field strength of 0.25 G at $r = 2.37\,\mathrm{R}_\odot$. In the case of the second loop type, the magnetic field strength we estimate would be smaller than 0.13 G. This does not

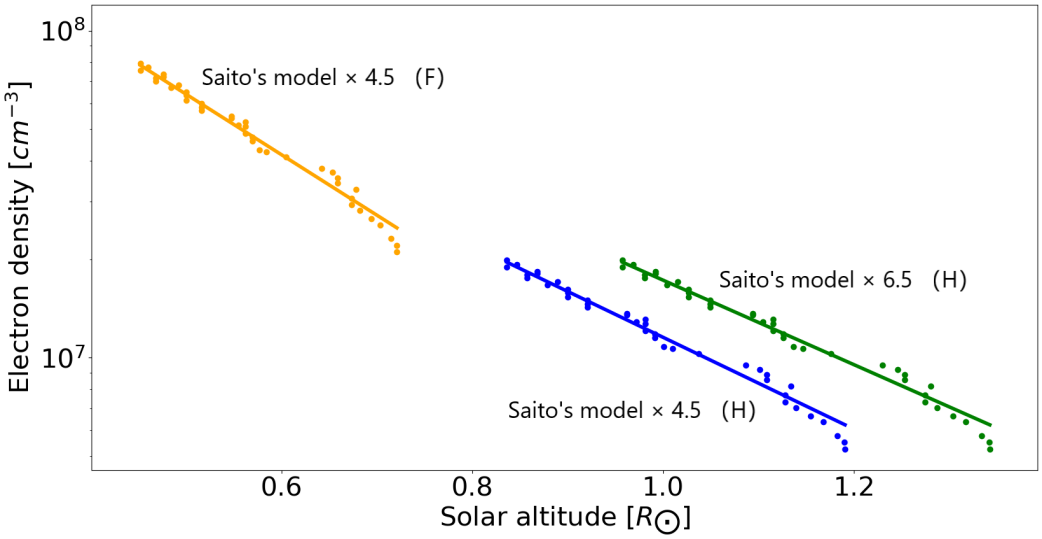

Figure 5.5: Inferred coronal density model from one selected J-burst under different assumptions of emission mechanism (Fundamental or Second-harmonic emissions) and reference coronal density model magnitude (Saito's model ×4.5).

compare well to our extrapolated value of the magnetic field strength using data from 1 AU.

5.6.3 Factors Affecting Coronal Loop Physical Parameters

5.6.3.1 The Reference Density Model Magnitude

We used the Saito model multiplied by 4.5 for estimating average beam velocities from type III bursts and the high frequency part of J-bursts. We then used our estimated beam velocities to infer the background electron density models for the curved apex of large coronal loops. Whilst this modified Saito model was inferred from other J-bursts (Reid & Kontar, 2017), there is an inherent uncertainty in our results because of this density model assumption.

We can test the effect on our results if we change the multiplication factor that we used on the Saito model. Figure 5.5 shows how the inferred electron density in the curved apex of a large loop is modified if we used the Saito model multiplied by 6.5. Because any specific density is now at a larger altitude, the reference altitude of the source position (l_0 in Equation 5.3) is higher, and therefore the estimated loop top altitude is higher. This is evident when comparing the green and blue lines in Figure 5.5, where we have an increase in apex of the coronal loop from 1.19 $R_\odot$ to 1.34 $R_\odot$ above the photosphere.

Using the Saito model multiplied by 6.5 instead of 4.5 leads to higher beam velocities deduced from the radio bursts. When using larger magnitude density models, the range of frequencies that we are analysing correspond to densities that are now farther away from the Sun, where the spatial gradient of the density model is smaller. This leads to longer distances between any given density, and hence the beam needs to travel faster over these long distances as the travel time inferred from the dynamic spectrum is fixed. The result of these higher beam velocities means that using the Saito model multiplied by 6.5 increases our inferred average density scale heights from $0.35\,R_\odot$ to $0.38\,R_\odot$. This change in density scale height is not very significant in our altitude range. With loop temperature, pressure and magnetic field being proportional to the density scale height, the exact density model does not modify significantly the derived plasma parameters at a given altitude. What has a significant effect on plasma parameters at the loop apex is the change in altitude of the coronal loop, as the temperature is proportional to r^{-2}, where r is the distance from the centre of the Sun.

5.6.3.2 Emission Mechanism

We used the assumption of second-harmonic emission to obtain our results, as second-harmonic emission is more prevalent during type III solar noise storms in the upper corona (see Kai et al. (1985) and Section 5.2). Moreover, during the solar radio noise storm we analysed, many J-bursts showed "Fundamental–Harmonic (F–H)" pairs structure on the LOFAR dynamic spectrum. This structure defined by both fundamental and harmonic components appears together, with the fundamental components at a lower frequency range than the harmonic. In this case, we analysed the harmonic components, because the fundamental components typically showed more structure. However, we cannot be completely certain that all of our radio bursts in this study are generated by harmonic emission.

If we assume fundamental emission for all of our bursts, the corresponding electron densities that the electron beam travels through will be higher. This means that the altitudes will be lower. Figure 5.5 shows the derived electron density in the curved apex of a large loop if we assume fundamental emission. We can clearly see the densities are higher and the altitudes are lower. This is evident when comparing the yellow and blue lines in Figure 5.5, where we have an decrease in apex of the

coronal loop from 1.19 $R_\odot$ to 0.72 $R_\odot$.

The effect of assuming fundamental emission for all of our J-bursts reduces the derived loop apex height, from from 1.37 $R_\odot$ to 0.85 $R_\odot$. The average scale height is reduced from 0.36 $R_\odot$ to 0.27 $R_\odot$. Even with a decrease in the average scale height, the reduced altitude of the loop apex means that the 24 J-bursts average loop apex temperature increased from around 1 MK to 1.3 MK. The average plasma density at the loop apex is changed from $0.45 \times 10^7\,cm^{-3}$ to $1.8 \times 10^7\,cm^{-3}$. Moreover, under the fundamental emission assumption compared to harmonic, the average loop top pressure dramatically increases from $0.07 \times 10^{-2}\,dyn\,cm^{-2}$ to $0.3 \times 10^{-2}\,dyn\,cm^{-2}$. Average value of minimum magnetic field strength increases from 0.13 G to 0.28 G. The increase in temperature, density, pressure, and magnetic field are primarily driven by the smaller loops that are inferred by assuming fundamental emission despite the decreases in the average density scale height.

5.6.3.3 Loop Top Geometry

In Section 5.5.1, we introduced the idea that the electron beam travel distance profile along the solar altitude $h(t)$ was converted from the distance profile along the loop by assuming the loop top geometry is a semi-circle. However, it is also common to consider that the loop top geometry is a semi-ellipse (e.g. Dorovskyy et al., 2021). Figure 5.6 shows three scenarios of loop top geometry assumption: (a) tall semi-ellipse, (b) semi-circle, (c) flat semi-ellipse. In the real solar corona, the loop top geometry can be varying between these three scenarios.

In the case that the coronal loop top is a tall semi-ellipse (Figure 5.6a), the electron beam travels to higher altitudes. As such, the inferred background plasma density model will have a larger density scale height and larger loop apex altitudes. The converse is true if we assume the flat semi-ellipse (Figure 5.6c).

The loop cross-section is also an important characteristic to be considered. As mentioned in Section 5.6.2, the loop type (ii) increases cross-section with height, which will cause the density of an electron beam propagating along the loop to decrease. This scenario will contribute towards the reduction of radio waves being produced by the electron beam at the top of the loop, and was discussed in depth by Reid & Kontar (2017). The loop cross-section can be estimated by imaging radio sources. However, exactly what shape coronal loops take near their apex is beyond

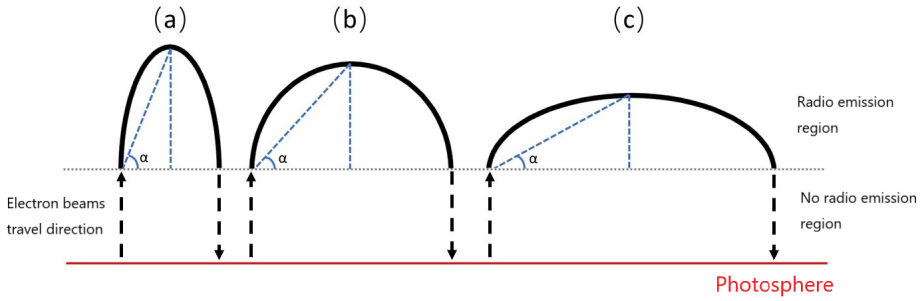

Figure 5.6: Three scenarios of loop top geometry assumptions: **(a)** A tall semi-ellipse: $\tan(\alpha) > 1$; **(b)** A semi-circle: $\tan(\alpha) = 1$; **(c)** A flat semi-ellipse: $\tan(\alpha) < 1$.

the scope of this article and will be a subject of a future study.

5.7 Conclusions

This study estimated solar accelerated electron beam velocities by analysing type III and J-bursts, identified from the same solar radio noise storm observed by LOFAR. After comparisons, we found that the kinetic properties of the electron beams are similar while travelling in "open" or closed flux tubes during the noise storm. This is the first comparison of type III and J-bursts exciter velocities during the same solar radio noise storm.

Solar J-bursts also provide us with an excellent way of estimating the physical parameters of large coronal loops, where the density is too low for typical UV or X-ray diagnostics, and typical coronal density models are not relevant. We described a novel technique for estimating the background density model of large coronal loops just using the spectroscopic data from a radio dynamic spectrum of a solar J-burst. Using data from 24 J-bursts, we inferred the average background density model of coronal loops in an active region. The coronal loop apexes were situated at an average height of $1.37\,R_\odot$, with an average scale height of $0.36\,R_\odot$. We then used the scale height to infer average loop plasma temperatures (1 MK), pressures ($2 \times 10^{-3}\,\mathrm{dyn\,cm^{-2}}$), and minimum magnetic field strengths (0.22 G). These plasma parameters are significantly different from those inferred for smaller coronal loops by Aschwanden et al. (1992) using higher frequency J-bursts. The plasma parameters that we estimated are dependent upon the assumptions that we made about

the coronal loop geometry, the background density model and the emission mechanism. We have showed that our derived plasma parameters are not too significantly affected by modifications in these assumptions and should hold as some of the first predictions of the plasma state in such large coronal loops. Our study has focused on the high resolution spectroscopic data from LOFAR but found similar results for when LOFAR imaging spectroscopy was used (Reid & Kontar, 2017). A further study would be interesting to compare our new technique with a density model estimated from interferometric images, taking into account radio scattering effects (e.g. Kontar et al., 2019), to test the assumption of the electron beam velocity remaining constant as it traversed the apex of the coronal loop.

Chapter 6

Science Chapter 2 - Use a type U burst to image a middle coronal magnetic loop

Zhang et al. (2024), The Astrophysical Journal (first-authorship publication, been published)

6.1 Abstract

Solar radio U-bursts are generated by electron beams traveling along closed magnetic loops in the solar corona. Low-frequency ($<$ 100 MHz) U-bursts serve as powerful diagnostic tools for studying large-sized coronal loops that extend into the middle corona. However, the positive frequency drift component (descending leg) of U-bursts has received less attention in previous studies, as the descending radio flux is weak. In this study, we utilized LOFAR interferometric solar imaging data from a U-burst that has a significant descending leg component, observed between 10 to 90 MHz on June 5th, 2020. By analyzing the radio source centroid positions, we determined the beam velocities and physical parameters of a large coronal magnetic loop that reached just about 1.3 $R_\odot$ in altitude. At this altitude, we found the plasma temperature to be around 1.1 MK, the plasma pressure around 0.20 $\mathrm{mdyn, cm^{-2}}$, and the minimum magnetic field strength around 0.07 G. The similarity in physical properties determined from the image suggests a symmetric loop. The average electron beam velocity on the ascending leg was found to be 0.21 c, while it was 0.14 c on the descending leg. This apparent deceleration is attributed to a decrease in the range of electron energies that resonate with Langmuir waves,

likely due to the positive background plasma density gradient along the downward loop leg.

6.2 Introduction

As introduced in Chapter 3, the solar type U burst can serve as a powerful diagnostic tool to probe the physical parameters of closed coronal magnetic loops and to study the kinetic properties of the accelerated electron beams traveling in these loops, located in the higher region of the corona, such as the middle corona. Furthermore, as introduced in Chapter 2, the middle corona, defined by heliocentric distances from 1.5 to 6 solar radii ($R_\odot$), has a tenuous plasma environment where the density is too low for X-ray and EUV emission diagnostics. The low-frequency U-bursts, observed by ground-based radio interferometers below 100 MHz, are generated by electron beams traveling along large-sized coronal loops that extend into the middle corona, higher than 1.5 $R_\odot$ heliocentric height. These large sized closed magnetic loop structures have been poorly studied due to the historical lack of low-frequency radio imaging, which was present only at a few, discrete frequencies. For example, Stewart & Vorpahl (1977) used 80 and 130 MHz from the Culgoora Radioheliograph. Analysing the negative frequency drift component (ascending leg) and positive frequency drift component (descending leg) of a low-frequency U-burst with high frequency resolution (1 MHz) radio interferometric imaging, such as the capability provided by LOFAR, can determine the velocity of electron beams traveling along both legs of the loop. It can also be used to determine the physical parameters of such large-sized loops, which have historically been ill-defined.

Previous studies have estimated the velocity of electron beams from the ascending leg of U-bursts, where electron beam propagating outwards from the Sun. Using methods similar to those employed in many previous studies on type III bursts (e.g., Poquerusse, 1994; Mann et al., 1999; Reid & Kontar, 2017), one can convert observed frequency to plasma frequency using $f_{\rm obs} \approx f_e$ for fundamental emission or $f_{\rm obs} \approx 2f_e$ for second-harmonic emission. The ambient electron density n_e can be derived. Using a numerical coronal density model, the radial distance of each radio source along the coronal magnetic flux tube, l, can be determined. Therefore, the evolution of frequency in time from a type III burst or the ascending leg of a U-burst can thus provide the electron beam velocity (This method has been

summarized by Reid & Ratcliffe, 2014). Labrum & Stewart (1970) estimated an average beam velocity of 0.25c by analyzing 29 U-bursts below 160 MHz, assuming fundamental emission and Newkirk's coronal density model. Refer to my work in Chapter 5 (Zhang et al., 2023), I determined the electron beam velocity from 27 type J bursts between 20 to 80 MHz observed by LOFAR during the same solar radio noise storm, averaging at 0.22c by assuming second-harmonic emission and multiplying Saito's density model(the background coronal density model by Saito et al., 1977) by a factor of 4.5. However, the limitation of this method is that it cannot be applied to the turning over part and the descending leg of U-bursts. It is because the standard coronal density models cannot be used when the magnetic field lines bend horizontally.

Using solar radio imaging measurements to directly determine the position of radio sources for predicting electron beam velocities and coronal loop parameters has become popular in recent years (see Reid, 2020, as a recent review), thanks to the construction and operation of high-performance new generation radio telescopes, such as LOFAR. By using the LOFAR tied-array beams solar images, Reid & Kontar (2017) estimated the exciter velocities of three U-bursts while they traveled along ascending legs between 40-70 MHz, ranging from 0.16c to 0.20c. However, determining the electron beam velocities from the descending leg was difficult due to the weak and faint emissions across narrow frequency ranges. Similarly, Dabrowski et al. (2023) analyzed the velocities of type-III and U bursts in their study using LOFAR tied-array and interferometric imaging. However, they were only able to determine the exciter velocity of the selected U-burst from the dynamic spectrum, as the extremely diffuse flux in the descending leg made imaging the descending leg challenging, especially in the lower frequency range below 100 MHz. Therefore, imaging low frequency U-bursts with clear and strong descending leg emissions would provide better opportunities for studying the propagation of electron beams along the downward leg of the coronal loops.

Other studies have used U-bursts to determine the physical parameters of coronal loops (e.g., Aschwanden et al., 1992; Fernandes et al., 2012). Using GHz radio observations from the Very Large Array (VLA), Aschwanden et al. (1992) derived the density, temperature, pressure, and minimum magnetic field strength of three

loops around 20 Mm in altitude. At MHz frequencies, using the NRH data, Mancuso et al. (2023) determined coronal loop parameters by constructing the 3D morphology of the loop from five radio source positions on images at three different frequencies (360.8, 327.0, 298.7 MHz). This loop reached about 146 Mm (0.21 solar radii) in altitude. Due to the limited number of frequency bands available for imaging, deriving loop parameters for the ascending and descending leg individually becomes challenging. However, coronal loops that generate U-bursts are commonly assumed to possess symmetrical geometric and physical properties. It remains unclear whether the ascending and descending legs exhibit similar or different physical characteristics, due to the lack of adequate simultaneous measurements of both legs for comparison.

In this work, we study an extremely bright U-burst observed by LOFAR between 10 to 90 MHz on the 5th June 2020. The U-burst has clear descending leg structure from 20 to 40 MHz, which provides opportunities for imaging the descending leg sources positions by using LOFAR interferometric imaging with high frequency resolutions. We estimated electron beam velocities travelled along upward and downward flows based on ascending and descending legs images. We derived coronal loops parameters by inferring plasma density models along the closed loop from radio images. The present chapter is organized as follows. In Section 6.3, we describe the details of the U-burst, including the LOFAR dynamic spectrum and observations from Nançay Decameter Array (NDA) and e-Callisto, as they provided additional information about the event from LOFAR. In Section 6.4, we present the LOFAR radio interferometric image data of the U-burst. We plotted the coronal loop structure over the solar disc and report the radio source characteristics of the U-burst, including source sizes, position, and time. In Section 6.5, we determine the electron beam velocities from both the ascending and descending legs on the image to make comparisons, as well as derive the coronal loop parameters. The discussions of the results are presented in Section 6.6 to address the questions mentioned in this section, including discussions of the scattering and projection effects. finally, section 6.7 concludes the key findings of this paper, and we also suggest future studies of large-size coronal loops and their connections to the low corona and interplanetary space by utilising U-burst events.

6.3 Observations of the U-burst

The U-burst was observed by several ground-based radio telescopes at 09:37:00 UT on June 5th, 2020, between 10 to 90 MHz. Stanislavsky et al. (2021, 2022) reported that the Giant Ukrainian Radio Telescope (GURT), the NDA, the Radio Solar Telescope Network (RSTN), and the e–Callisto Greenland sites observed the event simultaneously. On the LOFAR dynamic spectrum shown in Figure 6.1, it is clear that the event contains a group of type-III bursts preceding and following the ascending leg flux of the U-burst, which represents the negative frequency drift rate leg. This makes it challenging to determine which branch corresponds to the ascending leg flux of the U-burst.

The bright radio flux in the event was observed starting around 09:36:32 UT, consisting of a group of type-III-like bursts (which may also contain J-bursts) that emerged together during a short period of time until 09:36:50 UT. This group of bursts contains the ascending leg of the U-burst. However, the ascending leg flux overlaps with a bright type III burst at 09:36:45 UT on the LOFAR dynamic spectrum. Together, this branch of the flux exhibits the largest temporal width on the dynamic spectrum. As evidence, the e-Callisto dynamic spectrum in Figure 6.1 shows this flux branch separating around 23 MHz into two. The first flux branch drifts towards lower frequencies (around 11 MHz), overlaps with the preceding bright type III burst that starts around 09:36:40 UT and exhibits a relatively constant frequency drift rate. We consider this to be a type-III burst. The second flux branch has a clear characteristic of decreased drift rate, reached the turning over point at around 18 MHz on the e-Callisto dynamic spectrum. Therefore, we have identified the second separated branch as the ascending leg flux of the U-burst. The descending leg of the U-burst is defined as the emissions occurring after the turning point with a positive frequency drift rate. On the LOFAR dynamic spectrum, it can be clearly identified as the flux drifting from 20 to 40 MHz, between 09:37:14 and 09:37:26 UT.

Figure 6.2 displays a NDA composite dynamic spectrum of the Stokes V parameter (Boischot et al., 1980). It merges the data obtained from the NewRoutine and Mefisto (which filters the data on-the-fly) receivers above and below 35 MHz, respectively (Lamy et al., 2017; Lecacheux et al., 2013). We observe that the degree of circular polarization was different for the U-burst and the surrounding vis-

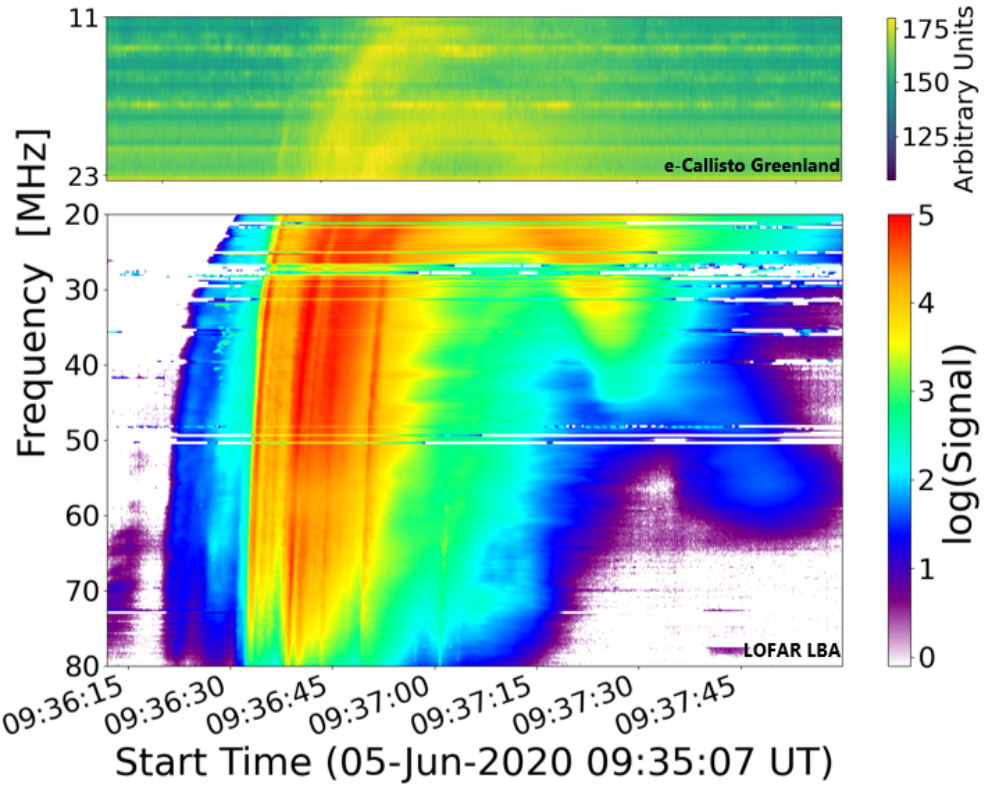

Figure 6.1: Dynamic spectrum of the U-burst event on June 5th 2020. The bottom panel displays the LOFAR dynamic spectrum from 20 to 80 MHz, while the upper panel shows the e-Callisto dynamic spectrum between 11 to 24 MHz. The turning frequency is approximately 18 MHz at 09:37:00 UT.

ible type III bursts. Most of the type III bursts were highly right-handed circularly polarized. The U-burst ascending leg displayed a relatively lower degree of right-handed circular polarization ($|V|/I < 0.2$), which entirely switched to left-handed circular polarization for the U-burst descending leg. The U-burst lower degree of circular polarization allows us to confidently conclude that the emission mechanism is second-harmonic emission, which typically produces low circular polarized radio flux (see Dulk & Suzuki, 1980). In addition, the switch in the sign of Stokes V between the ascending and descending legs (from RH to LH circular polarisation) is consistent with the fact that the electron beam is traveling in opposite directions relative to the observer.

We also report the observation of another descending leg component by LOFAR in this event, which is visible on the log-scale LOFAR dynamic spectrum, as shown in Figure 6.1. The radio flux was recorded between 40 and 60 MHz, from 09:37:40 to 09:38:00 UT. The reason for identifying it as another U-burst rather

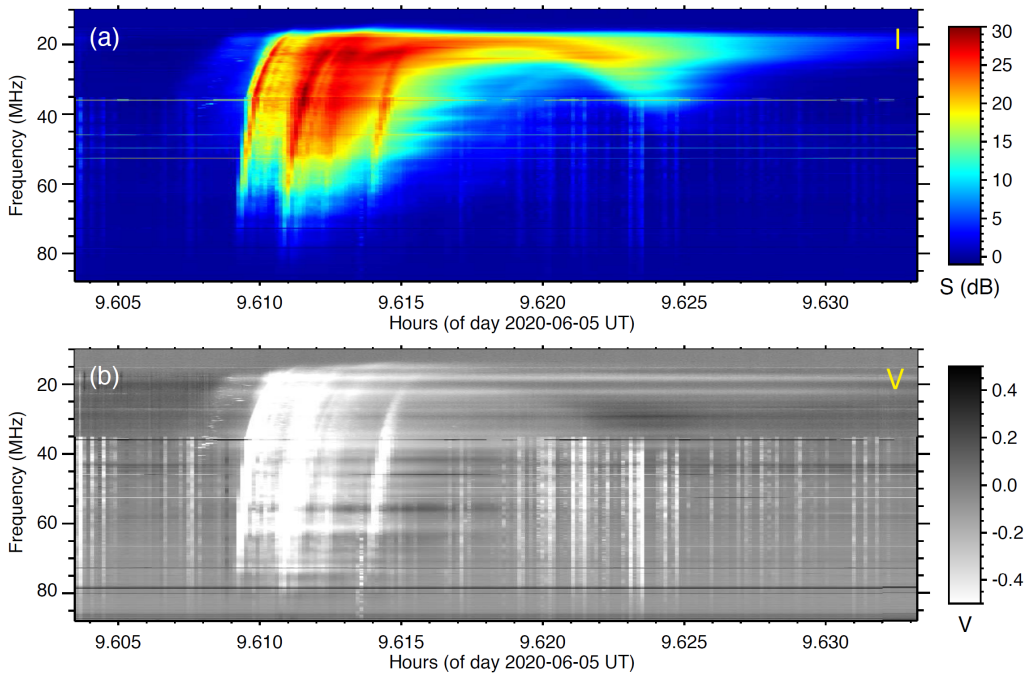

Figure 6.2: NDA composite dynamic spectrum of Stokes I (top) and Stokes V (bottom) using the NewRoutine receiver above 35 MHz and the Mefisto one (RFI-filtered data) below 35 MHz. The type III bursts were highly right-handed circularly polarized ($|V| > 0.4$). In comparison, the U-burst has a lower degree of circular polarization ($|V| < 0.2$). The ascending leg of the U-burst is right-handed circularly polarized whilst the decending leg is left-hand circularly polarised.

than a continuation of the U-burst in this study is because it exhibits a lower frequency drift rate of 1.6 MHz/s, lower than the U-burst descending leg drift rate at 2.3 MHz/s, and two order of magnitude lower in intensity. It is challenging to identify the turning point and ascending leg of this U-burst as they were overshadowed by other bright radio bursts, similar to the main U-burst ascending leg that we are studying.

6.4 LOFAR Interferometric Imaging

The LOFAR interferometric solar imaging dataset consists of imaging data from 60 frequency sub-bands, ranging from 19.13 to 80.07 MHz, with a step of approximately 1 MHz, varying slightly for each sub-band.

6.4.1 The U-burst Image

Since the descending leg of the U-burst stopped emitting at 40 MHz, we primarily utilized the imaging data between 20.70 MHz and 40.03 MHz to generate the ra-

dio source image of the U-burst. The temporal resolution of the imaging data for each frequency sub-band is approximately 1.7 seconds, after being processed using the LOFAR solar image pipeline (The Default Pre-Processing Pipeline (DPPP); Diepen & Dijkema (2021), and WSclean Offringa et al. (2014)). In total, we selected 15 noiseless frequency sub-bands to create the interferometric image of the U-burst. For each selected sub-band, two time intervals were chosen to represent the ascending and descending legs respectively, as black dots labeled on the dynamic spectrum, shown in Figure 6.3. The time profile for the ascending leg was determined based on the peak flux time during the ascending flux period. The time profile for the descending leg can be directly identified on the descending flux branch as the peak flux occurring between 09:37:13 and 09:37:27 UT. Therefore, we have 30 radio images to visualize the propagation of the electron beam along the closed magnetic loops that generated the U-burst. These radio images, overplotted on the AIA 171 Å image of the Sun, depict the propagation of the electron beam along the large coronal magnetic loop, as shown in Figure 6.3. In this image, the contours are plotted at the full width at half maximum (FWHM) representing the sizes of the radio sources along the loop.

The magenta contours on the U-burst image illustrate the ascending leg of the U-burst, collectively demonstrating the outward travel of the electron beam from the Sun. The highest-frequency channel selected for imaging the ascending leg of the U-burst is 40.2 MHz, located at a high altitude off the solar disc in the image. This positioning makes it challenging to detect the origin of the electron beam acceleration, as no GOES X-ray activities have been observed. However, a coronal jet was observed simultaneously from AR12765 during the U-burst event, as shown in Figure 6.4. We consider that the accelerated electron beams that produced the radio emissions of this U-burst event were accompanied by this jet plasma and they were accelerated by the same magnetic reconnection process. This acceleration process produced a minimal amount of emissions compared to typical flares (see Raouafi et al., 2016). The observation of this jet provides evidence supporting that the footpoint of the upward leg of the large coronal loop was located at AR12765.

Chen et al. (2023b) investigated the source positions and directivity of the interplanetary (IP) type III bursts, which were simultaneously observed below 10 MHz

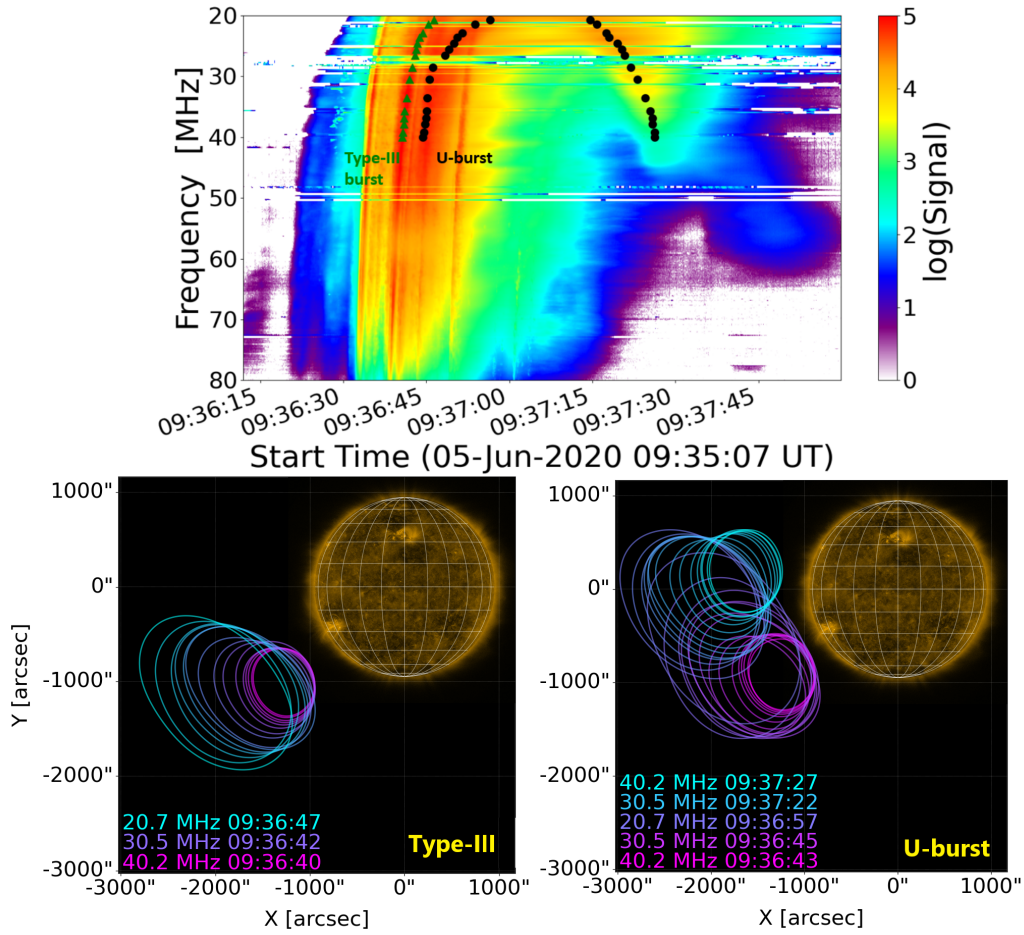

Figure 6.3: Top: dynamic spectrum of the event. The times of peak flux for each image contour are highlighted by green triangles for the type III burst and black dots for the U-burst. Bottom: LOFAR interferometric solar radio image contours taken at 50% intensity for a type III burst (left) and the U-burst (right), between 20-40 MHz. Image contours are overlaid on the AIA 171 Å image.

by the Parker Solar Probe, Solar Orbiter, and STEREO. We established that this interplanetary type III burst was the same event as the U-burst in our study, as it was connected to the type III burst flux we imaged in Figure 6.3. This connection was evidenced by the clear extension of flux to the lower frequency range on the e-Callisto dynamic spectrum, as shown in Figure 6.1. Chen et al. (2023b) employed both intensity fitting and timing methods (indicated by triangle symbols) to determine the positions of the interplanetary type III burst sources. Furthermore, they confirmed that the electron beam originated from AR12765 and that its trajectory was straightforward along the -60° longitudinal plane.

Other type III bursts observed during the ascending period of the U-burst event

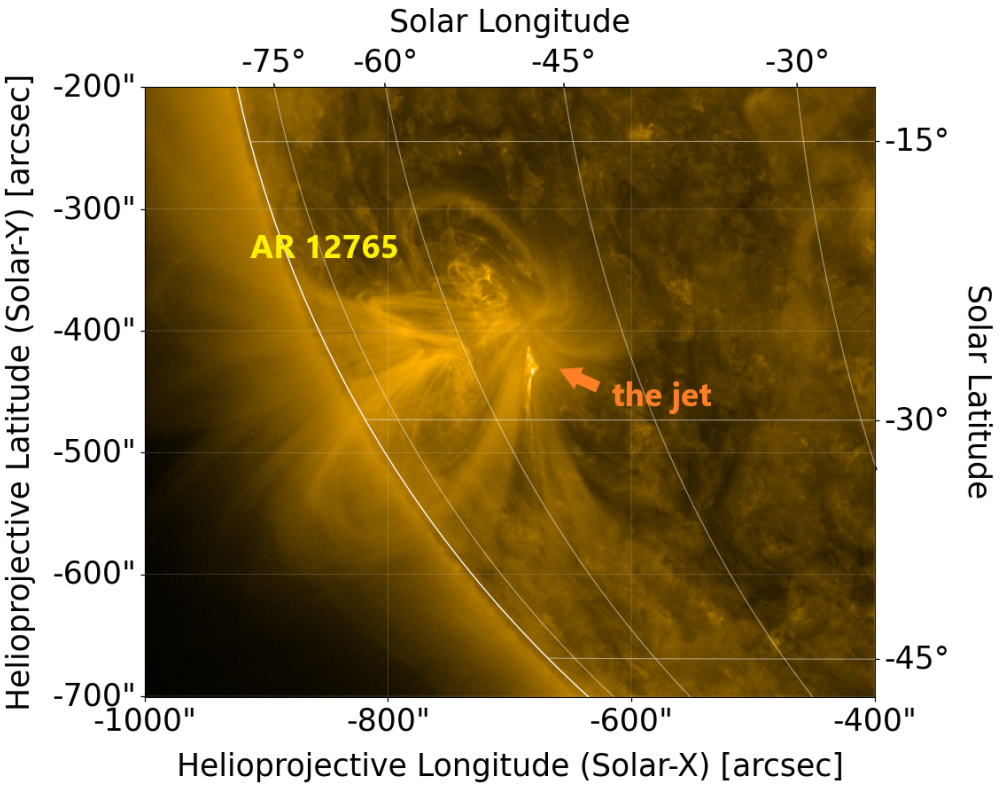

Figure 6.4: AIA 171 Å image of an observed coronal jet that was co-temporal with the U-burst, originating from Active Region AR12765 at 2020-06-05 09:37:45 UT.

also originated from this active region. As an example, we imaged the brightest preceding type III burst, as shown in Figure 6.3; the high-frequency radio sources of the type III burst are spatially close to the ascending leg sources of the U-burst. In this study, we assumed that the ascending leg sources were located on the same longitudinal plane (-60°) as the active region AR12765 at 09:37:00 UT.

The sources in the ascending leg, ranging from 30.5 to 20.7 MHz on the image, depict the electron beam's travel along the upward leg of the large coronal loop drifted towards the north and eventually reached the loop apex above the solar equatorial region. This observation aligns well with the general understanding of the U-burst emission mechanism, which places the emission region of the turning over part of the burst at the loop apex. The radio sources at the lowest frequency of both the ascending and descending legs, observed at 20.7 MHz, exhibit a noticeable shift towards the north. The region in which the loop apex can be considered located is suggested to be within this area based on the image.

The radio sources of the descending leg, indicated by cyan contours on the

U-burst image in Figure 6.3, show that the electron beam is propagating downward from the apex of the loop above the solar equatorial region towards the high-latitude regions in the northern solar hemisphere. This observation suggests that the location of the footpoint for the downward leg of the magnetic loop is in the northern high-latitude regions. Regarding the Potential Field Source Surface (PFSS) global modeling (The lower-boundary magnetic field data for the PFSS models are provided by GONG synoptic magnetograms: Harvey et al. (1996), implemented in a Python package, pfsspy: Stansby et al., 2020), with the source surface set at 2.5 $R_\odot$ as illustrated in Figure 6.5, there are large magnetic field loops connecting AR12765 to various northern high-latitude regions. Likely locations include the southern polar region, the unidentified active region located near the limb, and some field lines connected to the backside of the solar limb. However, none of these loops have a 2D projection that reaches the heliocentric height depicted in the radio image, although the source surface height at 2.5 $R_\odot$ is considered sufficient to display the corresponding large coronal loop from extrapolation. The uncertainty of the coronal loop downward leg footpoint location leads to the challenge of the projection effect, as the true position of radio sources is hard to measure due to the distances along the line-of-sight axis being undetectable. In this study, we assumed that the descending leg sources were located on the same plane as the solar limb for studying the coronal loop physical parameters and the beam velocity. We also discussed the projection effect's influence on the results in Section 6.6.4.

6.5 Electron Beam Characteristics and the Coronal Loop Physical Parameters

6.5.1 Coronal Loop Density Model

The background electron density model of the coronal loop can be directly inferred from the U-burst images. The positions of the radio sources were defined as the centroids of each contour on the image. As explained in the previous section, to approximate projection effects, we assumed that the centroids of the ascending leg radio sources were located on the same longitudinal plane (-60°) as the active region AR12765 at 09:37:00 UT, and the descending leg sources were located on the same plane as the solar limb (-90°). The assumption of both longitudinal planes allows

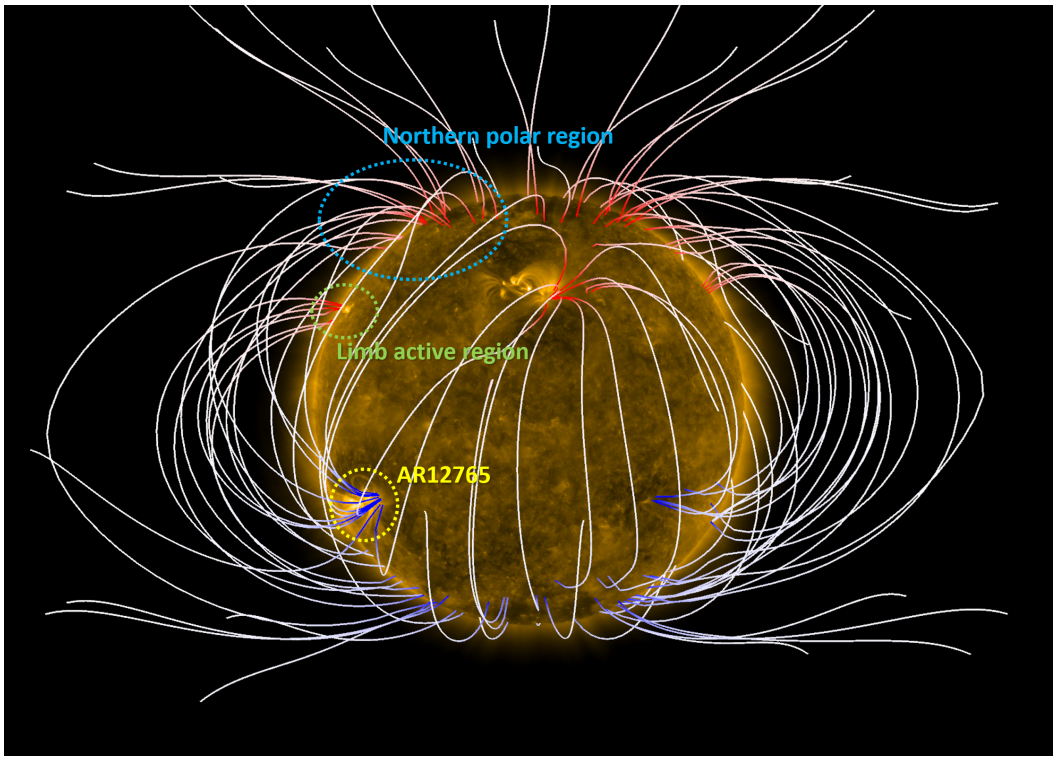

Figure 6.5: Potential Field Source Surface (PFSS) global modelling of the solar magnetic field on 5th June 2020 09:06:37 UT, with the source surface set at 2.5 $R_{\odot}$.

us to define the observational angle of each radio source in addition to the 2D projection radio images. The ascending leg source height spanning from 0.8 to 1.3 $R_{\odot}$, and the descending leg source height from 0.7 to 1.3 $R_{\odot}$. Both legs are within the same range of the middle corona, with the average height of the ascending leg being only 3% higher than that of the descending leg.

The electron density, n_e, can be determined from the radio frequency profile of the contours f_r, assuming the emission mechanism is second-harmonic, as introduced in Chapter 3, and the same method used in the work introduced in Chapter 5. Then, the background electron density distribution of the coronal loop can be described by fitting an exponential model (see Equation 5.4 in the previous chapter). Different from the work in the previous chapter, the solar altitude value is determined directly from imaging data, which represent the centroids of the radio sources' contours located on the image. n_0 denotes the reference plasma density, a constant determined from the exponential fit, and λ is the hydrostatic plasma density scale height.

We found that the magnitude of the density models from both legs is similar

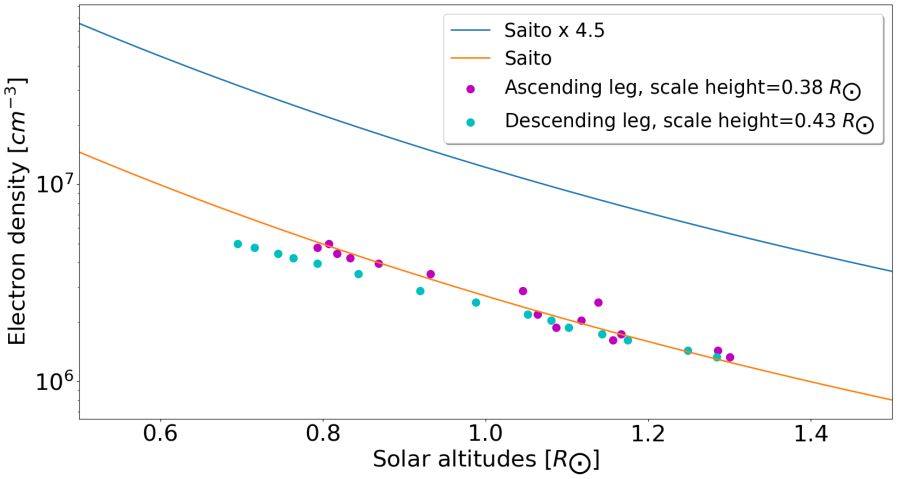

Figure 6.6: Electron density as a function of solar altitude for the ascending leg (purple dots) and descending leg (cyan dots) of the coronal loop. Overplotted is the Saito density model (orange) and the Saito density model times 4.5, which was inferred by (Reid & Kontar, 2017).

to Saito's model, as shown in Figure 6.6. The density model of the descending leg exhibits a slightly lower gradient, which means a larger density scale height compared to the ascending leg. By fitting an exponential density model, we determined the density scale height, denoted as λ in Equation 5.4, for both legs. The ascending leg density scale height, $\lambda_{ascending} = 0.38$ R$_\odot$, and the descending leg scale height, $\lambda_{descending} = 0.43$ R$_\odot$. There is only 12% difference between the scale heights, likely within the errors given by projection and scattering effect. We consider this as evidence of a symmetric loop in plasma conditions. Both scale heights are close to the statistical result of 0.36 R$_\odot$ from the analysis of 24 type J bursts observed in the same frequency range (see Chapter 5 and Zhang et al. (2023)).

6.5.2 Electron Beam Velocity

We determined the electron beam velocity directly from the image by analyzing the position of the radio source, which reflected the actual path of the propagating electron beam along with a specific travel time profile. To calculate the electron beam velocity, we measured the travel distance as the sum of the distances between each centroid position. The travel time was defined as the peak flux point time profile selected from the LOFAR dynamic spectrum. The relationship between travel distance and travel time is illustrated in Figure 6.7.

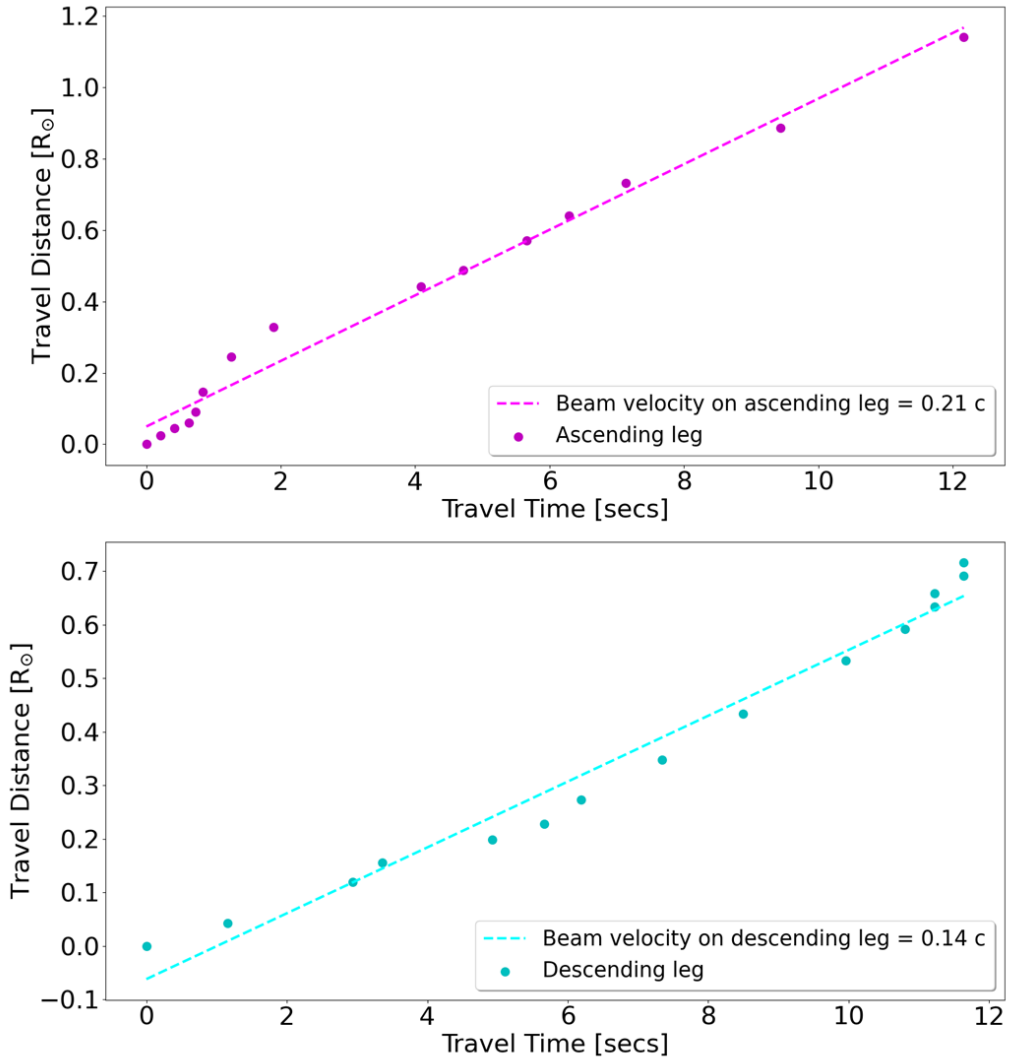

Figure 6.7: Distances between each centroid of the radio image contours vs travel time, determined for the ascending leg (top) and descending leg (bottom). The 40.2 MHz contour centroid is the start point of the ascending leg, and the 20.7 MHz contour centroid is the start point of the descending leg. The travel distance is defined as the distances between each centroid to the previous one. The electron beam velocity along the ascending leg (0.21c) was greater than that along the descending leg (0.14c).

The electron beam traveled both legs with similar travel times. Specifically, the ascending leg exhibited a travel time of 12.16 seconds, while the descending leg had a travel time of 11.64 seconds. The total travel distance for the ascending leg is 1.14 $R_\odot$, and for the descending leg, it is 0.72 $R_\odot$. By examining the plot in Figure 6.7, we observed that the electron beam velocity along the ascending leg (0.21c) was greater than that along the descending leg (0.14c).

6.5.3 Loop top temperature

Using the coronal loop density scale height, the loop top temperature can be determined by inferring the density model and assuming that the coronal plasma is in hydrostatic equilibrium. We use the hydrostatic density scale height equation (e.g. Aschwanden et al., 1992). However, due to the large height of our coronal loop, we take into account the change in gravitational acceleration as a function of heliocentric altitude rather than assuming gravitational acceleration is a constant. Consequently, we do not have an isothermal loop like Aschwanden et al. (1992). Instead the loop temperature can be described by:

$$T(r) = \frac{\beta}{1+\alpha} \frac{m_P \lambda}{k_B} \frac{GM_\odot}{r^2}, \tag{6.1}$$

where λ is the density scale height estimated from both legs by fitting an exponential model using Equation 5.4 described in the previous section, and r is the distance from the center of the Sun. The term $\frac{GM_\odot}{r^2}$ represents the gravitational acceleration, which varies as a function of r due to the large size of the coronal loop. $\alpha = 1.22$ is the ratio of electron to proton number, and $\beta = 1.44$ is the mean molecular weight, k_B is the Boltzmann constant, m_P is the mass of a proton. Therefore, we determined the temperature distributions along both the upward and downward legs of the coronal loop from both the ascending and descending portions of the U-burst as shown in Figure 6.8.

On the ascending leg, from the 40 MHz source to the 20 MHz source position, the temperature decreases from 1.76 MK to 1.09 MK. Then, on the descending leg, the temperature increases from the loop top to the lower altitude, ranging from 1.23 MK to 2.24 MK. The temperature near the top of the coronal loop is 1.1 MK on the ascending leg at 1.3 $R_\odot$, and 1.2 MK on the descending leg at the same altitude.

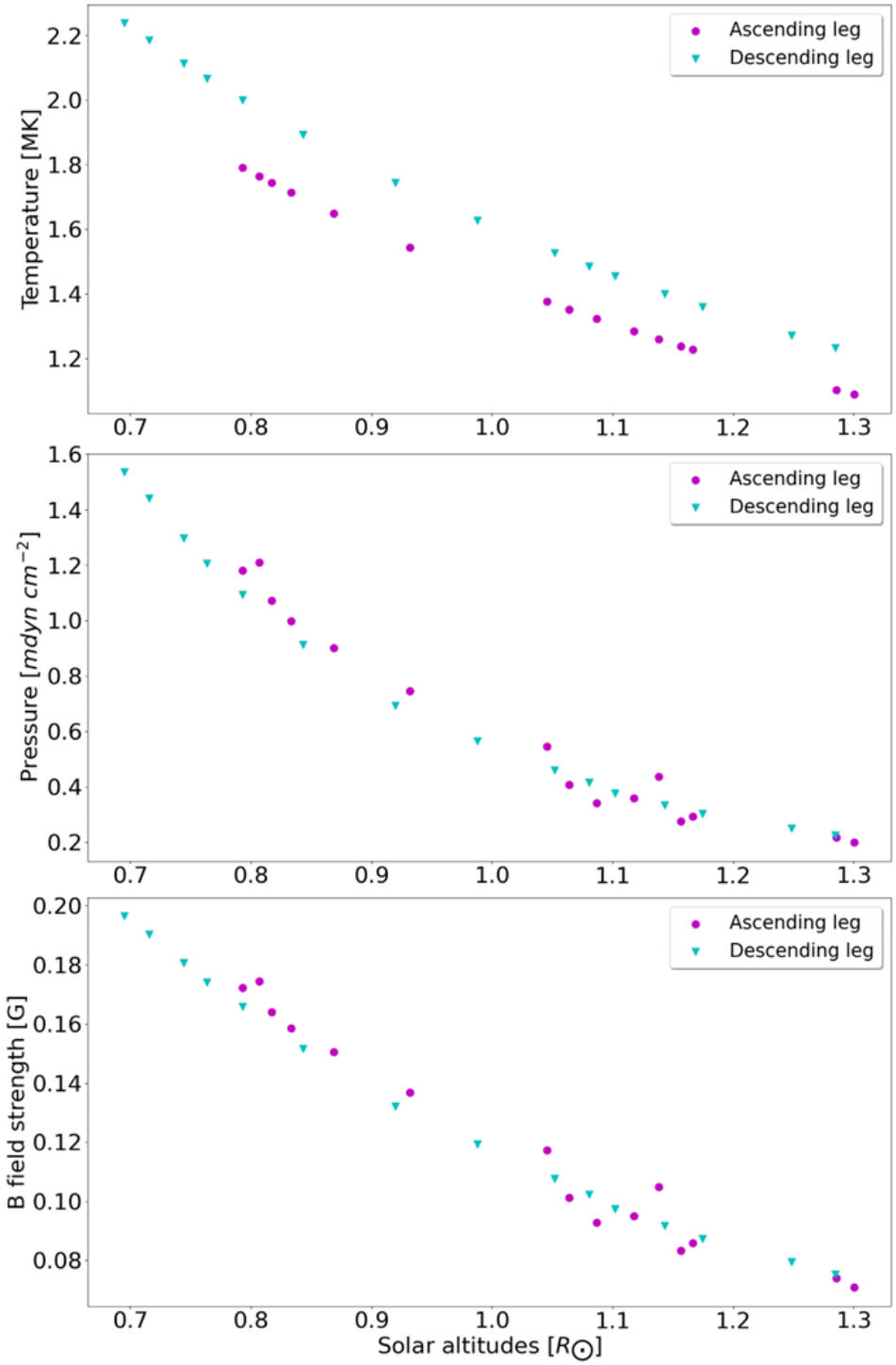

Figure 6.8: Plasma parameters of the coronal loop derived from the U-burst observations vs the coronal loop altitude. Top: temperature. Middle: pressure. Bottom: minimum magnetic field strength assuming $\beta < 1$). The ascending leg is plotted as purple dots whilst the descending leg is potted as cyan triangles.

These results are consistent with the estimations in the previous chapter (Chapter 5), based on a statistical analysis of 24 J-bursts in the same LOFAR LBA frequency range, which suggest an average loop top temperature of 1.0 ± 0.2 MK at an altitude of 1.37 $R_\odot$.

This supported the plasma temperature is symmetric within the loop. The lower temperature on the ascending leg is due to $\lambda_{descending} = 0.43$ $R_\odot$ is greater than $\lambda_{ascending} = 0.38$ $R_\odot$ in equation 6.1, as we described in section 6.5.1.

6.5.4 Loop top Pressures

Again, the loop top pressure was estimated using the ideal gas law, which incorporates the plasma density (n_e) and loop temperature (T) as follows:

$$P(h) = n_e(h) k_b T(h), \tag{6.2}$$

where $T_e(h)$ is the previously determined loop plasma temperature.

It is important to note that previous studies (e.g. Aschwanden et al., 1992) utilized the RTV law (see Rosner et al., 1978) to establish the relationship between pressure, temperature, and loop size. However, as discussed in Chapter 5 ,this relationship is not applicable in our study due to the condition that the ratio of the density scale height to the loop height is greater than one, which is necessary for using the RTV law.

We estimated that the plasma pressure near the loop top at 1.3 $R_\odot$ is 0.20 mdyn cm^{-2} on the ascending leg and 0.23 mdyn cm^{-2} on the descending leg. These results are lower than the estimation by Zhang et al. (2023) of 0.7 ± 0.3 mdyn cm^{-2} at 1.37 $R_\odot$. By using the loop top plasma temperature distribution values determined from section 6.5.3, Figure 6.8 middle panel illustrates the loop top pressure distributions of both legs. The loop top pressure along the ascending leg, following the path of the electron beam, decreases from 1.2 mdyn cm^{-2} to 0.2 mdyn cm^{-2}, and then increases on the descending leg from 0.2 mdyn cm^{-2} to 1.5 mdyn cm^{-2}. The 13% difference at 1.3 $R_\odot$ is not significant, suggesting both legs have similar plasma pressure. Similar to the temperature, the loop top plasma pressure is lower at higher altitudes, indicating that both legs are similar in this regard.

6.5.5 Loop top minimum magnetic field strength

To determine the minimum magnetic field strength of the coronal loop, we utilize the condition where the plasma β is less than one, as introduced in the previous chapter (see Equation 5.9).

We determined that the minimum magnetic field strength near the loop top at 1.3 $R_\odot$ is 0.07 G on the ascending leg and 0.08 G on the descending leg. This is only 20% lower to the estimation by Zhang et al. (2023) of 0.13 $\pm$ 0.03 G at 1.37 $R_\odot$. Similar to loop top pressure, the distribution of minimum magnetic field strength for both legs is plotted in Figure 6.8. The field strength decreases along the ascending leg from 0.17 G to 0.07 G outwards from the 40 MHz source position, and then increases on the descending leg from 0.08 G to 0.20 G downwards from the loop apex.

6.6 Discussion

6.6.1 Apparent Electron Beam Deceleration

Based on our estimations of electron beam velocities from both legs of the coronal loop, we concluded that the apparent electron beam velocity was less in the descending leg and more in the ascending leg, creating an apparent electron beam deceleration. This decrease in velocity reflects the electron energies that generate Langmuir waves which ultimately result in the detected radio emission we observe.

Numerous previous simulation studies have demonstrated that the initial properties of the electron beam (e.g. energy distribution, beam density) influence the energy of electrons in the beam which resonate with Langmuir waves (Kontar, 2001b; Li & Cairns, 2013a,b, 2014; Ratcliffe et al., 2014; Reid & Kontar, 2018b). Recently, Lorfing & Reid (2023) simulated the generation of Langmuir waves by an electron beam as it propagated from the surface of the Sun to 50 $R_\odot$. The authors show that the maximum electron velocity which resonates with Langmuir waves decreases whilst traveling from a high to a low-frequency emission region (low to high altitude). This decrease relates to the energy density of the electrons decreasing as a function of distance, as they spread out along the expanding magnetic flux tube and undergo velocity dispersion (Reid & Kontar, 2015, 2017). From observations, a decrease in the apparent velocity has been observed from type III bursts at low

frequencies corresponding to the solar wind (Dulk et al., 1987; Krupar et al., 2015).

One key difference in the descending leg of the coronal loop is the sign of the background density gradient: it is positive instead of negative. A positive density gradient is known to reduce the level of Langmuir waves produced by an electron beam, as refraction shifts waves to higher phase velocities instead of lower phase velocities (e.g. Kontar, 2001b). This behaviour is known to reduce the radio intensity of reverse type III bursts (Li et al., 2011). Whilst the higher phase velocity Langmuir waves could resonate with higher energy electrons, the increased difficulty for the electrons to generate Langmuir waves and the reduced electron flux at higher velocities would likely lead to the apparent deceleration that we have observed here. A further difficulty in the resonant production of Langmuir waves for the descending electron beam is the increasing background plasma temperature and the resultant increase in Landau Damping. Future simulations that tackle this problem and a more robust study of multiple U-bursts that can be imaged are required to investigate this further.

6.6.2 Loop Top Plasma Density Model and Physical Parameters

Using the solar U-burst, we defined the distribution of electron plasma density of the magnetic loop as a function of solar altitude above the solar surface, as shown in Figure 6.6. Both legs of the distribution exhibit similar plasma density distributions, aligning well with Saito's density model. Notably, our results show a lower density model compared to the estimation by Reid & Kontar (2017), where Saito's model was multiplied by a factor of 4.5 (also plotted in Figure 6.6) when analyzing U-bursts observed by LOFAR between 40 to 80 MHz. This same multiplier of 4.5 was also used by Zhang et al. (2023) in determining beam speeds and deriving loop parameters from J bursts observed between 20 to 80 MHz. As observed by Trottet et al. (1982), type III burst can be related to electron beams travelling along discrete, short-lived structures that were denser than the surrounding corona. Similar results have been found from other studies such as by Carley et al. (2016), who used 450-150 MHz type III burst imaging to deduce a density model that was 11.5 times that of Saito's density model. However, combining imaging of 240-80 MHz type III bursts with an MHD model, McCauley et al. (2017) found coronal structures that were similar with the Saito model, similar to our results. It would be beneficial to

use imaging of radio bursts from events at many different times and dates to build up a more statistical picture of how coronal loop density distributions can vary.

The plasma pressure that we found for the coronal loop agrees very well with the estimations of pressure using Yohoh/SXT limb data from Gary & Alexander (1999), and shown in Gary (2001) at an altitude of 1.3 solar radii. The minimum magnetic field strength we estimated using $\beta < 1$ is also within the range of field strengths shown in Gary (2001) at the same altitude. Our estimate is smaller than the value of the magnetic field estimated by Dulk & McLean (1978), around 0.3 G at the same altitude. If the plasma beta was 0.1, the minimum value shown in Gary (2001), we would get a similar value of magnetic field strength to that estimated by Dulk & McLean (1978).

6.6.3 Radio Source Size and Scattering Effect

The size of the radio source is an important measurement that can be obtained from solar radio imaging. By examining the interferometric image of the U-burst in Figure 6.3, we plotted the radio source size, defined by the semi-major axis length of the Full Width Half Maximum (FWHM), as a function of frequency shown in Figure 6.9. The size of the radio source increased while the electron beam was traveling along the ascending leg and decreased while it was traveling along the descending leg. We discovered that the radio source expanded and contracted at a similar rate on both legs: the ascending leg source size had an increase rate of 0.5 $R_\odot$ MHz^{-1}, and the descending leg had a decrease rate from the loop top, propagating downward at a rate of -0.4 $R_\odot$ MHz^{-1}. We found the beam (point-spread-function, PSF) size variation in the same way, increasing from 40.03 MHz's beam size at 0.0002 $R_\odot$ to 0.0004 $R_\odot$, which is the beam size of 20.70 MHz. Compared to the FWHM source sizes shown in Figure 6.9, ranging from 0.7 to 1.8 $R_\odot$, the beam sizes are significantly smaller (three orders of magnitude less) and are corrected by the WSClean algorithms (Offringa et al., 2014) during data processing. Therefore, the beam size has limited influence on the source size estimations.

From the U-burst image displayed in Figure 6.3, it is evident that the coronal loop's cross-section is larger at the loop top and gradually decreases towards the footpoint of the leg as shown in Figure 6.9. This loop geometry aligns with the classification of coronal loops by Zaitsev & Kronshtadtov (2017), which indicates

that the plasma pressure within the loop is high, and the flux tube cross-section increases with height. The expansion of the cross section of the coronal magnetic flux tubes leads to a decrease in the electron beam density, which subsequently reduces the generation of Langmuir waves. As a result, the radio emissions in the lower frequency part of type-III bursts and the curvature part of U bursts commonly become more diffused. This phenomenon has been discussed and studied in the work by Reid & Kontar (2015, 2017), related to type III and U-burst stopping frequencies.

Other than the magnetic tube structural expansion, another factor that significantly influences the observed size and shape of the radio source is the radio wave propagational scattering effect, as demonstrated in numbers of previous studies (for example, Steinberg et al., 1971; Bian et al., 2019; Sharykin et al., 2018; Kontar et al., 2017, 2019, 2023). This scattering effect, induced by anisotropic density turbulence, causes the size of the intrinsic source to be observed as a larger radio source by Earth-based radio telescopes. The 35 MHz radio source of both legs has a size around 0.87 $R_\odot$, close to Kontar et al. (2019)'s calculation of 1.1 $R_\odot$ based upon the scattered size of a point source, assuming fundamental emission. Moreover, we also find that a f^{-1} dependence to the source size with frequency is a reasonable fit to the data, a dependence that is predicted from radio wave scattering. As such, we can conclude that scattering is likely to play a significant role in the determination of the U-burst radio source sizes.

Another effect of radio wave scattering is the outward shift of radio sources on the image away from the solar centre displaced from their actual source location. This means the actual source is at lower altitude than the location on the U-burst image. In this case, the loop temperature estimations would be higher as the gravitational acceleration in Equation 6.1 becomes larger, so the pressure and the minimum magnetic field strength would be greater as well. We identified that the emission mechanism of the U-burst flux is second-harmonic emission, which involves less intrinsic shift of the source position compared to emission at the fundamental, and so our results will be less affected. With respect to our estimated velocities, this derived parameter is related to the relative distance between each radio source contour and not the absolute position. Consequently, scattering effects will have a very limited influence on the estimations of the electron beam velocities.

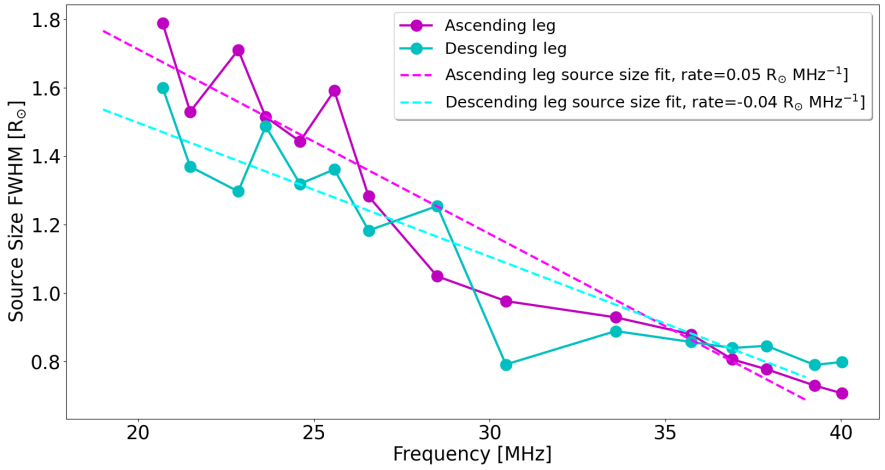

Figure 6.9: Full Width Half Maximum (FWHM) size of the observed U-burst radio source, defined by the semi-major axis size, for frequencies between 20–40 MHz. The dashed lines are linear fits to the data.

6.6.4 Projection Effect

The projection effect in solar imaging presents a significant challenge when measuring the distances of radio sources along the line-of-sight axis (z-axis). This issue arises because 2D projected radio images only yield positional information on the x and y axes. The projection effect substantially influences the estimation of electron beam velocities and the assumed density model. It also introduces uncertainties in accurately determining both the actual electron beam acceleration site and the descending leg's footpoint of the loop.

In this study, we made the assumption that the ascending leg's footpoint of the coronal loop is located at Active Region AR12765, based on simultaneous observations of a coronal jet. We posited that the ascending leg aligns with the same longitudinal plane as AR12765 (at -60° longitude), and we presumed the descending leg to be on the plane of the solar limb (at -90° longitude). Distances along the z-axis for each radio source were measured by incorporating the observational angle derived from this assumption. Therefore, the descending leg radio source heliocentric altitude determined based on this assumption is the underestimation of the real situation, as the z-axis distances are zero on the limb plane. Chen et al. (2023b) analyzed the interplanetary component of the type III bursts that we imaged during our study. The kHz radio source positions, deduced using multiple spacecraft ob-

servations were found to have a good agreement with the 60 degree Parker spiral that we found for the origin of the type III bursts and U-bursts, detected at higher frequencies with LOFAR.

6.7 Conclusions

In this study, for the first time, we used a radio U-burst to successfully image both the upward and downward legs of a large coronal loop extending into the middle corona. The U-burst was part of a series of radio bursts that lasted 90 seconds. The exciting electron beams were accelerated in an active region on the southern hemisphere, accompanied by an EUV jet. By employing high temporal and frequency resolution interferometric imaging data provided by LOFAR, we determined the loop altitude was around 1.3 $R_\odot$ above the solar surface, originating in an active region in the southern hemisphere and extending into the northern hemisphere.

We inferred density models of the coronal loops for both legs and derived the physical parameters of the coronal loop based on the density scale height from the inferred model, which is 0.38 $R_\odot$ for the ascending leg and 0.43 $R_\odot$ for the descending leg. The loop top plasma temperatures, pressures, and minimum magnetic field strengths were found to be similar on both legs. At 1.3 $R_\odot$, where the 21 MHz sources on both legs are located, the plasma temperature to be around 1.1 MK, the plasma pressure around 0.20 $\mathrm{mdyn, cm^{-2}}$, and the minimum magnetic field strength around 0.07 G. The physical parameter distributions along the loop top determined from both legs are similar, as Figure 6.8 illustrates. Therefore, we consider this as evidence that the large coronal loop possesses symmetric physical properties. The density model that we inferred from the U-burst was very similar to the Saito density model. Assuming this density model as Saito's times 4.5 (the value we used in Chapter 5 and Reid & Kontar (2017)) would result in lower altitudes and consequently higher temperatures, pressures and magnetic field strengths for the derived coronal loops.

Although U-bursts with such clear and wide frequency range are unusually seen, we suggest that more observations and comparisons are needed in the future to further explore the conclusion of symmetry of physical parameters of both upflow and downflow legs of such large-sized coronal loops.

We determined the velocity of the electron beam that excited the radio U-burst,

based on the ascending and descending leg radio source positions. Our findings reveal an apparent deceleration in the electron beam propagation along the coronal loop, with velocities decreasing from 0.21c to 0.14c. As discussed in Section 6.5.2, we propose a number of physical parameters may play a role in this apparent deceleration, including the magnetic field expansion, velocity dispersion, and the change in the sign of the background density gradient that occurs at the top of the magnetic loop, making it more difficult for high velocity electrons within the beam to generate Langmuir waves that can produce the observable radio waves (e.g. Kontar, 2001b; Reid & Kontar, 2015). We note that we do not think there was any deceleration of the electron beam, merely that a decreasing energy range of electrons resonated with the Langmuir waves as a function of distance (e.g. Lorfing & Reid, 2023).

We examined the impact of both scattering and projection effects on radio imaging. We acknowledge that the actual radio source positions could be lower than the observed altitudes due to the scattering effect, as discussed by Kontar et al. (2023). However, considering the emission mechanism of the U-burst is second-harmonic, we propose that the scattering effect's influence might be less significant compared to that of fundamental emissions. Furthermore, the scattering effect is unlikely to significantly affect the estimation of electron beam velocities and the density scale heights in this study, as the relative distances between each imaged radio source are less impacted than the absolute heights. The projection effect remains a challenge for ground-based solar radio imaging between 20 to 80 MHz. Therefore, we advocate for future observation in this range by multiple instruments from different observational positions to mitigate this issue.

Chapter 7

Science Chapter 3 - Relationship Between Microwaves and metre range during the Solar flare on June 3, 2021

Shamsutdinova, et al. 2022 (Proceeding of Science Volume 425: PoS-MUTO 2022, Published DOI: 10.22323/1.425.0065), and Shamsutdinova, et al. 2024 (Monthly Notices of the Royal Astronomical Society, in review)

The work presented in this chapter was part of a collaborative project with solar microwave experts from the Institute of Solar-Terrestrial Physics in Siberia. In this project, we studied a B1 GOES class impulsive solar flare that occurred on 3 June 2021, with the aim of enhancing our understanding of the mechanistic relationship between microwave and radio bursts detected during solar flares.

During such an impulsive flare, which exhibits a simple temporal structure, the accelerated electron beam generates microwave flux when travelling downwards, due to the gyrosynchrotron mechanism. It also generates radio flux while travelling upwards along 'open' or large closed magnetic fields in the corona's tenuous plasma, owing to the plasma emission mechanism, as introduced in Chapter 3. This process produces fast-drift bursts observable from ground-based low-frequency radio interferometers. The motivation of this study is to improve our understanding of the mechanisms underlying the relationship between microwave and radio bursts detected during solar flares. By tracing the propagation of the electron beam, we examined the kinetic properties of the beam that produce the low-frequency radio

bursts, as well as the background density model of the corona region above the flare.

The flare was observed by the Siberian Radioheliograph (SRH) within the 3-6 GHz range. My collaborators utilized SRH measurements to localize microwave sources and study their evolution (see our conference paper, Shamsutdinova et al., 2022). Spectral data from the Broadband Microwave Spectropolarimeter (BBMS) (4-8 GHz) and YAMAGAWA (70-9000 MHz) were applied to examine the evolution of flare emissions over time and frequency, tracking the propagation of accelerated electrons in the microwave region. I took responsibility to analyse the radio observations by the the E-Callisto (18-87 MHz) dynamic spectrum, where three type-III bursts and one type J bursts were identified during this only single event.

The temporal profiles of microwave and radio wave flux exhibited a peak-to-peak correlation, but with a noticeable delay time gap. The delay between the microwave and radio flux peaks is attributed to the travel time of the electron beam from the microwave emission region to the radio emission region in the solar atmosphere. I obtained the electron beam velocities by assuming numerical coronal density model at different magnitudes along the magnetic flux tube traversed by the radio flux exciters. We found that the electron beam travel times, obtained from the radio bursts, are in good agreement with the delay time estimated from the peak-to-peak correlation. By inversely inferring the best match magnitude of the coronal density model, this study presents, for the first time, a novel method to determine the coronal density model from ground-based multi-wavelength observations of a solar flare.

To clarify, in this project, my primary responsibility was analyzing the low-frequency radio bursts observed during the solar flare event on June 3, 2021, and discussing the comparative results between the electron beam travel time and the peak-to-peak delay time from the microwave and radio flux. I made significant contributions to writing the radio analysis and discussion sections of the journal article. This forms the focus of this chapter.

7.1 Introduction

As summarised in Section 2.5, solar flares are complex and powerful events that encompass a range of phenomena throughout the solar atmosphere, extending from the bottom layer, the photosphere, to the heliosphere, which defines the interplan-

etary space. Assuming the most accepted model, known as the standard model, energetic particles are accelerated due to the magnetic reconnection process and propagate in opposite directions along the flare magnetic structures. When accelerated high-energy electrons and ions travel downward from the acceleration region, they generate X-rays (see Hannah et al., 2011; Holman et al., 2011), as well as EUV and microwave emissions from the flare arcade and its footpoints (see Fletcher et al., 2011). Conversely, accelerated electron beams travelling outwards from the reconnection region along 'open' or large-sized closed magnetic loops become the source of fast-drift radio bursts (see Reid & Ratcliffe, 2014), as introduced in Section 3.2.1. These beams propagate in the corona, serving as powerful probes that diagnose local plasma conditions and magnetic field properties.

The correlation between flare X-ray emissions and corresponding flare-accelerated type III radio bursts has been analysed in numerous statistical and case studies (see, for example, Kane, 1981; Vilmer et al., 2002; Krucker et al., 2008; White et al., 2011; Reid & Vilmer, 2017). Reid & Vilmer (2017) discovered a strong connection between electrons driving type III emissions and X-ray flare emissions, with an association rate higher than 28% after analysing ten years of observations (from 2002 to 2011, radio: 4000–100 MHz, X-ray data >6 keV). Although this rate is higher than the 3% reported by Kane (1981) and 15% by Hamilton et al. (1990), it indicates that not every observed radio burst correlates with X-ray activity identifiable as a flare. Saint-Hilaire et al. (2009) and Reid & Vilmer (2017) suggest that the electron beams' density capable of producing type III bursts is lower than the density required for generating detectable X-ray emissions. Additionally, Kundu et al. (1994) and Silva et al. (2000) found that the lack of correlation between X-ray and radio emissions is due to incompatible spectral indices, indicating different electron energy distributions. As summarised by White et al. (2011), flare microwave flux is more sensitive to electrons above 300 keV, which is the high-energy part of the electron spectrum comparable to that of the radio-emission electrons. This forms the objective of this project: studying the correlation between the microwave and radio flux peaks of the flare, examining the electron propagation between the two emission regions, and probing the coronal plasma conditions in the flare region.

We analysed a B1 GOES class solar flare that occurred on 3rd June 2021, observed in multiple wavelengths including X-ray, microwave, and radio emissions from multiple instruments, as a case study. This event's observational details will be introduced in Section 7.2. A summary of my collaborators' work on the microwave data analysis is illustrated in Section 7.3. The radio data analysis conducted by me is detailed in Section 7.4, where I determined the electron beam velocities from the frequency drift rate of radio bursts by utilising different magnitudes of the coronal density model. This allowed me to calculate the specific beam travel time from the microwave emission region to the metre-wave radio emission region. By comparing the microwave-radio flux peak-to-peak delay time with the spectroscopic analysis of the radio bursts, the diagnostics of kinetic properties of the electron beams accelerated during the flare event and the inferred coronal density model in the flare region will be presented in Section 7.5. Thus, I provide a novel method to examine the plasma condition and electron trajectory in the flare region by combining microwave and radio observations, aligning well with the project's objectives. In Section 7.6, I will discuss the influence of the emission mechanism on the results we determined. I will also compare the magnitude of the inferred density model and the electron beam velocities that generated these coronal fast-drift bursts during the event to those determined by previous studies. The key findings and the conclusion of this work will be summarised in Section 7.7.

7.2 Observation

I wish to clarify emphatically that the work in this section was conducted by my collaborators, J.N. Shamsutdinova, L.K. Kashapova, and D.A. Zhdanov, as mentioned at the beginning of this chapter. The content within section 7.2 provides basic observational information.

The flare occurred at 01:36 UT on June 3, 2021. It was located in the active region AR12829, which is depicted in Figure 7.1. The AIA 193 Å EUV image, captured by the SDO-AIA, shows the flare as a bright, compact source near the eastern limb. The duration of the flare was less than one minute, and it was classified as B1 class according to the GOES classification system. This flare was observed by various instruments across a wide range of the electromagnetic spectrum from X-ray to metre radio and has been utilized in this work for detailed analysis.

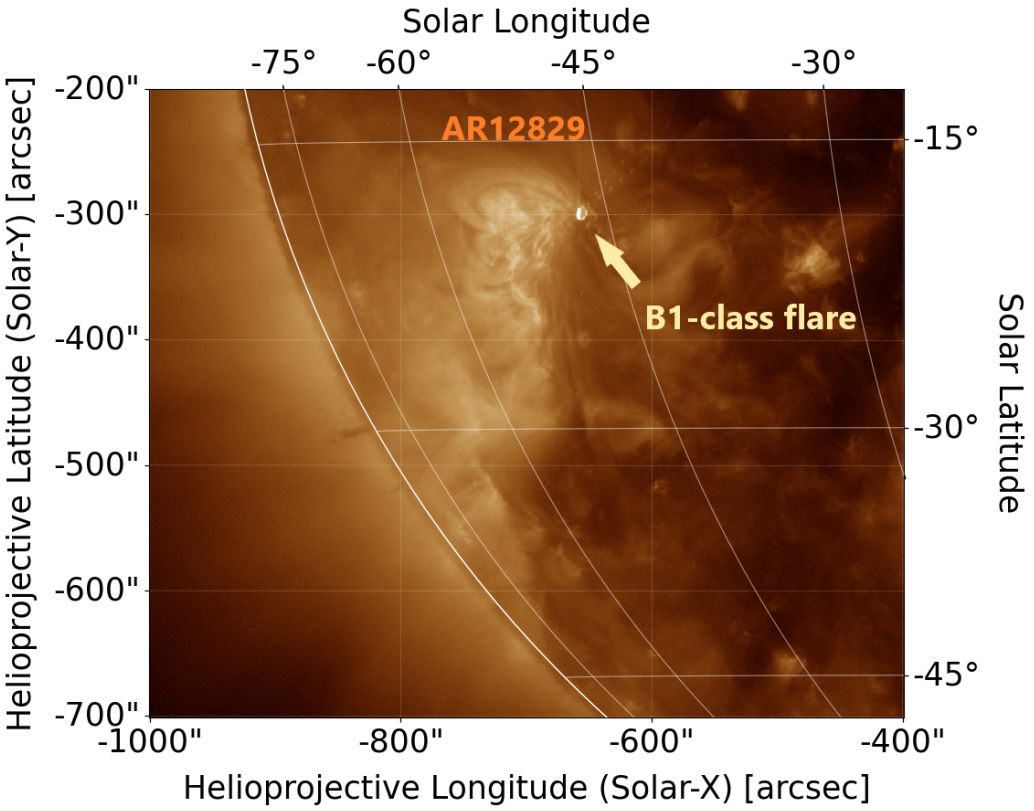

Figure 7.1: SDO AIA 193 Å image of the solar southeastern limb at 01:36:16 UT on 2021-06-03. The active region AR12829, containing the studied B1 class flare, is labeled. This figure is credited to myself.

7.2.1 X-ray and Microwave Observational data

X-ray data were obtained with the Gamma-Ray Burst Monitor of the Fermi Gamma-Ray Space Telescope (FERMI/GBM, Meegan et al., 2009). Microwave images within the 3–6 GHz range were acquired by the Siberian Radioheliograph (SRH, Lesovoi & Kobets, 2017), the Badary Broadband Microwave Spectropolarimeter (BBMS, Zhdanov & Zandanov, 2015), and were combined with data from the Nobeyama Radio Polarimeters (NoRP, Torii et al., 1979).

The team analysed spectral data and temporal profiles obtained with the Gamma-Ray Burst Monitor of the Fermi Gamma-Ray Space Telescope in X-rays (FERMI/GBM, Meegan et al., 2009). The team separated the thermal emission from the emission of non-thermal (accelerated) electrons using X-ray spectra.

Microwave images within the 3–6 GHz range were obtained using the Siberian Radioheliograph (SRH, Lesovoi & Kobets, 2017). The SRH, a T-shaped antenna array, is capable of observing microwave emissions in the 3–24 GHz range. It

provides a spatial resolution of 5 arc seconds and a temporal resolution of up to 20 ms. During the observation of the flare, the SRH operated within the 3–6 GHz range, achieving a temporal resolution of approximately 1.3 seconds.

The team also utilized correlation plots as proxies for microwave flux. These plots represent the temporal variation of the sum of cross-correlations of all antenna pairs (Lesovoi et al., 2017). This type of data is particularly useful for monitoring solar activity due to its high sensitivity to weak bursts. To extend the spectral range of our analysed microwave data, we incorporated data from the Badary Broadband Microwave Spectropolarimeter (BBMS, Zhdanov & Zandanov, 2015), in conjunction with data from the Nobeyama Radio Polarimeters (NoRP, Torii et al., 1979). The BBMS observes within the 4–8 GHz range, offering a temporal resolution of 1 second. The NoRP is capable of detecting microwave emissions across the 1–35 GHz range, with a time resolution of up to 0.1 second.

The flare topology was analysed using UV and EUV images from the SDO-AIA. Additionally, the team employed both the line-of-sight (LOS) and vector magnetograms obtained from the Helioseismic and Magnetic Imager (HMI, Scherrer et al., 2012), also on board the SDO.

7.2.2 Radio Observation

Observations of radio bursts were obtained from the dynamic spectra of the e-Callisto spectrometer network, particularly the Astronomical Society of South Australia station (e-Callisto ASSA station, Benz et al., 2005), which operates between 15–86 MHz with a time resolution of 0.25 seconds.

The integration of these spectral data with observations from the YAMAGAWA spectropolarimeter (Iwai et al., 2017), which observes within the 70 MHz–9 GHz range with a 1 second time resolution, enabled us to produce a combined dynamic spectrum. This spectrum continuously showcases emissions ranging from microwaves to the metre radio range.

The combined dynamic spectra of radio emission at metre and microwave wavelengths are shown in the top panel of Figure 7.2. This dynamic composite spectrum includes data obtained by the e-Callisto network spectrograph (15–86 MHz), the YAMAGAWA spectropolarimeters (70–2000 MHz), NoRP (2 GHz), and BBMS (3.7–9.4 GHz) during the flare event.

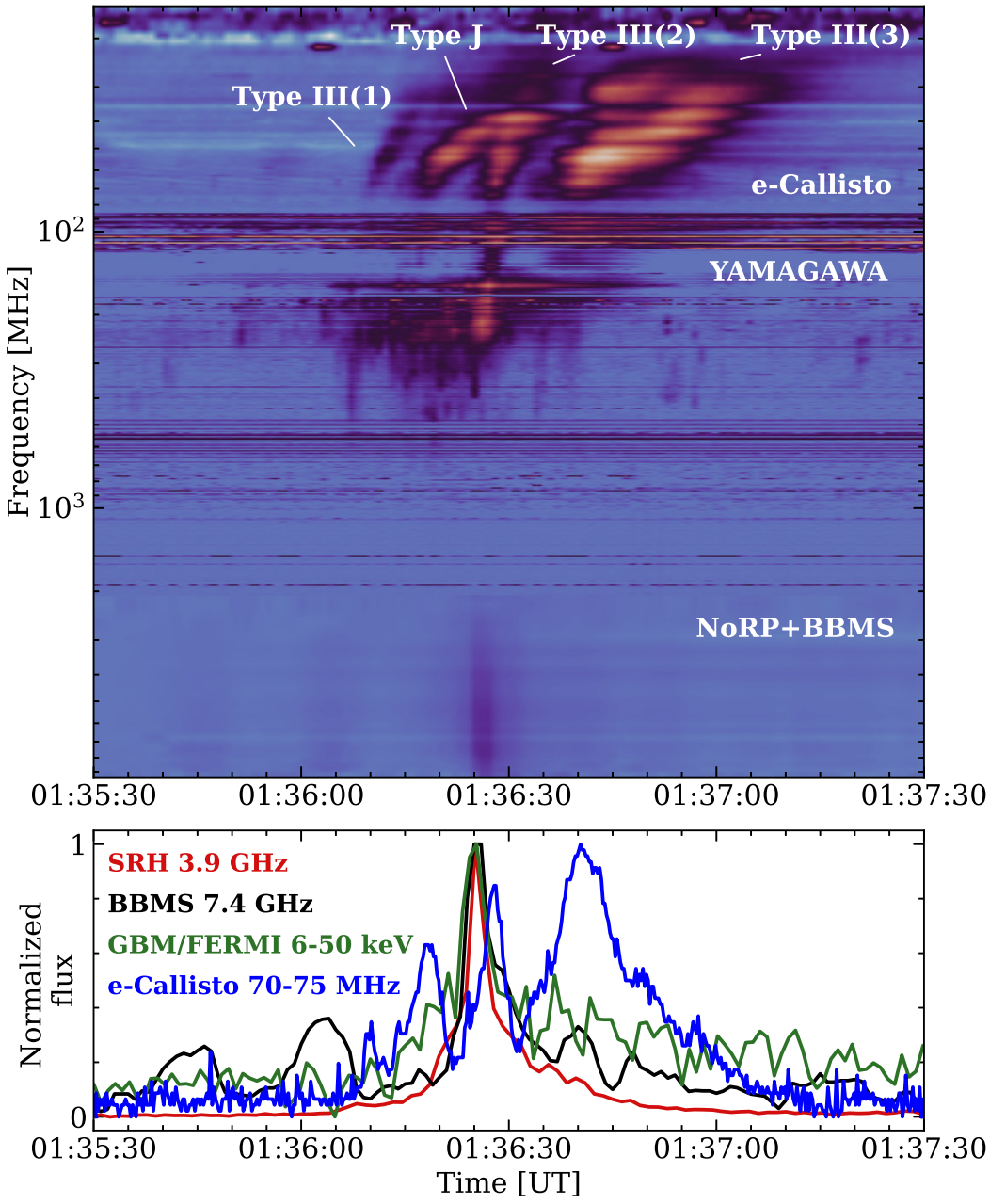

Figure 7.2: *Top:* Combined dynamic spectra obtained by e-Callisto (ASSA), YAMAGAWA in metre range within 15-2000 MHz and Nobeyama and BBMS in microwaves within 2-8 GHz during the flare SOL2021-06-03T01:35:30. *Bottom:* Comparison of microwave, metre radio and X-ray normalized temporal profiles. This figure created by my collaborators. This figure will be published on the submitted MNRAS paper.

We identified four high-intensity fast-drift radio bursts in the e-Callisto dynamic spectrum, comprising three type III bursts and one type J burst. Additionally, we observed some low-intensity bursts with structures that were overshadowed by the four main bursts. These were not considered in this study due to their low intensity nature and undetectable correlations with the peaks flux in microwave and X-ray emissions.

The bottom panel of Figure 7.2 presents a comparison of the temporal profiles of multi-wavelength measurements, ranging from radio to X-ray spectra. This comparison is achieved by integrating the flux from multiple instrumental measurements. The evolution of microwave emission is depicted through the temporal profile of the SRH correlation coefficients at 3.9 GHz and the temporal profile of the BBMS flux at 7.4 GHz. Additionally, the flux in the 6–50 keV energy band from the FERMI/GBM illustrates the evolution of the X-ray flux.

7.3 Analysis of the Flare Microwave Temporal Profile

I wish to clarify emphatically that the work in this section was conducted by my collaborators, J.N. Shamsutdinova, L.K. Kashapova, and D.A. Zhdanov, as mentioned at the beginning of this chapter. The content within Section 7.3 provides a brief introduction to the analysis work conducted by my collaborators.

The main outcome of the analysis of the flare's microwave data is to determine the temporal profile of the microwave peak flux, which will be used to measure the peak-to-peak delay time between the microwave and radio range observations. This peak-to-peak delay time will then be compared to the analysis of the radio bursts introduced in the following Section 7.4.

By comparing the temporal profiles of the flux observed by the BBMS in the microwave range (3.9 and 7.4 GHz) with those of the FERMI/GBM in the X-ray range (6-24.5 and 24.5-50 keV), we observed a good agreement between microwave and X-ray emissions, as Figure 7.3 shows. This suggests that the same non-thermal population of electrons is responsible for both types of emission.

Upon comparing the BBMS microwave measurements, we observed that the time profiles at 3.9 GHz and 7.4 GHz appear similar. However, the bursts outside

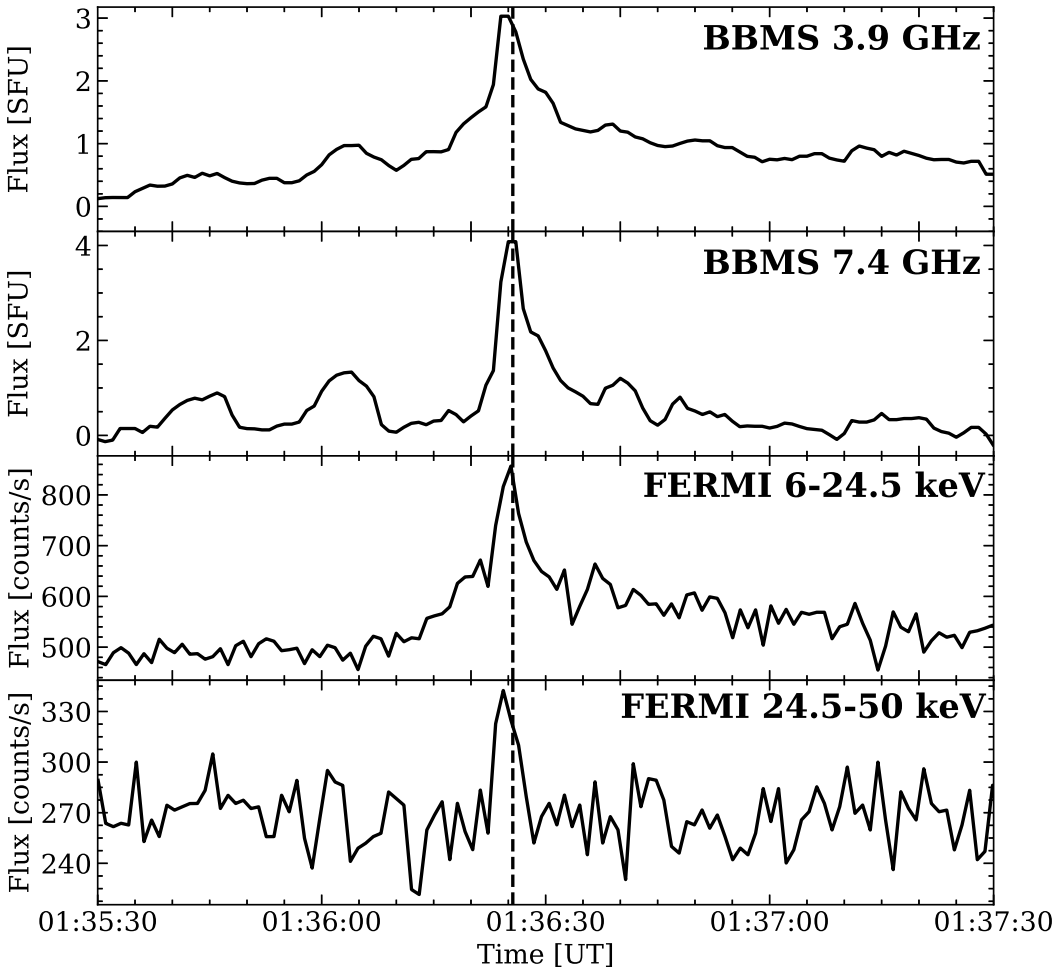

Figure 7.3: Temporal profiles in microwaves and X-rays. The dashed line shows the main peak at 01:36:26UT. The temporal profiles at 7.4 GHz and 24.5–50 keV present the evolution of non-thermal electron flux. This figure created by my collaborators. This figure will be published on the submitted MNRAS paper.

the main peak are less pronounced at 3.9 GHz. This difference is attributed to the formation of the 3.9 GHz flux in an optically thick environment for microwave (MW) emissions at the level of the flare loop. Consequently, we primarily used the temporal profile at 7.4 GHz for comparison with the radio flux measured by e-Callisto, as detailed in the following sections.

In this collaborative project, my collaborators advanced the analysis of the spectral properties of microwave sources using imaging data from the SRH. They examined the evolution of these microwave sources by constructing two masks on the microwave images, which enhanced our understanding of the magnetic topology of the flare. However, this particular aspect is not the main focus of this thesis. The

primary objective of this chapter is to analyse the radio bursts identified in the e-Callisto dynamic spectrum and to compare with the temporal profiles of microwave flux measured by BBMS at 7.4 GHz, as initially outlined at the beginning of this section.

7.4 Analysis of the Radio Bursts

I wish to clarify here that the work in this section and the rest of the chapter was conducted by myself. The credit for Figure 7.6 goes to my collaborators.

In the e-Callisto dynamic spectrum shown in Figure 7.4, four fast-drift radio bursts were identified. Upon individually examining the frequency drift profiles of each burst, it was found that Type III (1) and (2) bursts exhibited a high frequency drift rate from about 80 to 20 MHz, characterizing them as typical Type III bursts. The classification of the Type III (3) burst is less clear; it could be either a Type III or J burst. This ambiguity arises from the complex frequency profile below 50 MHz, suggesting that the accelerated electron beam may have diverged into different magnetic field structures at the 50 MHz region, or in another case, this could be a group of solar radio bursts flux generated by different exciting electron beams at a similar time, thus appearing on the dynamic spectrum with such a frequency structure. However, the light curve of the burst above 50 MHz displays characteristics typical of a Type III burst.

We employed the same method as used in Chapter 5 to determine the electron beam velocity of each identified radio burst. This was achieved by analysing the temporal profile of the maximum peak flux from their high-frequency part (ranging from 58 to 75 MHz). The rationale behind choosing this high-frequency range is its clear flux structure and its stronger correlation with magnetic flux tubes that are relatively more vertical in the solar atmosphere, allowing us to use the numerical density model. In this range, the frequency drift rate remains constant, in contrast to the low-frequency part, which exhibits a more complex flux structure and a decreasing drift rate. The black solid lines in Figure 7.4 represent the peak flux of each frequency band and of each identified burst, and the gradient of the fit in the dynamic spectrum represents the frequency drift rate, df/dt. Equation 5.1 in Chapter 5 illustrates the concept that we determine the electron beam velocity from the frequency drift rate of bursts from the dynamic spectrum. Then we can deter-

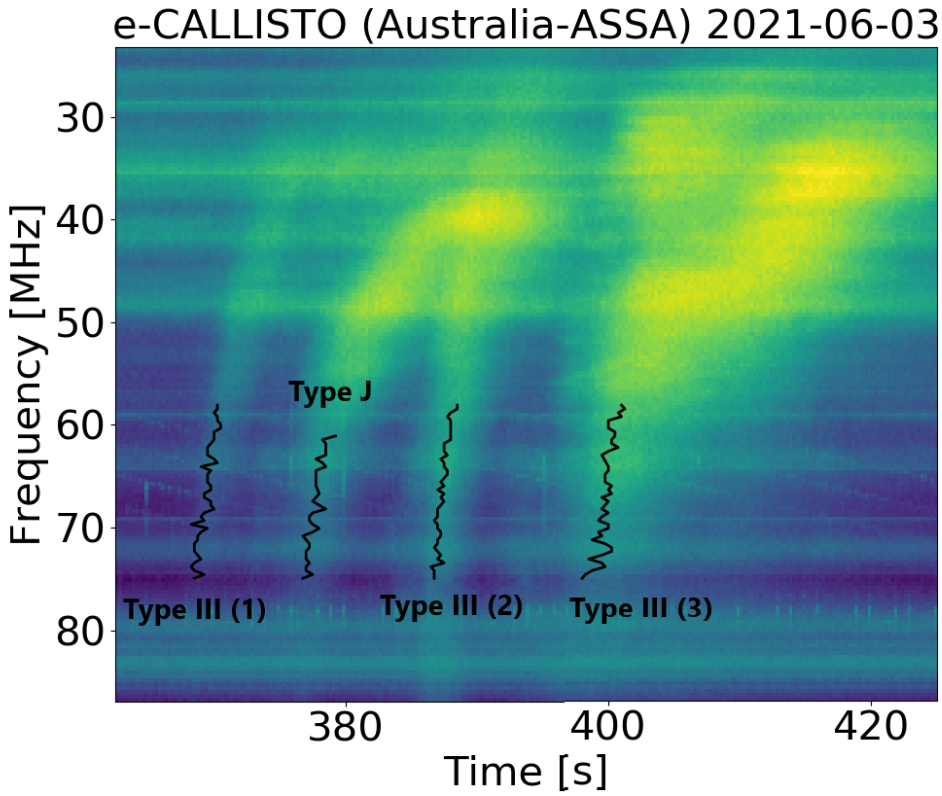

Figure 7.4: Dynamic spectrum obtained from the e-Callisto Australia-ASSA station's observation of the event. It highlights four fast-drift bursts, which are labeled according to the peak flux time profile of their high-frequency part, ranging from 58 to 75 MHz.

mine the background plasma density by assuming the emission mechanism (F or H emission; see Chapter 3), and then the density can be further converted to the corresponding heliocentric height by applying a numerical coronal density model. Finally, the electron beam velocity can be determined by knowing the travel distances, dl, of the electron beam along the radial magnetic flux tube and the time profile, dt, we obtained in the dynamic spectrum where we defined the frequency drift rate.

In this work, we assumed Saito's model (see the model's equation 2.4) and examined different magnitudes of the multiplier, ranging from 2.5 to 10.5, to determine the electron beam velocity. Additionally, the altitude of the radio source for the high-frequency part of each burst can also be determined from the density model. Therefore, the travel distances of the electron beam from the microwave to the radio emission region can be defined by the altitude differences between their source posi-

tions. Different multipliers applied to Saito's model lead to varying travel distances and electron beam velocities, and consequently, different travel times (observed as delay times between the microwave and radio flux peaks).

Although determining the microwave source height directly from the observational data in this work is challenging, we assumed that the microwave emission region, associated with a small flare arcade close to the electron beam accelerating site, is located roughly at 0.1 $R_{\odot}$ above the photosphere. This assumption is based on the analysis of the flare loop's topology, conducted by my collaborators using the SRH microwave imaging technique (see the two directed papers).

We assume that the radio bursts identified in the e-Callisto dynamic spectrum are second-harmonic emissions. In this study, we do not have polarisation measurements for classifying the emission type. This assumption is based on numerous observations indicating that radio bursts more commonly show harmonic emissions than fundamental ones, with an expected H-F ratio of 2:1 (e.g. Wild et al., 1954; Stewart, 1974). Additionally, the case of fundamental emission is discussed in Section 7.6.1.

We multiplied Saito's model by factors of 2.5, 4.5, 6.5, 8.5, and 10.5, respectively. As Figure 7.5 shows, the increasing magnitude of the coronal density model leads to a higher altitude of the radio emission region, thus yielding larger travel distances from the microwave to the radio emission region (noting the increase in source height, see plots in the middle column of the figure). However, the electron beam velocity determined from the radio burst frequency drift increases as the magnitude of the model increases (see plots in the first column of the figure). This is attributed to the fact that the gradient of the density model is smaller at higher altitudes compared to lower altitude regions. This topic has been discussed in Section 5.6.3.1. The increasing travel distances and electron beam velocities, assuming a higher magnitude of the coronal density model, result in increasing travel times, which correspond to the delay times predicted between the observed microwave and radio emission peak flux time profiles (see plots in the second column of the figure).

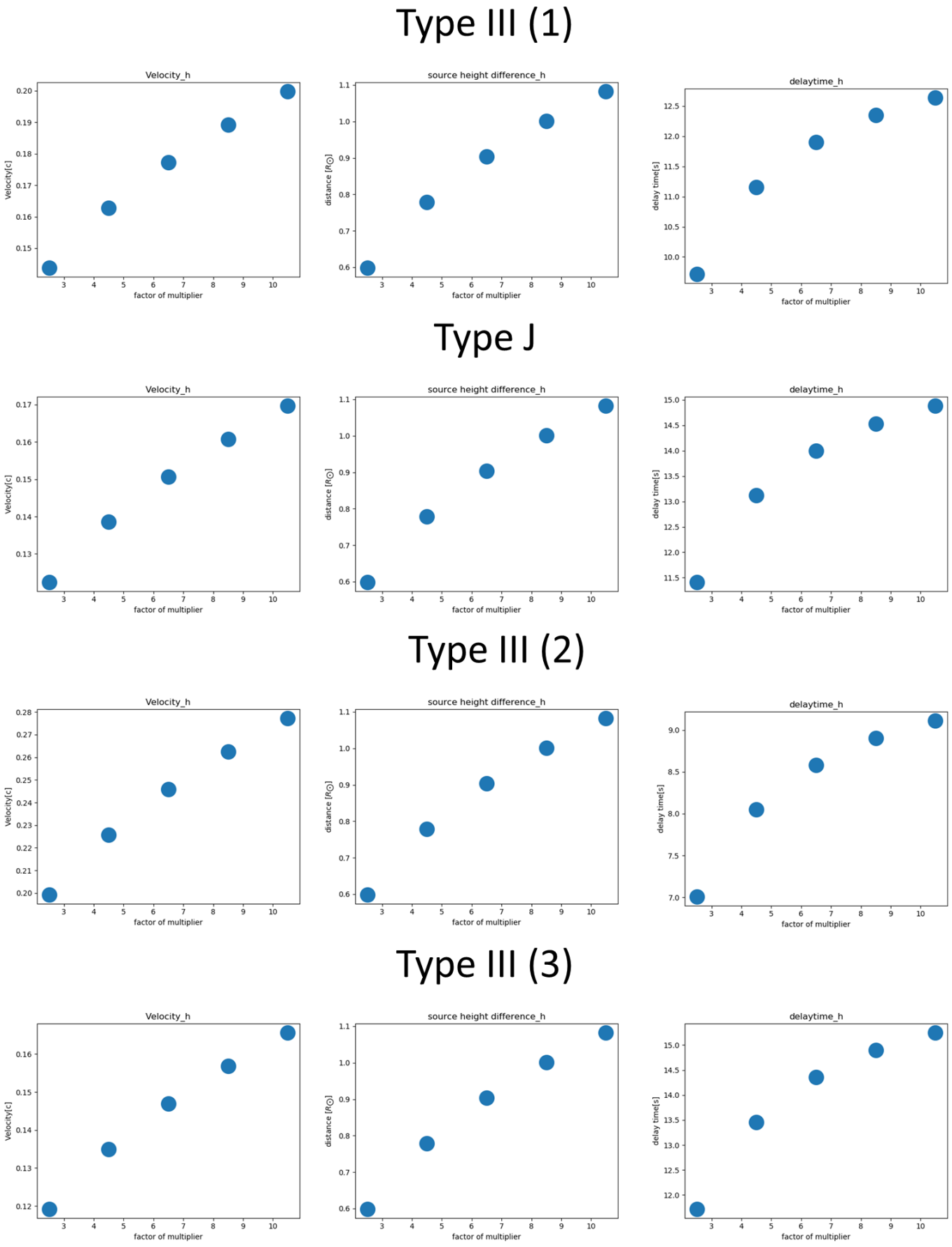

Figure 7.5: Electron beam velocity (left column), the radial height of the start frequency radio sources (75 MHz) above the photosphere (middle column), and the predicted travel time or the peak flux delay time between microwave and radio observations (right column). The x-axis for each plot represents the multipliers for Saito's model.

7.5 Relation between Microwave emission and Radio Bursts

We compared the electron beam travel time predicted using the method introduced in Section 7.4 with the time delay between the microwave and radio peak flux temporal profiles. We found that using a factor of 10.5 (summarized in Table 7.1) aligned the predictions with the observations well. When applying a factor of 10.5 to Saito's model, we predicted that the most intense type III burst (3)'s flux peak time, measured in the e-Callisto dynamic spectrum, would have a 15.2 seconds delay after the corresponding microwave flux peak. From observations, comparing the microwave (BBMS at 7.4 GHz) and radio flux peak temporal profiles, we found that the type III (3) flux peak exhibited a 15-second delay between the two observations, aligning well with our prediction, as shown in Figure 7.6 upper panel. Similarly, we predicted that for the type J burst exciter, the electron beam would have a similar travel time, 14.9 seconds. In the same figure, we identified the corresponding microwave flux peak by introducing a 15 second delay between both observations which matched our prediction.

We also predicted the travel time for the electron beam that generated the type III (2) burst to be 9.1 seconds. By shifting the radio flux observation 9 seconds earlier, we successfully located the corresponding microwave peak, which is relatively low in intensity, as Figure 7.6 bottom panel shows. The shorter delay time is attributed to the higher frequency drift rate characteristic of the type III (2) burst, resulting in the highest beam velocities among the four radio bursts as Table 7.1 shows.

We did not find a correlated microwave peak for the Type-III (1) burst. This burst was the weakest on the radio dynamic spectrum, and we considered that electron flux related with this burst was not sufficient to generate a pronounced signal in the microwave range or that the temporal resolution of the MW observations was not sufficient to detect it.

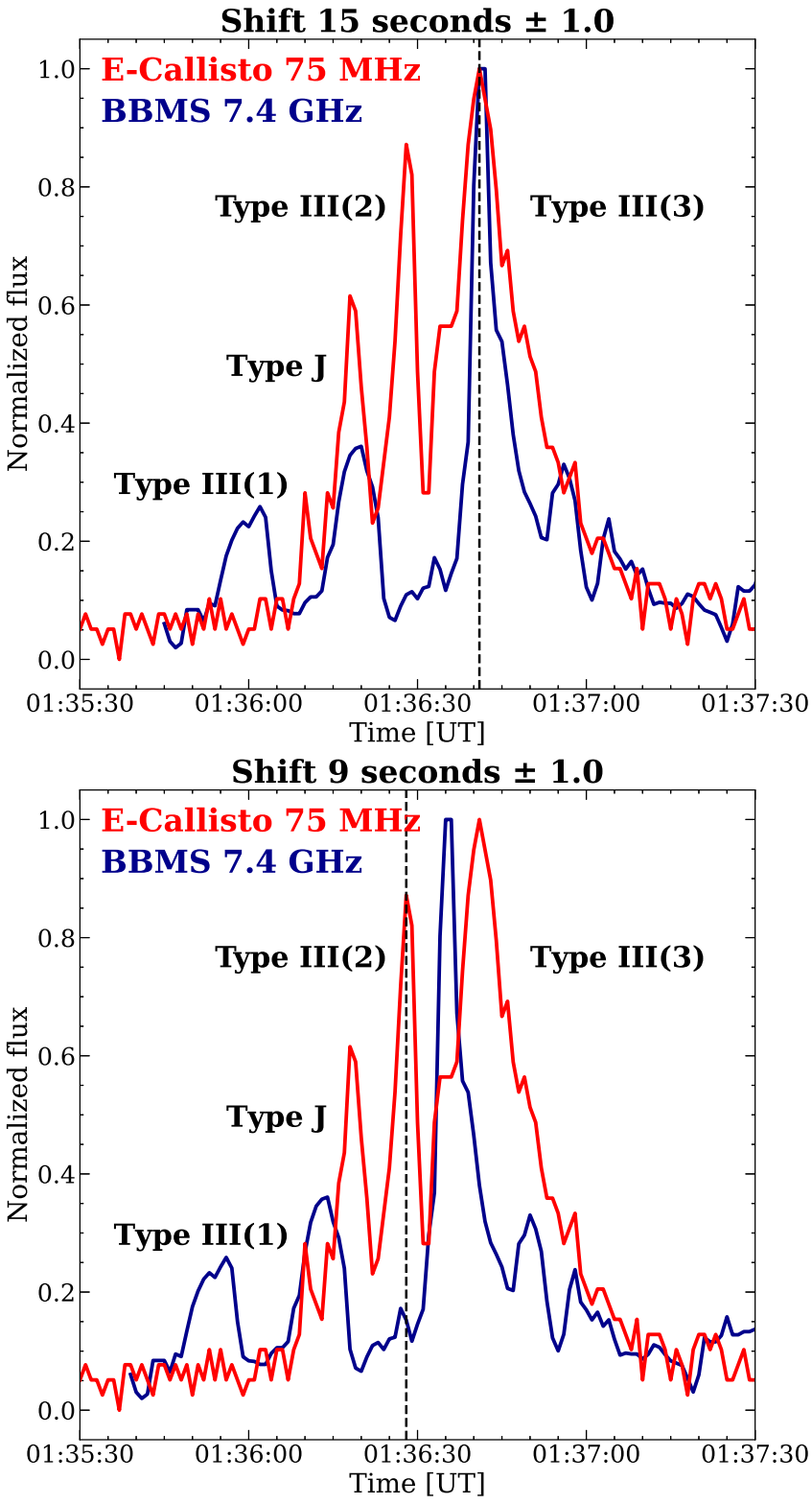

Figure 7.6: Comparison of the microwave flux temporal profile obtained by BBMS at 7.4 GHz and the radio flux temporal profile obtained by E-Callisto (ASSA) at 75 MHz ± 2 MHz. Top panel: The microwave flux is shifted 15 seconds along the time axis to the right (towards a later time range). Bottom panel: The microwave flux is shifted 9 seconds to the right. This figure created by my collaborators. This figure will be published on the submitted MNRAS paper.

Table 7.1: Predictions of the electron beam travelling time from the region of the primary energy release to the height of the radio burst generation in the assumption of the second harmonic and Saito's model × 10.5.

The radio burst	Start frequency, MHz	End frequency, MHz	Beam velocity, c	Delay time, seconds
Type III (1)	58	75	0.20	12.64
Type J	61	75	0.17	14.89
Type III (2)	58	75	0.28	9.11
Type III (3)	58	75	0.17	15.25

7.6 Discussion

7.6.1 Second-harmonic Emission Assumption

Although we initially assumed that the radio bursts observed were second-harmonic emissions, it is possible they were fundamental emissions in the real case. However, assuming fundamental emission, we calculated the beam velocity and derived the electron beam travel time from the microwave to the radio emission region, finding significantly shorter delay times. For example, by assuming 10.5 is the multiplier of the Saito's model and fundamental emission, the electron beam generated type III (3) burst took less than 12 seconds to travel from the microwave to radio emission region. These do not align well with the time delay between the microwave and radio flux peaks observed.

The reason is that the fundamental emission mechanism assumption leads to the generation of radio waves by the electron beam in a denser plasma environment, where the background plasma frequency is f_e, as opposed to the second-harmonic emission scenario of $1/2f_e$. This implies that the radio emission region is at a lower altitude in the solar corona, closer to the microwave emission region compared to the assumption of second-harmonic emission. The shorter travel distances consequently result in shorter travel times. We considered that either the radio bursts identified in this study were second-harmonic emissions, or the multiplier of Saito's model is higher than 10.5 above the flare region during the impulsive phase that generated the microwave and radio flux we studied.

We suggest that future work should involve polarization measurements of solar radio bursts. The emission mechanisms can be discerned through these measurements, as harmonic emissions typically show about 10% circular polarization,

which is low compared to around 35% for fundamental emissions (see Dulk & Suzuki, 1980).

7.6.2 Magnitude of the inferred coronal density model

In this work, we tested various multipliers to Saito's model and found that a multiplier of 10.5 fits the observations for type III (2), (3), and type J bursts. This estimated magnitude aligns well with the inferred density model by Carley et al. (2016) from a flare and flux rope observed by Nançay Radio Astronomy Facility, which uses a multiplier of 11.5. However, it is still significantly higher than the original Saito's model, being an order of magnitude higher.

The estimated multiplier at 10.5 exceeds the prediction at 4.5, which was inferred from type U burst imaging by Reid & Kontar (2017) and applied to type III and J burst analyses in Chapter 5. Applying the multiplier at 4.5 in this study, we obtained a delay time of 13.5 seconds, representing a 10% error margin from the peak-to-peak time difference of 15 seconds.

The uncertainties in the height of the microwave emission region influenced the accuracy of our estimations. In this work, we assumed the microwave emission region is at 0.1 $R_\odot$ above the photosphere, which is higher than the estimations of previous studies. For instance, White et al. (2011) determined the microwave source at 17 GHz for a flare located at the limb to be at 0.012 $R_\odot$ above the photosphere. Although this is almost an order of magnitude lower than our assumption, we determined that for the electron beam generating the type III (3) burst, a velocity of 0.17c requires an additional 1.2 seconds to travel from the microwave to the radio emission regions. Therefore, in this case, the predicted magnitude of Saito's model's multiplier at 4.5 leads to a travel time of 14.7 seconds, which is closer to the observational peak time delay of 15 seconds. In the next phase of our work, we plan to obtain the heights of microwave sources by using solar microwave imaging, which is essential to enhance the method we described in this work. This can be achieved by observing flares located close to the limb to overcome the projection effect on the microwave source position. Moreover, I suggest to combine the radio and the microwave imaging.

7.7 Conclusion

We examined the relationship between microwave and metre radio emission of the B1 GOES class flare on 3 June 2021, followed by a group of type III and type J bursts. The presence of accelerated electrons were confirmed by both HXR and MW spectra analysis. The relationship between the microwave emission and the type III radio bursts can be used as an indicator of electron propagation from the acceleration region to different layers of the solar atmosphere. Using the delay between the type III radio bursts and the microwave bursts, we have shown that a coronal density model can be estimated in the absence of imaging observations.

Based on the results of the study, we can conclude:

1. The density model of Saito's model multiplied by 10.5 provides the best estimation for the coronal plasma density distributions above this flare region. The delays obtained from comparing the microwave and metre radio ranges showed good agreement with the delays from the radio dynamic spectrum analysis using this density model. Three of the four bursts revealed in the temporal profiles of the analysed event had a peak-to-peak relationship between the radio and the microwave bursts.

2. We found that the metre radio bursts found in the considered event were generated by electron fluxes of different energies with different velocities and corresponding to different delays with MW bursts.

Chapter 8

Conclusion and Future Work

8.1 Conclusion

The focus of this thesis has been described in Chapter 1. Through my three PhD research projects, illustrated in Chapters 5, 6, and 7, respectively, I conclude the main outcomes of this thesis regarding each point of focus:

1. Investigating the kinetic properties of electron beam trajectories in the middle corona.

In Chapter 5, a total of 27 Type III and 27 J bursts were identified during the storm observed on 10 April 2019 by LOFAR, between 20 and 80 MHz. I determined the electron beam velocity for the 27 identified Type III bursts using the 'classic method', df/dt to dl/dt (see Equation 5.1), which is widely used in many previous studies (see review by Reid & Ratcliffe, 2014). In this work, I introduced a method to determine the beam velocities from the high-frequency component of J bursts. This approach avoids the curvature part of the magnetic loop top, which does not fit the density model describing a radial density distribution. A comparison between beam velocities determined from the 54 identified bursts reported similar velocities for both types: 0.16 - 0.17 c when assuming fundamental emission, and 0.18 - 0.22 c under the assumption of second-harmonic emission.

Chapter 6 presents a case study analysing a U-burst observed by LOFAR, in interferometric mode, on 5th June 2020. I visualised a large coronal loop extending to 1.3 $R_{\odot}$ above the photosphere (within the middle corona range) from the solar radio interferometric images. The U-burst exhibits a significant, bright, and clear descending component, spanning the 20 to 40 MHz range. This provides an oppor-

tunity to study the upflow and downflow legs of a large coronal loop reaching the middle corona region. The electron beam velocities were determined by measuring the travel distances between each radio source's centroids in the image (see Figure 6.3). An apparent deceleration of the electron beam was observed as it moved from the upflow, at 0.21 c, to the downflow leg of the loop, at 0.14 c. I discussed and pointed out that this apparent deceleration is attributed to a decrease in the range of electron energies resonating with Langmuir waves, likely due to the positive background plasma density gradient along the downward loop leg.

Chapter 7 presents a case study of a B1 GOES class flare observed by multiple instruments across a range of frequencies, from X-rays to radio waves, on 3rd June 2021. This work was collaborative, and my role involved analysing the radio bursts. I employed various magnitudes of numerical density models to ascertain the exciter velocities of four fast-drift bursts (three Type III and one J-burst). The density model, developed by Saito et al. (1977), was adjusted with multipliers ranging from 2.5 to 10.5, introducing variations in estimating the height of the radio emission region. It was found that the delays, which represent the electron beam travel time from the microwave to the radio emission region, obtained from comparing the microwave and metre radio ranges showed good alignment with the delays from the radio dynamic spectrum analysis, especially when using Saito's density model multiplied by 10.5.

Through the three projects focused on determining electron beam velocities from low-frequency fast-drift solar radio bursts, a total of 59 bursts were analysed. I found that the estimations align well with the generally accepted range between 0.1 and 0.5,c (e.g. Reid & Ratcliffe, 2014; Carley et al., 2016). The estimations largely rely on two assumptions when using classic methods: (1) whether assuming fundamental emission or second-harmonic emission, and (2) the magnitude of the assumed numerical coronal density model. In comparison, using imaging, as demonstrated in the U-burst project (Chapter 6), proves to be more robust as the relative travel distances can be directly determined from the observational data, thus avoiding the above two assumptions. However, I also highlighted the limitations of using solar radio imaging techniques, which include projection and scattering effects. This means the radio sources' positions on the image may differ from the

actual scenario. This leads to my first recommended area of work introduced later (see Section 8.2.1).

Both the classic and the imaging methods for determining the electron beam velocity can be further used to probe the coronal density model when combined with X-ray, EUV, and microwave observations. The work conducted in Chapter 7 serves as a good example of this approach. This leading us to the second focus point of this thesis:

2. Assessing the ambient plasma density distributions (electron plasma density model) in the middle corona.

The work presented in Chapter 5 marks the first instance, surpassing previous efforts, of deriving the density model for large-sized coronal loop tops by analysing the curvature part of the J-bursts. This achievement was realised by assuming that the electron beam velocity remains constant and that the geometry of the loop top is semi-circular. This study provided a strategy and served as an example of inferring the plasma density distribution of such large-sized loops in the middle corona region using only the dynamic spectrum data of low-frequency solar radio bursts. Through statistical analyses of 24 J-bursts observed during the same solar noise storm, it was determined that the density scale height of the loop top part ranged from 0.26 to 0.5 $R_\odot$, with an average of 0.36 $R_\odot$. For reference, the density distribution was plotted in the top panel of Figure 5.4. Notably, this method heavily relies on the beam velocity estimation, which is influenced by the assumptions discussed in the preceding focus point. It involves using an assumed numerical density model to first determine the electron beam velocity, which in this study, utilised Saito's model multiplied by 4.5 (inferred by Reid & Kontar, 2017). However, the reliance on a reference model is not always a limitation. Building on this concept, work introduced in Chapter 7 utilised the temporal correlation between microwave and radio observations of an impulsive flare. By examining different magnitudes of the reference density model and comparing them with the observed delay time, it was determined that the coronal density model above this flare, along the trajectory of the type III burst's electron beam, is Saito's model multiplied by 10.5.

In Chapter 6, I was able to directly determine the coronal density model from the U-burst image, thanks to the capability of accurately measuring the positions of

radio sources for specific frequencies offered by the LOFAR interferometric radio imaging data. This data provides unparalleled high resolution in both frequency and temporal dimensions. The U-burst presented an excellent opportunity to determine, for the first time, the density model of such a large coronal loop's downflow leg. Upon comparison, I found that the density scale heights are similar for both legs, with 0.38 $R_\odot$ on the upflow leg and 0.43 $R_\odot$ on the downflow leg. Interestingly, as shown in Figure 6.6, the inferred density distribution aligns well with the original Saito's model for both legs. This indicates that I am the first to report consistent plasma density at the same height across such a large region in the middle corona, along a large coronal closed flux tube. However, significant challenges due to scattering and projection effects remain with the solar radio imaging method. To overcome these challenges, one strategic direction is to combine the imaging method from Chapter 6 with the dynamic spectrum analysis from Chapter 7. Utilising imaging data to determine the beam velocity minimises the influence of scattering effects, as it is determined from the relative distance between radio sources. Then, examining the beam velocity and the reference density model through multi-wavelength observations (integrating radio with microwave, EUV, and X-ray observations), similar to the approach in Chapter 7, is my current project while writing up this thesis.

3. Examining the physical parameters of expansive closed magnetic loops that extend to the middle corona

In Chapter 5, I explore a strategy inspired by Aschwanden et al. (1992)'s work to determine the loop top plasma temperature (from the definition of hydrostatic scale height, derived from the preceding focus point's concluded work), pressure (from the ideal gas law), and minimum magnetic field strength (from the condition $\beta < 1$) distributions, using solely the J-burst dynamic spectrum data. Notably, the thesis utilises low-frequency radio data (20 - 80 MHz), which has rarely been used before to measure large-sized coronal loop physical parameters. This approach enabled me to determine the physical parameter distributions along the coronal loop, thanks to the variation of gravitational acceleration along such a large-sized structure across a significant radial altitude range. As discussed and concluded at the end of Chapter 5, for most loops reaching a top at 1.37 $R_\odot$, a plasma temperature

of 1 MK, pressure of 0.7 dyn, cm^{-2}, and minimum magnetic field strength of 0.13 G are comparable to smaller loop parameters determined by high-frequency radio observations (e.g., Aschwanden et al., 1992). The U-burst studied in Chapter 6 was imaged at a frequency resolution of around 1 MHz. With both legs of the coronal loop being imaged, I determined the physical parameter distributions for both legs of the loop and report symmetry in the physical characteristics of this giant loop. The coronal loop of this U-burst, slightly lower than statistical estimations in Chapter 5, stands at 1.3 $R_{\odot}$, with the plasma temperature at 1.1 MK, pressure at 0.2 dyn, cm^{-2}, and magnetic field strength at 0.07 G. These parameters are lower than the estimations from Chapter 5 due to the lower density model estimations. In conclusion, this practice is a highlight outcome of the research presented in this thesis, offering insights into diagnosing magnetic loop parameters that are large and reach into the middle corona region, which was previously poorly defined. Such an approach enhances our understanding of the physical conditions in the middle corona and contributes significantly to the broader field of solar physics. For example, the large loops' physical parameters determined in this thesis can be compared with future observations, in-situ measurement missions, and simulations.

8.2 Further work

Throughout the three research projects presented in this thesis, several challenges were encountered, leading to recommendations for further work.

8.2.1 Solar radio imaging Projection Problem

Solar radio imaging currently only yields a 2D projection of radio sources onto the 3D sky, as observations are confined to a single point: Earth. Resolving this projection effect remains a significant challenge. For instance, as mentioned in Chapter 6, it is impossible to determine the distances along the line-of-sight axis for off-disk radio sources. This limitation introduces significant uncertainties in accurately pinpointing the exact positions of radio sources. A recent example is the work by Badman et al. (2022), who developed a model describing solar wind formation and propagation from the photosphere to 1 AU. They used LOFAR interferometric imaging data of a type III burst to visualise electron beam trajectories in the middle corona range. However, Badman et al. (2022) encountered limitations in determin-

ing distances along the line-of-sight axis from the images, leading to significant uncertainties in modelling the trajectory path and the associated physical processes.

There are two possible strategies for addressing the projection effect problem in solar radio burst observations. The first involves increasing the number of observation points, particularly in the low-frequency range above 10 MHz, in space. This expansion provides opportunities to apply timing triangulation, a technique that can effectively solve the projection effect issue. An example of this approach is the 'SURROUND' project proposed by the Dublin Institute for Advanced Studies (DIAS), which plans to deploy between 3 and 5 spacecraft located at L1, L4, and L5 points, along with additional spacecraft positioned ahead of and behind Earth (see Weigt et al., 2023). The onboard radio spectrometers in these spacecraft will observe solar radio flux in the frequency range of 0.01 – 25 MHz, enabling tracking of radio bursts from distances of 2 – 150 $R_{\odot}$. I propose increasing the operating frequency range of these spectrometers to overlap with that of ground-based interferometers. This would enable simultaneous observations over the interferometric imaging to more effectively overcome the projection problem. This strategy aligns well with the recommendations provided by Seaton et al. (2023), which summarised the challenges in middle coronal studies and suggested that coordinated and overlapping observations are critical for enhancing our understanding of the large-scale structures and dynamic changes within the middle corona. However, this strategy is instrument-based and represents a long-term further work solution.

The second strategy for addressing the projection effect problem involves a simulational study of the radio-wave propagation effect, specifically the scattering effect. Kontar et al. (2019) simulated the scattering effect of a point radio source by utilising an advanced 3D stochastic description of the radio wave propagation process. They found that the sizes and shapes of the scattered radio sources, particularly the ratio between FWHM X-size and Y-size, are strongly correlated with the source's heliocentric angle, as Figure 8.1 shows. This correlation can be used to address the projection effect on the image. I recommend developing an algorithm that describes the correlation between the observational angle of solar radio sources and their shape on the image. This will involve conducting a robust number of simulations based on the propagation model and comparing them with a substantial

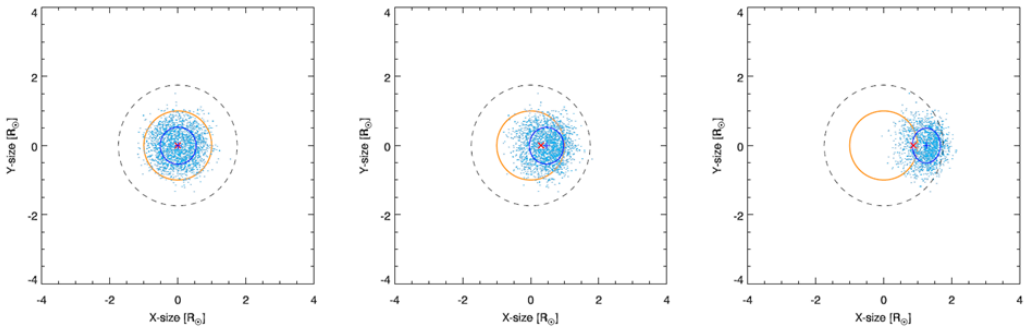

Figure 8.1: Simulated radio images for a point true source from three different source locations (0°, 10°, 30° from the disk center) demonstrate the effect of anisotropic turbulence. The projected positions of the actual sources are indicated by red crosses, while the positions of the image centroids are marked by blue crosses. The solar limb is depicted by the orange circle, and the blue ellipse represents the FWHM scattered source size. It is noteworthy that the observed radio source on the image due to scattering (blue ellipse) is comparable to LOFAR observations, as illustrated in Figure 1. These images are adopted from Kontar et al. (2019).

volume of existing observational data. The goal is to establish a novel method to mitigate the projection effect, which will also enhance the correction of scattering effects in solar radio images from simulations. I recommend applying this method to radio sources from electron beams that arise across the solar disc. This approach will allow us to constrain the morphology of magnetic loops in the middle corona and test the validity of photosphere magnetic field extrapolations.

8.2.2 Origin and trajectory of energetic particles in the solar atmosphere

Not every electron beam traversing the solar corona generates radio flux that can be identified as a solar radio burst in observations, nor is every observed radio burst correlated with X-ray activity identifiable as a flare (such as jet-driven bursts in Chapter 6). The distinctions in the acceleration processes between flare-accelerated fast-drift bursts (type III, J, and U bursts) and those without flare correlations remain elusive.

To address this, I plan to integrate high-resolution EUV imaging data from the Solar Orbiter (SolO) Extreme Ultraviolet Imager (EUI) and X-ray imaging data from the Solar Telescope Imaging X-rays (STIX) with the LOFAR low-frequency radio burst observations. I recommand to statistically analyse the acceleration properties using EUV and X-ray data to observe the magnetic fluctuations in the lower

corona, which are correlated with observed type III and U bursts. This approach will help in understanding the underlying mechanisms of electron acceleration and their manifestation in different layers of the solar atmosphere.

The multi-wavelength study of the middle corona is one of the directions I plan to pursue in my future research. The SolO EUI Full Sun Imager (FSI) with a $3.8° \times 3.8°$ Field of View (FOV) has the capacity to observe EUV emissions in the middle corona region, and the SolO Metis measuring UV and visible light from 1.9 to 9 solar radii, aligning perfectly with my intensive study using radio bursts. I aim to investigate the transition between the middle and upper corona and its connection to the heliosphere in terms of particle trajectories and magnetic field interactions by combining LOFAR and EUI observations. The combination and comparison of radio and EUV measurements will enable me to determine loop parameters and infer coronal density models in this region, which remains ill-defined, in a more robust way. Notably, this research interest of mine aligns perfectly with the EUI's scientific objective: The transition from the corona to the heliosphere (see Rochus et al., 2020).

References

2024, ASTRON. https://www.astron.nl/telescopes/lofar/

Alvarez, H., & Haddock, F. T. 1973, SoPh, 29, 197, doi: 10.1007/BF00153449

Aschwanden, M. J. 2005, Physics of the Solar Corona. An Introduction with Problems and Solutions (2nd edition)

Aschwanden, M. J., & Acton, L. W. 2001, ApJ, 550, 475, doi: 10.1086/319711

Aschwanden, M. J., Bastian, T. S., Benz, A. O., & Brosius, J. W. 1992, ApJ, 391, 380, doi: 10.1086/171353

Aschwanden, M. J., Benz, A. O., Dennis, B. R., & Schwartz, R. A. 1995, ApJ, 455, 347, doi: 10.1086/176582

Aurass, H., & Klein, K. L. 1997, A&AS, 123, 279, doi: 10.1051/aas:1997161

Aurass, H., Klein, K. L., & Martens, P. C. H. 1994, SoPh, 155, 203, doi: 10.1007/BF00670741

Badman, S. T., Carley, E., Cañizares, L. A., et al. 2022, ApJ, 938, 95, doi: 10.3847/1538-4357/ac90c2

Bale, S. D., Goetz, K., Harvey, P. R., et al. 2016, SSRv, 204, 49, doi: 10.1007/s11214-016-0244-5

Bastian, T. S., Benz, A. O., & Gary, D. E. 1998, ARA&A, 36, 131, doi: 10.1146/annurev.astro.36.1.131

Bellot Rubio, L., & Orozco Suárez, D. 2019, Living Reviews in Solar Physics, 16, 1, doi: 10.1007/s41116-018-0017-1

Benz, A. O., Barrow, C. H., Dennis, B. R., et al. 1983, SoPh, 83, 267, doi: 10.1007/BF00148280

Benz, A. O., Monstein, C., Beverland, M., Meyer, H., & Stuber, B. 2009a, SoPh, 260, 375, doi: 10.1007/s11207-009-9455-1

Benz, A. O., Monstein, C., & Meyer, H. 2005, SoPh, 226, 143, doi: 10.1007/s11207-005-5688-9

Benz, A. O., Monstein, C., Meyer, H., et al. 2009b, Earth Moon and Planets, 104, 277, doi: 10.1007/s11038-008-9267-6

Bian, N. H., Emslie, A. G., & Kontar, E. P. 2019, ApJ, 873, 33, doi: 10.3847/1538-4357/ab0411

Boischot, A., Rosolen, C., Aubier, M. G., et al. 1980, Icarus, 43, 399, doi: 10.1016/0019-1035(80)90185-2

Bougeret, J. L., Kaiser, M. L., Kellogg, P. J., et al. 1995, SSRv, 71, 231, doi: 10.1007/BF00751331

Bracewell, R. N. 2000, The Fourier transform and its applications (Ronald N. Bracewell. Boston : McGraw Hill)

Bray, R. J., & Loughhead, R. E. 1964, Sunspots (The International Astrophysics Series)

Briand, C., Zaslavsky, A., Maksimovic, M., et al. 2008, A&A, 490, 339, doi: 10.1051/0004-6361:200809842

Brown, J. C. 1973, SoPh, 31, 143, doi: 10.1007/BF00156080

Cairns, I. H., Lobzin, V. V., Warmuth, A., et al. 2009, ApJL, 706, L265, doi: 10.1088/0004-637X/706/2/L265

Cargill, P., & de Moortel, I. 2011, Nature, 475, 463, doi: 10.1038/475463a

Carley, E. P., Vilmer, N., & Gallagher, P. T. 2016, ApJ, 833, 87, doi: 10.3847/1538-4357/833/1/87

Carley, E. P., Vilmer, N., Simões, P. J. A., & Ó Fearraigh, B. 2017, A&A, 608, A137, doi: 10.1051/0004-6361/201731368

Carlsson, M., De Pontieu, B., & Hansteen, V. H. 2019, ARA&A, 57, 189, doi: 10.1146/annurev-astro-081817-052044

Carmichael, H. 1964, in NASA Special Publication, Vol. 50, 451

Chandra, R., Gupta, G. R., Mulay, S., & Tripathi, D. 2015, MNRAS, 446, 3741, doi: 10.1093/mnras/stu2305

Charbonneau, P. 2020, Living Reviews in Solar Physics, 17, 4, doi: 10.1007/s41116-020-00025-6

Chen, B., Kooi, J., Wexler, D., et al. 2023a, in Bulletin of the American Astronomical Society, Vol. 55, 059, doi: 10.3847/25c2cfeb.7e81b17a

Chen, N., Ip, W.-H., & Innes, D. 2013, ApJ, 769, 96, doi: 10.1088/0004-637X/769/2/96

Chen, X., Kontar, E. P., Chrysaphi, N., et al. 2023b, arXiv e-prints, arXiv:2306.09160, doi: 10.48550/arXiv.2306.09160

Chifor, C., Isobe, H., Mason, H. E., et al. 2008, A&A, 491, 279, doi: 10.1051/0004-6361:200810265

Cranmer, S. R. 2009, Living Reviews in Solar Physics, 6, 3, doi: 10.12942/lrsp-2009-3

Culhane, J. L., Vesecky, J. F., & Phillips, K. J. H. 1970, SoPh, 15, 394, doi: 10.1007/BF00151847

Dabrowski, B., Mikuła, K., Flisek, P., et al. 2023, A&A, 669, A52, doi: 10.1051/0004-6361/202142905

Diepen, G. v., & Dijkema, T. J. 2021, The default pre-processing pipeline (DPPP), ASTRON. https://support.astron.nl/LOFARImagingCookbook/dppp.html

Dorovskyy, V., Melnik, V., Konovalenko, A., Yerin, S., & Bubnov, I. 2021, SoPh, 296, 1, doi: 10.1007/s11207-020-01741-w

Dublin, T. C., & the Dublin Institute for Advanced Studies. Accessed date: 2023-10-27, SolarMonitor. www.solarmonitor.org

Dulk, G. A. 1985a, in Solar Radiophysics: Studies of Emission from the Sun at Metre Wavelengths, ed. D. J. McLean & N. R. Labrum, 19–35

—. 1985b, ARA&A, 23, 169, doi: 10.1146/annurev.aa.23.090185.001125

Dulk, G. A., Goldman, M. V., Steinberg, J. L., & Hoang, S. 1987, A&A, 173, 366

Dulk, G. A., & McLean, D. J. 1978, SoPh, 57, 279, doi: 10.1007/BF00160102

Dulk, G. A., & Suzuki, S. 1980, A&A, 88, 203

Elgaroy, O., & Lyngstad, E. 1972, A&A, 16, 1

Elgaroy, O., & Ugland, O. 1970, A&A, 5, 372

Emslie, A. G., Kucharek, H., Dennis, B. R., et al. 2004, Journal of Geophysical Research (Space Physics), 109, A10104, doi: 10.1029/2004JA010571

Evans, L. G., Fainberg, J., & Stone, R. G. 1973, SoPh, 31, 501, doi: 10.1007/BF00152825

Fernandes, F. C. R., Dutra, J. A. S. S., Cunha da Silva, R. D., & Sawant, H. S. 2012, Advances in Space Research, 49, 1607, doi: 10.1016/j.asr.2012.03.004

Fisher, G. H., Canfield, R. C., & McClymont, A. N. 1985, ApJ, 289, 434, doi: 10.1086/162903

Fletcher, L., Dennis, B. R., Hudson, H. S., et al. 2011, SSRv, 159, 19, doi: 10.1007/s11214-010-9701-8

Fokker, A. D. 1963, SSRv, 2, 70, doi: 10.1007/BF00174028

Fox, N. J., Velli, M. C., Bale, S. D., et al. 2016, SSRv, 204, 7, doi: 10.1007/s11214-015-0211-6

Ganse, U., Kilian, P., Vainio, R., & Spanier, F. 2012, SoPh, 280, 551, doi: 10.1007/s11207-012-0077-7

Gary, D. E. 2019, Lecture 6: Fourier Synthesis Imaging, New Jersey Institute of Technology. https://web.njit.edu/~gary/728/Lecture6.html

Gary, D. E., & Hurford, G. J. 2004, in Astrophysics and Space Science Library, Vol. 314, Astrophysics and Space Science Library, ed. D. E. Gary & C. U. Keller, 71, doi: 10.1007/1-4020-2814-8_4

Gary, G. A. 2001, SoPh, 203, 71, doi: 10.1023/A:1012722021820

Gary, G. A., & Alexander, D. 1999, SoPh, 186, 123, doi: 10.1023/A:1005147921110

Ginzburg, V. L., & Zhelezniakov, V. V. 1958, Soviet Ast., 2, 653

Ginzburg, V. L., & Zhelezniakov, V. V. 1959, in URSI Symp. 1: Paris Symposium on Radio Astronomy, ed. R. N. Bracewell, Vol. 9, 574

Golub, L., & Pasachoff, J. M. 2009, The Solar Corona (The Solar Corona by Leon Golub)

Gopalswamy, N. 2000, Geophysical Monograph Series, 119, 123, doi: 10.1029/GM119p0123

Grognard, R. J. M. 1985, in Solar Radiophysics: Studies of Emission from the Sun at Metre Wavelengths, ed. D. J. McLean & N. R. Labrum, 253–286

Guhathakurta, M., Holzer, T. E., & MacQueen, R. M. 1996, ApJ, 458, 817, doi: 10.1086/176860

Hale, G. E., & Nicholson, S. B. 1925, ApJ, 62, 270, doi: 10.1086/142933

Hamilton, R. J., Petrosian, V., & Benz, A. O. 1990, ApJ, 358, 644, doi: 10.1086/169017

Hannah, I. G., Hudson, H. S., Battaglia, M., et al. 2011, SSRv, 159, 263, doi: 10.1007/s11214-010-9705-4

Harvey, J. W., Hill, F., Hubbard, R. P., et al. 1996, Science, 272, 1284, doi: 10.1126/science.272.5266.1284

Hathaway, D. H., & Wilson, R. M. 2004, SoPh, 224, 5, doi: 10.1007/s11207-005-3996-8

Hirayama, T. 1974, SoPh, 34, 323, doi: 10.1007/BF00153671

Högbom, J. A. 1974, A&AS, 15, 417

Holman, G. D., Aschwanden, M. J., Aurass, H., et al. 2011, SSRv, 159, 107, doi: 10.1007/s11214-010-9680-9

Innes, D. E., Cameron, R. H., & Solanki, S. K. 2011, A&A, 531, L13, doi: 10.1051/0004-6361/201117255

Iwai, K., Kubo, Y., Ishibashi, H., et al. 2017, Earth, Planets and Space, 69, 95, doi: 10.1186/s40623-017-0681-8

Joshi, R. 2021, PhD thesis, Kumaun University, India

Joshi, R., Chandra, R., Schmieder, B., et al. 2020, A&A, 639, A22, doi: 10.1051/0004-6361/202037806

Kai, K., Melrose, D. B., & Suzuki, S. 1985, in Solar Radiophysics: Studies of Emission from the Sun at Metre Wavelengths, ed. D. J. McLean & N. R. Labrum (Cambridge UK: Cambridge Univ. Press), 415–441

Kane, S. R. 1981, ApJ, 247, 1113, doi: 10.1086/159121

Karlický, M. 2017, A&A, 602, A122, doi: 10.1051/0004-6361/201629652

Karlicky, M., Mann, G., & Aurass, H. 1996, A&A, 314, 303

Kasper, J. C., Abiad, R., Austin, G., et al. 2016, SSRv, 204, 131, doi: 10.1007/s11214-015-0206-3

Kerdraon, A., Pick, M., Hoang, S., Wang, Y. M., & Haggerty, D. 2010, ApJ, 715, 468, doi: 10.1088/0004-637X/715/1/468

Klassen, A., Gómez-Herrero, R., & Heber, B. 2011, SoPh, 273, 413, doi: 10.1007/s11207-011-9735-4

Klassen, A., Karlický, M., & Mann, G. 2003, A&A, 410, 307, doi: 10.1051/0004-6361:20031247

Klein, K. L., & Aurass, H. 1993, Advances in Space Research, 13, 295, doi: 10.1016/0273-1177(93)90493-U

Kontar, E. P. 2001a, Plasma Physics and Controlled Fusion, 43, 589, doi: 10.1088/0741-3335/43/4/314

—. 2001b, SoPh, 202, 131, doi: 10.1023/A:1011894830942

Kontar, E. P., Emslie, A. G., Clarkson, D. L., et al. 2023, ApJ, 956, 112, doi: 10.3847/1538-4357/acf6c1

Kontar, E. P., Brown, J. C., Emslie, A. G., et al. 2011, SSRv, 159, 301, doi: 10.1007/s11214-011-9804-x

Kontar, E. P., Yu, S., Kuznetsov, A. A., et al. 2017, Nature Communications, 8, 1515, doi: 10.1038/s41467-017-01307-8

Kontar, E. P., Chen, X., Chrysaphi, N., et al. 2019, ApJ, 884, 122, doi: 10.3847/1538-4357/ab40bb

Kopp, R. A., & Pneuman, G. W. 1976, SoPh, 50, 85, doi: 10.1007/BF00206193

Krucker, S., Saint-Hilaire, P., Christe, S., et al. 2008, ApJ, 681, 644, doi: 10.1086/588549

Krueger, A. 1979, in Geophysics and Astrophysics Monographs, Vol. 16, 23

Krupar, V., Kontar, E. P., Soucek, J., et al. 2015, A&A, 580, A137, doi: 10.1051/0004-6361/201425308

Krupar, V., Szabo, A., Maksimovic, M., et al. 2020, ApJS, 246, 57, doi: 10.3847/1538-4365/ab65bd

Kumari, A., Morosan, D. E., Kilpua, E. K. J., & Daei, F. 2023, A&A, 675, A102, doi: 10.1051/0004-6361/202244015

Kundu, M. R., Raulin, J. P., Nitta, N., et al. 1995, ApJL, 447, L135, doi: 10.1086/309567

Kundu, M. R., White, S. M., Gopalswamy, N., & Lim, J. 1994, ApJS, 90, 599, doi: 10.1086/191881

Labrum, N. R., & Stewart, R. T. 1970, PASA, 1, 316, doi: 10.1017/S132335800001208X

Lamy, L., Zarka, P., Cecconi, B., et al. 2017, in Planetary Radio Emissions VIII, ed. G. Fischer, G. Mann, M. Panchenko, & P. Zarka, 455–466, doi: 10.1553/PRE8s455

Larmor, J. 1897, Philosophical Transactions of the Royal Society of London Series A, 190, 205, doi: 10.1098/rsta.1897.0020

Lecacheux, A. 2000, Geophysical Monograph Series, 119, 321, doi: 10.1029/GM119p0321

Lecacheux, A., Dumez–Viou, C., & Klein, K.-L. 2013, in Journées scientifiques URSI–France, 73–76

Lemen, J. R., Title, A. M., Akin, D. J., et al. 2012, SoPh, 275, 17, doi: 10.1007/s11207-011-9776-8

Lesovoi, S., & Kobets, V. 2017, Solar-Terrestrial Physics, 3, 19, doi: 10.12737/article_58f96eeb8fa318.06122835

Lesovoi, S., Altyntsev, A., Kochanov, A., et al. 2017, Solar-Terrestrial Physics, 3, 3, doi: 10.12737/article_58f96ec60fec52.86165286

Li, B., & Cairns, I. H. 2013a, ApJL, 763, L34, doi: 10.1088/2041-8205/763/2/L34

—. 2013b, Journal of Geophysical Research (Space Physics), 118, 4748, doi: 10.1002/jgra.50445

—. 2014, SoPh, 289, 951, doi: 10.1007/s11207-013-0375-8

Li, B., Cairns, I. H., Yan, Y. H., & Robinson, P. A. 2011, ApJL, 738, L9, doi: 10.1088/2041-8205/738/1/L9

Lin, R. P., Evans, L. G., & Fainberg, J. 1973, Astrophys. Lett., 14, 191

Lin, R. P., Levedahl, W. K., Lotko, W., Gurnett, D. A., & Scarf, F. L. 1986, ApJ, 308, 954, doi: 10.1086/164563

Loboda, I. P., & Bogachev, S. A. 2019, ApJ, 871, 230, doi: 10.3847/1538-4357/aafa7a

Lorfing, C. Y., & Reid, H. A. S. 2023, SoPh, 298, 52, doi: 10.1007/s11207-023-02145-2

Maguire, C. A., Carley, E. P., McCauley, J., & Gallagher, P. T. 2020, A&A, 633, A56, doi: 10.1051/0004-6361/201936449

Maksimovic, M., Bale, S. D., Chust, T., et al. 2020, A&A, 642, A12, doi: 10.1051/0004-6361/201936214

Mancuso, S., Barghini, D., Bemporad, A., et al. 2023, A&A, 669, A28, doi: 10.1051/0004-6361/202243841

Mann, G., Jansen, F., MacDowall, R. J., Kaiser, M. L., & Stone, R. G. 1999, A&A, 348, 614

Maxwell, A., & Swarup, G. 1958, Nature, 181, 36, doi: 10.1038/181036a0

McCauley, P. I., Cairns, I. H., Morgan, J., et al. 2017, ApJ, 851, 151, doi: 10.3847/1538-4357/aa9cee

McGregor, S. L., Hughes, W. J., Arge, C. N., & Owens, M. J. 2008, Journal of Geophysical Research (Space Physics), 113, A08112, doi: 10.1029/2007JA012330

McLean, D. J. 1971, Australian Journal of Physics, 24, 201, doi: 10.1071/PH710201

—. 1981, PASA, 4, 132, doi: 10.1017/S1323358000016179

—. 1985, in Solar Radiophysics: Studies of Emission from the Sun at Metre Wavelengths, ed. D. J. McLean & N. R. Labrum, 37–52

Meegan, C., Lichti, G., Bhat, P. N., et al. 2009, ApJ, 702, 791, doi: 10.1088/0004-637X/702/1/791

Meléndez, J. L., Sawant, H. S., Fernandes, F. C. R., & Benz, A. O. 1999, SoPh, 187, 77, doi: 10.1023/A:1005110111620

Melnik, V. N., Konovalenko, A. A., Rucker, H. O., et al. 2011, SoPh, 269, 335, doi: 10.1007/s11207-010-9703-4

Melnik, V. N., Brazhenko, A. I., Konovalenko, A. A., et al. 2015, SoPh, 290, 193, doi: 10.1007/s11207-014-0577-8

Melrose, D. B. 1980, SSRv, 26, 3, doi: 10.1007/BF00212597

—. 1985a, in Solar Radiophysics: Studies of Emission from the Sun at Metre Wavelengths, ed. D. J. McLean & N. R. Labrum, 211–236

—. 1985b, in Solar Radiophysics: Studies of Emission from the Sun at Metre Wavelengths, ed. D. J. McLean & N. R. Labrum, 89–110

—. 1987, SoPh, 111, 89, doi: 10.1007/BF00145443

Melrose, D. B. 2009, in Universal Heliophysical Processes, ed. N. Gopalswamy & D. F. Webb, Vol. 257, 305–315, doi: 10.1017/S1743921309029470

—. 2017, Reviews of Modern Plasma Physics, 1, 5, doi: 10.1007/s41614-017-0007-0

Mikić, Z., Downs, C., Linker, J. A., et al. 2018, Nature Astronomy, 2, 913, doi: 10.1038/s41550-018-0562-5

Monstein, C. M., & Claudia. 2023, Callisto. https://www.e-callisto.org/index.html

Moore, R. L., Cirtain, J. W., Sterling, A. C., & Falconer, D. A. 2010, ApJ, 720, 757, doi: 10.1088/0004-637X/720/1/757

Morosan, D. E., Kilpua, E. K. J., Carley, E. P., & Monstein, C. 2019a, A&A, 623, A63, doi: 10.1051/0004-6361/201834510

Morosan, D. E., Gallagher, P. T., Zucca, P., et al. 2015, A&A, 580, A65, doi: 10.1051/0004-6361/201526064

Morosan, D. E., Carley, E. P., Hayes, L. A., et al. 2019b, Nature Astronomy, 3, 452, doi: 10.1038/s41550-019-0689-z

Nan, R., Li, D., Jin, C., et al. 2011, International Journal of Modern Physics D, 20, 989, doi: 10.1142/S0218271811019335

NASA. 2023, NASA. https://cdaw.gsfc.nasa.gov/movie/make_javamovie.php?img1=lasc2rdf&img2=goesx&date=20230919

Neupert, W. M. 1968, ApJL, 153, L59, doi: 10.1086/180220

Newkirk, Gordon, J. 1961, ApJ, 133, 983, doi: 10.1086/147104

Nindos, A. 2020, Frontiers in Astronomy and Space Sciences, 7, 57, doi: 10.3389/fspas.2020.00057

Nindos, A., Aurass, H., Klein, K. L., & Trottet, G. 2008, SoPh, 253, 3, doi: 10.1007/s11207-008-9258-9

Nóbrega-Siverio, D., Guglielmino, S. L., & Sainz Dalda, A. 2021, A&A, 655, A28, doi: 10.1051/0004-6361/202141472

Offringa, A. 2023, WSClean manual. https://wsclean.readthedocs.io/en/latest/index.html

Offringa, A. R., McKinley, B., Hurley-Walker, N., et al. 2014, MNRAS, 444, 606, doi: 10.1093/mnras/stu1368

Owen, C. J., Bruno, R., Livi, S., et al. 2020, A&A, 642, A16, doi: 10.1051/0004-6361/201937259

Parker, E. N. 1957, J. Geophys. Res., 62, 509, doi: 10.1029/JZ062i004p00509

—. 1958, ApJ, 128, 664, doi: 10.1086/146579

—. 1963, ApJS, 8, 177, doi: 10.1086/190087

—. 1972, ApJ, 174, 499, doi: 10.1086/151512

—. 1983, ApJ, 264, 642, doi: 10.1086/160637

Payne-Scott, R. 1949, Australian Journal of Scientific Research A Physical Sciences, 2, 214, doi: 10.1071/CH9490214

Payne-Scott, R., Yabsley, D. E., & Bolton, J. G. 1947, Nature, 160, 256, doi: 10.1038/160256b0

Petschek, H. E. 1964, in NASA Special Publication, Vol. 50, 425

Phillips, J. L., Bame, S. J., Barnes, A., et al. 1995, Geophys. Res. Lett., 22, 3301, doi: 10.1029/95GL03094

Poquerusse, M. 1994, A&A, 286, 611

Priest, E. 2014, Magnetohydrodynamics of the Sun, doi: 10.1017/CBO9781139020732

Pulupa, M., Bale, S. D., Bonnell, J. W., et al. 2017, Journal of Geophysical Research (Space Physics), 122, 2836, doi: 10.1002/2016JA023345

Raouafi, N. E., Patsourakos, S., Pariat, E., et al. 2016, SSRv, 201, 1, doi: 10.1007/s11214-016-0260-5

Raouafi, N. E., Stenborg, G., Seaton, D. B., et al. 2023, ApJ, 945, 28, doi: 10.3847/1538-4357/acaf6c

Ratcliffe, H., Kontar, E. P., & Reid, H. A. S. 2014, A&A, 572, A111, doi: 10.1051/0004-6361/201423731

Raulin, J. P., Kundu, M. R., Hudson, H. S., Nitta, N., & Raoult, A. 1996, A&A, 306, 299

Reale, F. 2014, Living Reviews in Solar Physics, 11, 4, doi: 10.12942/lrsp-2014-4

Reid, H. A. S. 2011, PhD thesis, University of Glasgow, UK

—. 2020, Frontiers in Astronomy and Space Sciences, 7, 56, doi: 10.3389/fspas.2020.00056

Reid, H. A. S., & Kontar, E. P. 2013, SoPh, 285, 217, doi: 10.1007/s11207-012-0013-x

—. 2015, A&A, 577, A124, doi: 10.1051/0004-6361/201425309

—. 2017, A&A, 606, A141, doi: 10.1051/0004-6361/201730701

—. 2018a, A&A, 614, A69, doi: 10.1051/0004-6361/201732298

—. 2018b, ApJ, 867, 158, doi: 10.3847/1538-4357/aae5d4

Reid, H. A. S., & Ratcliffe, H. 2014, Research in Astronomy and Astrophysics, 14, 773, doi: 10.1088/1674-4527/14/7/003

Reid, H. A. S., & Vilmer, N. 2017, A&A, 597, A77, doi: 10.1051/0004-6361/201527758

Reid, H. A. S., Vilmer, N., & Kontar, E. P. 2011, A&A, 529, A66, doi: 10.1051/0004-6361/201016181

Robinson, P. A., Cairns, I. H., & Willes, A. J. 1994, ApJ, 422, 870, doi: 10.1086/173779

Rochus, P., Auchère, F., Berghmans, D., et al. 2020, A&A, 642, A8, doi: 10.1051/0004-6361/201936663

Rodríguez-Pacheco, J., Wimmer-Schweingruber, R. F., Mason, G. M., et al. 2020, A&A, 642, A7, doi: 10.1051/0004-6361/201935287

Rosner, R., Tucker, W. H., & Vaiana, G. S. 1978, ApJ, 220, 643, doi: 10.1086/155949

Saint-Hilaire, P., Krucker, S., Christe, S., & Lin, R. P. 2009, ApJ, 696, 941, doi: 10.1088/0004-637X/696/1/941

Saint-Hilaire, P., Vilmer, N., & Kerdraon, A. 2013, ApJ, 762, 60, doi: 10.1088/0004-637X/762/1/60

Saito, K., Poland, A. I., & Munro, R. H. 1977, SoPh, 55, 121, doi: 10.1007/BF00150879

Sarkar, S., Paul, S., & Denra, R. 2015, Physics of Plasmas, 22, 102109, doi: 10.1063/1.4933041

Sarma, S. B. S. S. 1994, Australian Journal of Physics, 47, 811, doi: 10.1071/PH940811

Scherrer, P. H., Schou, J., Bush, R. I., et al. 2012, SoPh, 275, 207, doi: 10.1007/s11207-011-9834-2

Seaton, D., West, M., Wexler, D., et al. 2023, in Bulletin of the American Astronomical Society, Vol. 55, 360, doi: 10.3847/25c2cfeb.9a8b139f

Severino, G. 2017, The Photosphere (Cham: Springer International Publishing), 71–126, doi: 10.1007/978-3-319-64961-0_3

Shamsutdinova, J. N., Zhang, J., Zhdanov, D. A., Kashapova, L. K., & Reid, H. A. S. 2022, in The Multifaceted Universe: Theory and Observations - 2022, 65

Sharykin, I. N., Kontar, E. P., & Kuznetsov, A. A. 2018, SoPh, 293, 115, doi: 10.1007/s11207-018-1333-2

Shibata, K., Nozawa, S., & Matsumoto, R. 1992, PASJ, 44, 265

Silva, A. V. R., Wang, H., & Gary, D. E. 2000, ApJ, 545, 1116, doi: 10.1086/317822

Sittler, Edward C., J., & Guhathakurta, M. 1999, ApJ, 523, 812, doi: 10.1086/307742

Smith, D. F. 1970, Advances in Astronomy and Astrophysics, 7, 147, doi: 10.1016/B978-0-12-003207-5.50009-8

Sodré, Z. A. L., Cunha-Silva, R. D., & Fernandes, F. C. R. 2015, SoPh, 290, 159, doi: 10.1007/s11207-014-0632-5

Solanki, S. K., Inhester, B., & Schüssler, M. 2006, Reports on Progress in Physics, 69, 563, doi: 10.1088/0034-4885/69/3/R02

Staehli, M., & Benz, A. O. 1987, A&A, 175, 271

Stanislavsky, A. A., Bubnov, I. N., Koval, A. A., & Yerin, S. N. 2022, A&A, 657, A21, doi: 10.1051/0004-6361/202141984

Stanislavsky, L. A., Bubnov, I. N., Konovalenko, A. A., Tokarsky, P. L., & Yerin, S. N. 2021, Research in Astronomy and Astrophysics, 21, 187, doi: 10.1088/1674-4527/21/8/187

Stansby, D., Yeates, A., & Badman, S. T. 2020, Journal of Open Source Software, 5, 2732, doi: 10.21105/joss.02732

Steinberg, J. L., Aubier-Giraud, M., Leblanc, Y., & Boischot, A. 1971, A&A, 10, 362

Steinberg, J. L., Hoang, S., & Dulk, G. A. 1985, A&A, 150, 205

Sterling, A. C., Moore, R. L., Falconer, D. A., & Adams, M. 2015, Nature, 523, 437, doi: 10.1038/nature14556

Stewart, R. T. 1974, SoPh, 39, 451, doi: 10.1007/BF00162437

Stewart, R. T., & Vorpahl, J. 1977, SoPh, 55, 111, doi: 10.1007/BF00150878

Sturrock, P. A. 1964, in NASA Special Publication, Vol. 50, 357

—. 1966, Nature, 211, 695, doi: 10.1038/211695a0

Sturrock, P. A., & Uchida, Y. 1981, ApJ, 246, 331, doi: 10.1086/158926

Su, Y., Veronig, A. M., Holman, G. D., et al. 2013, Nature Physics, 9, 489, doi: 10.1038/nphys2675

Suzuki, S. 1978, SoPh, 57, 415, doi: 10.1007/BF00160114

Suzuki, S., & Dulk, G. A. 1985, in Solar Radiophysics: Studies of Emission from the Sun at Metre Wavelengths, ed. D. J. McLean & N. R. Labrum, 289–332

Suzuki, S., & Sheridan, K. V. 1978, Radiofizika, 20, 1432

Sweet, P. A. 1958, in Electromagnetic Phenomena in Cosmical Physics, ed. B. Lehnert, Vol. 6, 123

The SunPy Community, Barnes, W. T., Bobra, M. G., et al. 2020, The Astrophysical Journal, 890, 68, doi: 10.3847/1538-4357/ab4f7a

Thompson, A. R., Moran, J. M., & Swenson, George W., J. 2017, Interferometry and Synthesis in Radio Astronomy, 3rd Edition, doi: 10.1007/978-3-319-44431-4

Tonks, L., & Langmuir, I. 1929, Physical Review, 33, 195, doi: 10.1103/PhysRev.33.195

Torii, C., Tsukiji, Y., Kobayashi, S., et al. 1979, Proceedings of the Research Institute of Atmospherics, Nagoya University, 26, 129

Trottet, G., Pick, M., House, L., et al. 1982, A&A, 111, 306

Vaiana, G. S., Krieger, A. S., & Timothy, A. F. 1973, SoPh, 32, 81, doi: 10.1007/BF00152731

Vaiana, G. S., Reidy, W. P., Zehnpfennig, T., van Speybroeck, L., & Giacconi, R. 1968, Science, 161, 564, doi: 10.1126/science.161.3841.564

van Ballegooijen, A. A. 1986, ApJ, 311, 1001, doi: 10.1086/164837

van Driel-Gesztelyi, L., & Green, L. M. 2015, Living Reviews in Solar Physics, 12, 1, doi: 10.1007/lrsp-2015-1

van Haarlem, M. P., Wise, M. W., Gunst, A. W., et al. 2013, A&A, 556, A2, doi: 10.1051/0004-6361/201220873

Verscharen, D., Klein, K. G., & Maruca, B. A. 2019, Living Reviews in Solar Physics, 16, 5, doi: 10.1007/s41116-019-0021-0

Vilmer, N., Krucker, S., Lin, R. P., & The Rhessi Team. 2002, SoPh, 210, 261, doi: 10.1023/A:1022492414597

Wang, M., Fu, Q. J., Xie, R. X., Huang, G. L., & Duan, C. C. 2001, SoPh, 199, 157, doi: 10.1023/A:1010301632136

Wang, Y. M., Sheeley, N. R., J., Socker, D. G., et al. 1998, ApJ, 508, 899, doi: 10.1086/306450

Weigt, D. M., Cañizares, L. A., Maloney, S. A., et al. 2023, arXiv e-prints, arXiv:2308.04194, doi: 10.48550/arXiv.2308.04194

West, M. J., & Seaton, D. B. 2015, ApJL, 801, L6, doi: 10.1088/2041-8205/801/1/L6

West, M. J., Seaton, D. B., Wexler, D. B., et al. 2023, SoPh, 298, 78, doi: 10.1007/s11207-023-02170-1

Wexler, D., Imamura, T., Efimov, A., et al. 2020, SoPh, 295, 111, doi: 10.1007/s11207-020-01677-1

White, S. M. 2007, Asian Journal of Physics, 16, 189

White, S. M., Benz, A. O., Christe, S., et al. 2011, SSRv, 159, 225, doi: 10.1007/s11214-010-9708-1

Wild, J. P. 1950, Australian Journal of Scientific Research A Physical Sciences, 3, 541, doi: 10.1071/CH9500541

Wild, J. P., Murray, J. D., & Rowe, W. C. 1954, Australian Journal of Physics, 7, 439, doi: 10.1071/PH540439

Yao, J.-X., Yu, X.-F., Tlamicha, A., & Wei, F.-S. 1997, Advances in Space Research, 20, 2351, doi: 10.1016/S0273-1177(97)01054-5

Zaitsev, V. V., & Kronshtadtov, P. V. 2017, Geomagnetism and Aeronomy, 57, 841, doi: 10.1134/S001679321707026X

Zhang, J., Reid, H. A. S., Carley, E., et al. 2024, ApJ, 965, 107, doi: 10.3847/1538-4357/ad26fd

Zhang, J., Reid, H. A. S., Krupar, V., et al. 2023, SoPh, 298, 7, doi: 10.1007/s11207-022-02096-0

Zhang, P., Zucca, P., Kozarev, K., et al. 2022, ApJ, 932, 17, doi: 10.3847/1538-4357/ac6b37

Zhang, P. J., Wang, C. B., & Ye, L. 2018, A&A, 618, A165, doi: 10.1051/0004-6361/201833260

Zhang, Q. M., & Ji, H. S. 2013, A&A, 557, L5, doi: 10.1051/0004-6361/201321908

Zhdanov, D. A., & Zandanov, V. G. 2015, SoPh, 290, 287, doi: 10.1007/s11207-014-0553-3

Zweibel, E. G., & Yamada, M. 2009, ARA&A, 47, 291, doi: 10.1146/annurev-astro-082708-101726